Influence of the geometry of stemless implants on the bone adaptation process of the humerus: a computational analysis

Manuel Rosado Nunes Comenda

Thesis to obtain the Master of Science Degree in

Biomedical Engineering

Supervisors: Professor João Orlando Marques Gameiro Folgado

Professor Carlos Miguel Fernandes Quental

Examination Committee

Chairperson: Professor João Miguel Raposo Sanches

Supervisor: Professor Carlos Miguel Fernandes Quental

Members of the Committee: Professor Rui Miguel Barreiros Ruben

Doctor Marco Aurélio Carmelino Cardoso Sarmento

November 2018

Agradecimentos

Em primeiro lugar gostaria de agradecer ao Professor Carlos Quental e ao Professor João Folgado, meus orientadores, pela disponibilidade, atenção, e acima de tudo paciência demonstradas ao longo de toda a realização do trabalho. Todo o conhecimento que me transmitiram foi fundamental para a realização deste trabalho.

Gostaria também de deixar uma nota de agradecimento ao Doutor Marco Sarmento pela disponibilidade demonstrada em esclarecer conceitos anatómicos do procedimento cirúrgico da artroplastia do ombro.

Aos meus amigos e colegas de gabinete, muito obrigado por todo o apoio e ajuda, e pela companhia durante os longos dias de trabalho.

Queria agradecer à Catarina, por toda a paciência, ajuda e apoio ao longo de todo o curso, que muito contribuíram para a concretização dos meus objetivos.

Por último, mas não menos importante, queria agradecer a toda a minha família, com especial atenção aos meus pais e à minha irmã por todo o apoio demonstrado desde sempre, que tanto contribuíram para o meu crescimento pessoal.

Abstract

Aiming to reduce stem-related complications of the shoulder arthroplasty, a new type of implants arose, the stemless implants. Despite the good results in clinical studies, there is a lack of knowledge about the influence of these implants at long-term, critical to the success of the procedure, especially considering the differences in the geometry of the commercialized implants. The goal of this study was to analyse the influence of the geometry of 5 stemless implants on the bone adaptation process of the humerus after a shoulder arthroplasty. To accomplish that, shoulder arthroplasties were virtually simulated in Solidworks®, and three-dimensional finite element models were developed in Abaqus® to be used with a bone remodelling model. The analysed models were based on the ECLIPSE™ Stemless Shoulder Prosthesis from Arthrex, GLOBAL ICON™ Stemless Shoulder System from DePuy Synthes, SMR® Stemless from Lima Corporate, SIMPLICITI™ Shoulder System from Wright, and Sidus™ Stem-Free Shoulder from Zimmer. For the validation of the bone remodelling model, its bone remodelling parameters were adjusted to allow the simulation of the actual humerus density distribution. The simulations for the bone-implant assemblies were performed using those parameters. The evaluation of the changes in bone mass and density led to the conclusion that the geometry of the implants influences the bone adaptation process of the humerus. From the bone remodelling point of view, the Global Icon, SMR, and Simpliciti models showed a good performance, whereas the Eclipse model had the worst performance, followed by the Sidus model.

Keywords

Humerus, Shoulder Arthroplasty, Stemless implants, Bone remodelling, Finite element method.

Resumo

Tendo como objetivo reduzir as complicações da artroplastia do ombro relacionadas com a haste, surgiu um novo tipo de implantes, os implantes sem haste. Apesar de apresentarem bons resultados em estudos clínicos, não existe um conhecimento vasto sobre a influência destes implantes a longo prazo, crítico para o sucesso do procedimento, especialmente considerando as diferenças na geometria dos implantes comercializados. O objetivo deste trabalho foi analisar a influência da geometria de 5 implantes sem haste no processo de adaptação óssea do úmero após uma artroplastia do ombro. Para tal, simularam-se virtualmente as artroplastias do ombro em Solidworks®, e foi utilizado um modelo de remodelação óssea com modelos tridimensionais de elementos finitos utilizando o software Abaqus®. Os modelos analisados basearam-se nos implantes ECLIPSE™ *Stemless Shoulder Prosthesis* da Arthrex, GLOBAL ICON™ *Stemless Shoulder System* da DePuy Synthes, SMR® *Stemless* da Lima Corporate, SMIPLICITI™ *Shoulder System* da Wright e Sidus™ *Stem-Free Shoulder* da Zimmer. Para a validação do modelo de remodelação óssea, os seus parâmetros de remodelação óssea foram ajustados para permitir a simulação da distribuição de densidades normal do úmero. As simulações dos conjuntos osso-implante consideraram esses parâmetros. A avaliação das variações de massa e densidade óssea permitiu concluir que a geometria dos implantes tem influência no processo de adaptação óssea do úmero. Do ponto de vista de remodelação óssea, os modelos Global Icon, SMR, e Simpliciti apresentaram um bom desempenho, enquanto que o modelo Eclipse teve o pior desempenho seguido do modelo Sidus.

Palavras-chave

Úmero, Artroplastia do ombro, Implantes sem haste, Remodelação óssea, Método de elementos finitos.

Table of contents

List of figures

List of tables

List of acronyms

3-D	Three-dimensional
AVN	Avascular Necrosis
CT	Computed Tomography
CTA	Cuff Tear Arthropathy
ECM	Extracellular Matrix
FDA	Food and Drug Administration
FE	Finite Element
FEM	Finite Element Method
HU	Hounsfield Units
ME	Mean Error
OA	Osteoarthritis
RMSE	Root-Mean-Square Error
ROI	Regions of Interest
RTSA	Reverse Total Shoulder Arthroplasty
SD	Standard Deviation
STB	Soft-Tissue Balancing Approach
TPS	Titanium Plasma Spray
TSA	Total Shoulder Arthroplasty
VHP	Visible Human Project

List of symbols

$\mathbf{a}, a_i$	Microstructure parameters
$\boldsymbol{\theta}, \theta_i$	Euler angles
$\mathrm{E}^{\mathrm{H}}_{ijkm}$	Homogenized material properties
E_{ijkl}	Material properties of the base material
Y	Volume of the unit cell
¥	Solid part of the unit cell
$\boldsymbol{X}^{kl}$	Set of periodic functions from the homogenization method
E	Young's modulus
ν	Poisson's ratio
α^P	Load weight factors
$\mathbf{t}$	Surface loads
$\mathbf{u}$	Displacements field
Γ	Boundary surface of a body
Ω	Volume of a body
$\boldsymbol{\varepsilon}$	Strain field
$\boldsymbol{\upsilon}$	Virtual displacements field
ζ	Stabilization parameter of the optimization problem
$\mathbf{D}$	Descent direction
s	Step length of the optimization problem
k	Metabolic cost per unit of bone volume
m	Corrective factor for the preservation of intermediate densities
μ	Attenuation value
ρ_r	Relative density
ρ	Apparent density
V	Volume
H	Height
R	Radius
D	Diameter
L	Length
$\bar{x}$	Mean
Δbm	Change in bone mass
Δbm_O	Overall change in bone mass

1. Introduction

1.1. Motivation and objectives

According to Lübbeke et al. (2017), annual incidence rates of shoulder arthroplasty have nearly tripled over the last decade and, although shoulder arthroplasty is seen as a satisfactory treatment for the rheumatoid or osteoarthritic glenohumeral joint, its long-term performance still presents some concerns. For instance, the stress shielding effect, characterized by an adaptation of bone to changes in load distribution due to the insertion of an implant into the bone, according to Wolff's law, may be the cause of several complications. These adaptation processes weaken the bone, either making it thinner or more porous, and subsequently increasing the risk of implant failure and periprosthetic fractures.

Since the first report of a shoulder arthroplasty, there is a trend of shortening the stem's length of the humeral components to avoid stem-related complications, such as periprosthetic fractures and the occurrence of the stress shielding effect. Consequently, the last generation of shoulder implants consists in stemless implants. Besides intending to reduce the stem-related concerns, these implants allow an easier surgical procedure by reducing the surgical steps, the blood loss and the mean operative time (Berth & Pap, 2013). Additionally, this type of implants preserves proximal bone stock, which is critical for a future revision surgery, if needed, especially considering the increase of a younger population needing surgery (Nagels et al., 2003). An optimal glenoid exposure is also beneficial when compared to humeral resurfacing implants (Churchill & Athwal, 2016).

There is an increase in clinical trials addressing the performance of stemless implants, for which functional and radiologic clinical outcomes are promising and comparable to those of standard stemmed implants, either in short, mid or long-term follow-ups (Hawi et al., 2017). Nevertheless, there is evidence of the prevalence of complications, as reported by Habermeyer et al. (2015), who observed, radiologically, bone mass loss in the proximal humerus in 41.3 % of the patients. More recently, a study presenting clinical and radiologic outcomes after 9 years of follow-up also reported bone mass loss in radiographs of the humerus in 29.4 % of patients (Hawi et al., 2017). Regarding computational analyses, a small number of finite element studies address the performance of stemless implants. Overall, those studies are limited to the analysis of generic stemless implants models (Razfar et al., 2015; Reeves et al., 2018), or to only one stemless implant model (Favre & Henderson, 2016; Santos et al., 2018).

The present study is motivated by the prevalence of complications in the stemless shoulder arthroplasty, and by the lack of knowledge regarding the influence of these implants on the long-term outcome of the procedure, especially considering the significant geometry variability of the available implants, which prevents extrapolation of the outcome of one implant to the others. The goal of the present work is to analyse the impact of 5 geometries of stemless implants, available in the market, on the bone adaptation process of the humerus, using three-dimensional finite element models.

1.2. Thesis outline

The present work is divided into 7 main chapters. Chapter 2, Background Concepts, introduces some fundamental concepts for the understanding of the present work. Its sub-chapters cover topics about anatomical key concepts, anatomy of the shoulder complex, and state of the art of the shoulder arthroplasty and biomechanical modelling.

The bone remodelling model used in this study is described in Chapter 3, Bone Remodelling Model, in which its material model, optimization problem and computational simulation are detailed.

In Chapter 4, Computational Modelling, the geometric modelling of the intact bone and implants, as well as the virtual simulations of the shoulder arthroplasties, is described. Considerations about the finite element model and the bone remodelling simulations are also performed. The methodology followed for the analysis of the results is presented last.

The results obtained from the computational simulations are presented in Chapter 5, Results, and discussed in Chapter 6, Discussion.

The final conclusions and the future work concerning the computational performance of stemless implants are presented in Chapter 7.

2. Background concepts

This chapter presents a brief overview about fundamental concepts for a better understanding of the subject matter under study, including anatomical concepts, considerations about the musculoskeletal system and shoulder anatomy, a review about the shoulder arthroplasties state of the art, and background concepts about biomechanical modelling. The novel aspects of the work are presented last.

2.1. Key anatomical concepts

The terminology adopted in this work considers the human body in the anatomical position. Regardless of the position of the human body when performing a movement, the positional terms are defined with respect to this reference position, depicted in Figure 2-1.

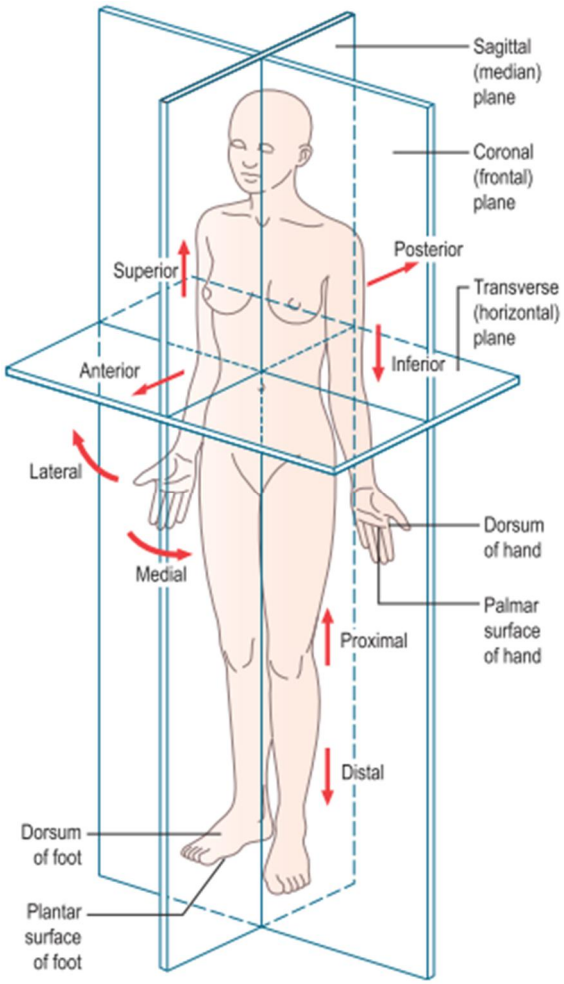

Figure 2-1 – Anatomical position presenting the cardinal planes and directional terminology (Adapted from Palastanga & Soames, 2012).

Additionally, to promote the understanding of the relation of structures one to another, 3 imaginary planes, perpendicular to each other, intersect the body. The sagittal plane divides the body into 2 symmetrical right and left halves, allowing the use of the lateral and medial terms, away and towards

the median plane, respectively. Other planes, parallel to this, are designated parasagittal planes. The coronal plane divides the body into anterior and posterior parts, in front and behind, respectively. All its parallel planes are also called coronal planes. At last, the transverse plane splits the body into superior and inferior parts. As the previous case, all its parallel planes are also called transverse planes. Some extra positional terms, also illustrated in Figure 2-1, are used such as distal and proximal, which refer to further away and closer to the trunk or root of the limb, respectively (Palastanga & Soames, 2012).

2.2. Musculoskeletal system

This section presents a brief description about the skeletal system, articular and muscular systems.

2.2.1. Skeletal system

The skeletal system is constituted by the entire framework of bones and their cartilages. It has several functions, including support, protection, assistance in movement, mineral homeostasis, blood cell production and triglyceride storage. Moreover, bone is a complex and active tissue that has the capability to continually remodel itself. It is considered an organ where several distinct tissues are found working together, such as bone tissue, cartilage, dense connective tissues, epithelium, blood-forming tissue, adipose tissue, and nervous tissue (Tortora & Derrickson, 2012).

2.2.1.1. Bone tissue

Bone is a connective tissue presenting an abundant extracellular matrix (ECM) composed of about 25 % of water, 25 % percent of collagen fibers, and 50 % of crystallized mineral salts. The bone tissue has 4 major types of cells, namely the osteogenic cells, osteoblasts, osteocytes, and osteoclasts. The osteogenic cells are unspecialized stem cells that undergo cell division, originating cells that develop into osteoblasts. Sequentially, osteoblasts build the ECM by synthetizing and secreting collagen fibers and other organic components essential to it. When mineral salts crystalize within the ECM, the tissue hardens in a process known as calcification. The osteocytes, which originate from osteoblasts during the extracellular matrix formation, are mature bone cells that ensure the bone tissue metabolism through the exchange of nutrients and wastes with the blood. Lastly, the osteoclasts are responsible for the ECM disintegration, called bone resorption. Osteoclasts derive from the fusion of white blood cells (monocytes) and release lysosomal enzymes and acids leading to the digestion of the protein and mineral ECM components (Tortora & Derrickson, 2012).

Bone is not a completely solid structure, as it has a high amount of small spaces between the cells and the ECM components. The regions of the bone may be classified as cortical (compact) or trabecular (spongy) depending on the size and distribution of the spaces. Cortical bone tissue, characterized for containing few spaces, consists in repeating units called osteons or harversian systems. Osteons are located parallel to each other, crossing longitudinally the bone. Each individual osteon is composed of a central canal containing nerves, blood and lymphatic vessels, and by concentrically arranged lamellae, which are rings of calcified ECM. Because diffusion through the lamellae is slow, an extra canal system provides alternative routes for metabolic exchanges. This extra canal system is formed due to the

canaliculi (small channels) that connect lacunae with each other and with the central canals. Lacunae are small spaces between the lamellae, which contain osteocytes. Cortical bone is penetrated transversely through perforating canals that allow vessels and nerves from the periosteum to connect with those of the central canals and medullary cavity. Trabecular bone, characterized for containing a high amount of spaces, is composed of units called trabeculae. Each individual trabecula is composed of concentric lamellae, osteocytes that lie in lacunae, and canaliculi radiating from the lacunae. In some bones, the spaces between the trabeculae are occupied by red bone marrow, which produces blood cells (Palastanga & Soames, 2012; Tortora & Derrickson, 2012). The described microstructure of the bone is illustrated in Figure 2-2.

In conclusion, the cortical bone and trabecular bone present a significant difference in their structure. The cortical bone is more dense, tough and strong than the trabecular bone, and so it plays a crucial role in resisting the loads from weight and motion (Palastanga & Soames, 2012; Tortora & Derrickson, 2012).

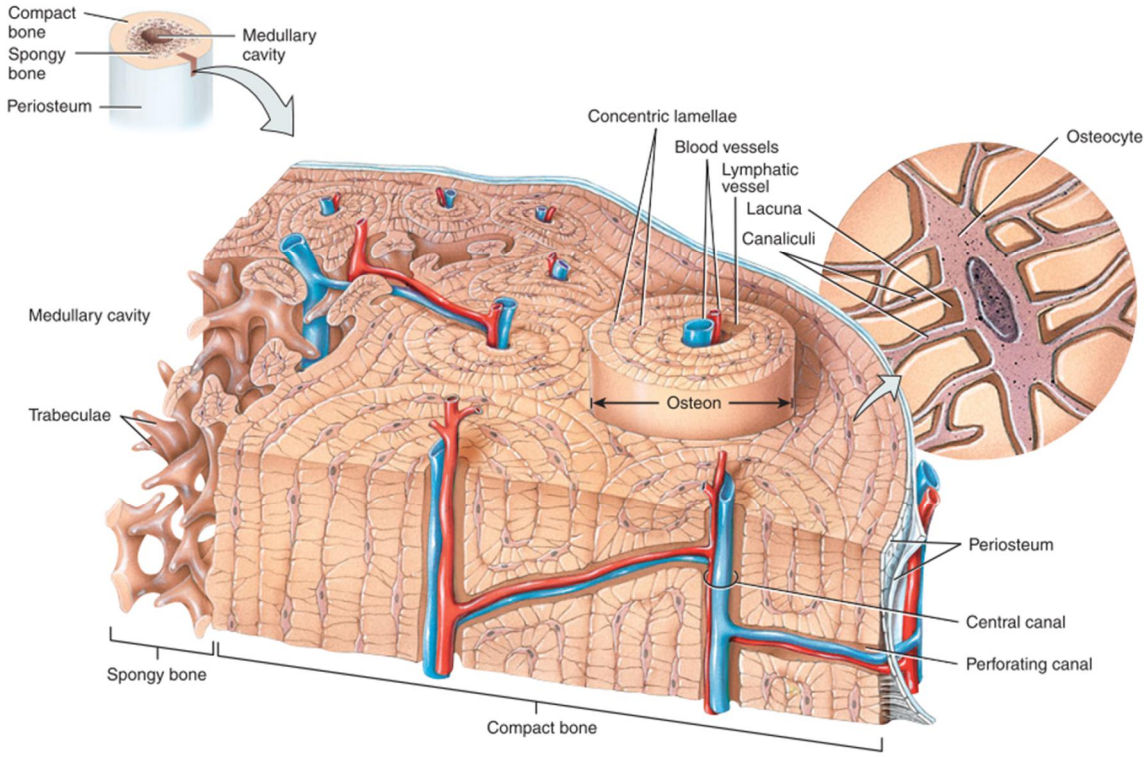

Figure 2-2 – Microscopic structure of bone tissue, including the representation of osteons in cortical (compact) bone and trabeculae in trabecular (spongy) bone (Adapted from Tortora & Derrickson, 2012).

Bones can be classified into long, short, flat or irregular, according to their shape and size. Considering the goal of this work, only the structure of a long bone, such as the humerus, is described here. The main portion of the bone, the bone's shaft, is the diaphysis which is mainly composed of cortical bone. The proximal and distal ends of the bone are called epiphyses which are composed of trabecular bone covered by a thin layer of cortical bone. The region where the diaphysis meets each epiphysis is the metaphysis. The epiphyseal line, originated from the epiphyseal plate, a layer of hyaline cartilage that allows the bone to grow in length during bone growing, can be found in its proximal end. As the bone

stops to grow, this layer of cartilage is replaced by bone. The epiphyses belonging to a joint, present a narrow layer of hyaline cartilage, called articular cartilage, which absorbs shock and reduces friction at the contacting articular surfaces. Around the bone surface, excluding the surface covered by articular cartilage, there is a resistant layer of dense irregular connective tissue associated with blood vessels called periosteum. In addition to enabling bone growing in diameter or thickness, since it contains bone-forming cells, this sheath has a protective function and serves as an attachment site for tendons and ligaments. Within the diaphysis there is a cylindric space called medullary cavity, which contains fatty yellow bone marrow in adults. The medullary cavity is covered by a thin membrane, called endosteum, containing a unique layer of bone-forming cells (Tortora & Derrickson, 2012). The described macrostructure of the bone is illustrated in Figure 2-3.

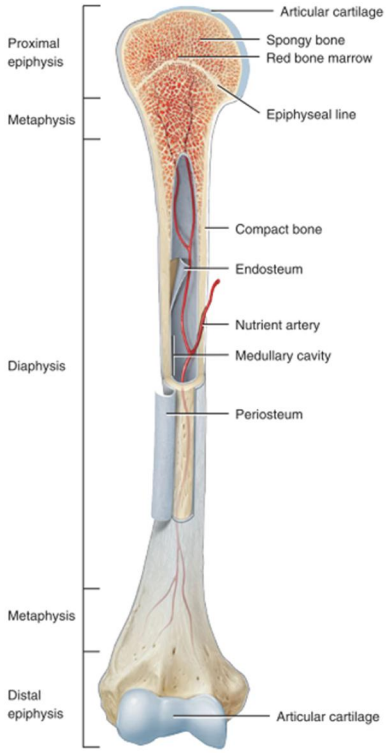

Figure 2-3 - Macroscopic structure of bone, illustration of a partially sectioned humerus (Adapted from Tortora & Derrickson, 2012).

2.2.1.2. Bone remodelling process

As mentioned before, bone is a dynamic tissue with the capability to renew itself. It experiences a continual adaption process to reach and maintain the skeletal size, shape, and structural integrity, as well as to regulate mineral homeostasis. Bone remodelling involves bone resorption that consists in the removal of minerals and collagen fibers from bone by osteoclasts, thereby causing the destruction of bone ECM. In contrast, bone remodelling also involves bone apposition characterized by the addition of minerals and collagen fibers to bone by the osteoblasts, thus resulting in the formation of bone ECM. The remodelling process occurs at different rates in distinct regions of the body, and may be influenced by several factors, such as lifestyle, changes in diet, and physical exercise. An additional factor is the presence of injured bone that triggers the remodelling process, leading to the replacement of the injured

bone by new bone. The actions of osteoclasts and osteoblasts should be properly balanced. A high level of bone formation abnormally increases the bones' thickness and weight, interfering with the movement at the joints, whereas an excessive loss of tissue or calcium reduces the strength of bones, increasing the probability of fracture (Raggatt & Partridge, 2010; Tortora & Derrickson, 2012. Walsh, 2018).

According to Wolff's law, bone is continuously subjected to remodelling processes due to mechanical stimuli. The loss of mechanical stimuli originates a decrease in bone formation and an increase in bone resorption, which affects people exposed to long-term bed rest, astronauts, and patients submitted to surgeries with an implant placement. The introduction of an implant into the bone leads to the occurrence of the stress shielding phenomenon, which consists in a reduced loading of the bone tissue due to the higher stiffness of the implant. In contrast, the increase of mechanical stimuli induced by physical activity promotes bone formation, as it is the case of tennis players who have their radii larger and more dense in the dominant side (Brodner et al., 2004; Gargiulo et al., 2017; Walsh, 2018).

Skeletal aging also influences the bone remodelling process. With age increase, a remodelling imbalance is developed, existing more bone resorption than bone formation, which leads to cortical and trabecular bone loss. Factors that play a role in this imbalance are hormone changes during ageing, and reduced muscle mass and loading (Walsh, 2018).

2.2.2. Articular system

A joint, or articulation, is a site of contact between bones, between cartilage and bones, or between teeth and bones. Joints are classified according to their structure or function. Considering their structure, joints can be classified into fibrous, cartilaginous, and synovial joints, while considering their function, they can be classified into synarthroses, amphiarthroses, and diarthroses. The synarthroses, amphiarthrosis, and diarthroses are considered, respectively, immovable, slightly movable, and freely movable joints. Considering the purpose of the present study, only the synovial type of joints is described here (Tortora & Derrickson, 2012).

Synovial joints are characterized by the presence of an articular capsule that surrounds the joint and forms a synovial cavity. It is a two-layer sleeve-like structure that links the bones in the articulation. Its outer fibrous membrane is composed of dense irregular connective tissue, mostly collagen fibers, which is attached to the bones' periosteum. In some fibrous membranes, the fibers are arranged in parallel bundles called ligaments which hold bones close together in this type of joints. The inner layer of the articular capsule, also known as synovial membrane, is composed of areolar connective tissue with elastic fibers. Inside the synovial cavity, the bones' surfaces are covered by hyaline cartilage, articular cartilage, that reduces the friction between bones and absorbs shock during movements. Helping to this function, the synovial membrane secretes synovial fluid that reduces friction by lubricating the joint as it forms a thin viscous film over the surfaces of the articular capsule. Moreover, synovial fluid supply nutrients and removes metabolic wastes from the chondrocytes within articular cartilage. According to the shape of the articulating surfaces, and the possible types of movement allowed by the joint, synovial joints are divided into 6 subtypes: plane, hinge, pivot, condyloid, saddle, and ball-and-socket joints, as illustrated in Figure 2-4 (Tortora & Derrickson, 2012).

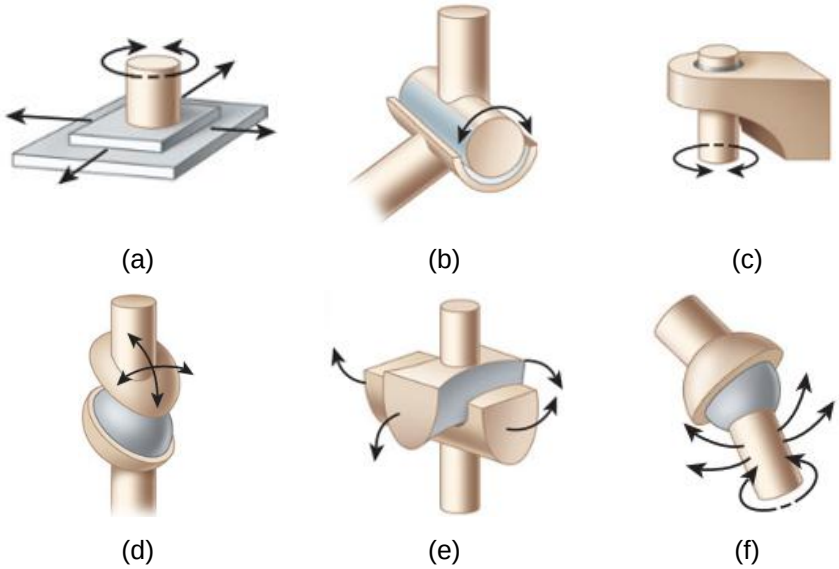

Figure 2-4 – Types of synovial joints: (a) Plane (biaxial or triaxial), (b) hinge (uniaxial), (c) pivot (uniaxial), (d) condyloid (biaxial), (e) saddle (biaxial), and (f) ball-and-socket (triaxial) (Adapted from Tortora & Derrickson, 2012).

2.2.3. Muscular system

In the human body there are 3 types of muscular tissues: skeletal, cardiac and smooth muscle tissues. Cardiac muscle tissue is found only in the heart, while smooth muscle tissue is in the walls of hollow internal structures. Skeletal muscle tissue is attached to bones and it plays an essential role in the movement of the skeleton. It is considered a voluntary muscle tissue as its contraction and relaxation can be performed by conscious control. Additional functions of the muscle tissue include stabilizing the body positions, aiding the transportation of substances within the body, and producing heat (Tortora & Derrickson, 2012).

2.3. The shoulder complex

The shoulder joint results from the articulation of the humeral head and the glenoid cavity of the scapula. Due to its geometry, it is the most mobile joint of the human body, at the expense of stability. This section presents a brief description about the shoulder related systems, such as the skeletal system, articular and muscular systems for a better understanding of the shoulder joint.

2.3.1. Skeletal system

2.3.1.1. Humerus

The humerus, illustrated in Figure 2-5, is one of the bones of the shoulder joint. It articulates proximally with the scapula, forming the shoulder joint, and distally with both the ulna and radius, forming the elbow joint. The head of the humerus is located at its proximal extremity, and it articulates with the glenoid cavity of the scapula. Distally to the head, at the former site of the epiphyseal plate, is the anatomical neck. Bellow the anatomical neck is the surgical neck. On the upper lateral part of the humerus next to the head, there is a prominence called greater tubercle, being the most lateral bony region of the shoulder. Below

the anatomical neck, on the anterior aspect, there is a distinct smaller prominence called lesser tubercle. The humerus' body comprises a roughened V-shaped area, named deltoid tuberosity, which serves as an attachment site for the deltoid muscle (Palastanga & Soames, 2012; Tortora & Derrickson, 2012). Because the present study focuses on the proximal region of the humerus, the distal regions of the humerus are not described here.

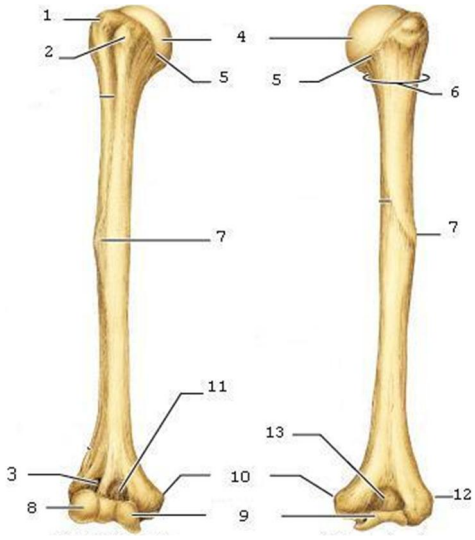

Figure 2-5 – Anterior (a) and posterior (b) views of a right humerus (Adapted from Marieb, 2001). The landmarks identified are the: 1 - Greater tubercle, 2 - Lesser tubercle, 3 - Radial fossa, 4 - Head of humerus, 5 - Anatomical neck, 6 - Surgical neck, 7 - Deltoid tuberosity, 8 – Capitulum, 9 – Trochlea, 10 - Medial epicondyle, 11 - Coronoid fossa, 12 - Lateral epicondyle, and 13 - Olecranon fossa.

Two important features of the humerus are the angle of inclination and the angle of retroversion. The angle of inclination represents the angle, ranging from 135° to 140° in the coronal plane, that the axis of the head and neck forms with respect to the long axis of the shaft, as illustrated in Figure 2-6 – (a). Notice that the centre of the humeral head is about 1 cm medial to the long axis of the shaft, and that the anatomical and mechanical axes of the humerus lie inside the bone. The angle of retroversion, ranging from 30° to 40°, denotes the rotation between the axis of the head and neck and the transverse axis of the elbow, as illustrated in Figure 2-6 – (b), (Wilk, Reinold, & Andrews, 2009; Palastanga & Soames, 2012).

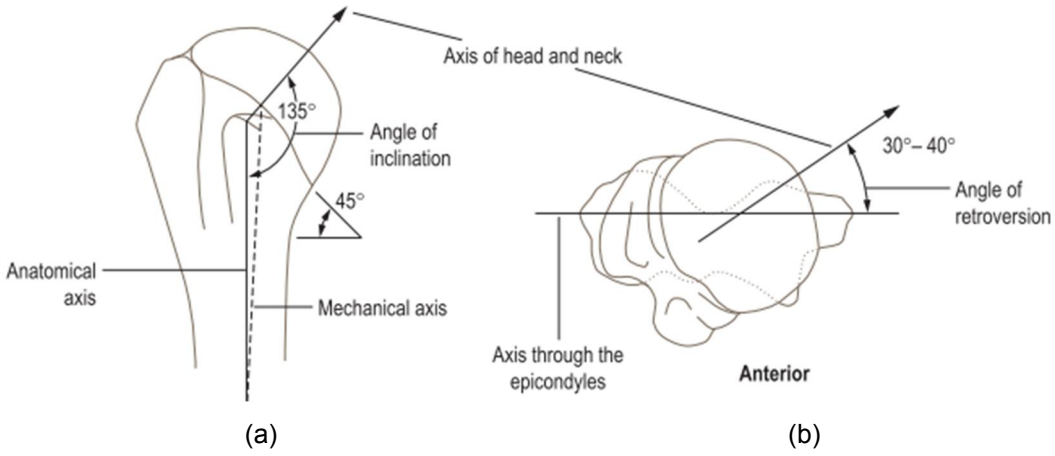

Figure 2-6 – Inclination (a) and retroversion (b) angles of the humerus (Adapted from Palastanga & Soames, 2012).

2.3.1.2. Scapula

The scapula, illustrated in Figure 2-7, is a large, flat, and triangular bone located in the posterior part of the thorax. The site of articulation with the clavicle is called acromion, which is situated at the lateral extremity of the spine. The spine is a sharp crest situated in the posterior surface of the scapula's body. The glenoid cavity, or glenoid fossa, is a depression located inferior to the acromion that articulates with the humeral head, forming the shoulder joint (Tortora & Derrickson, 2012).

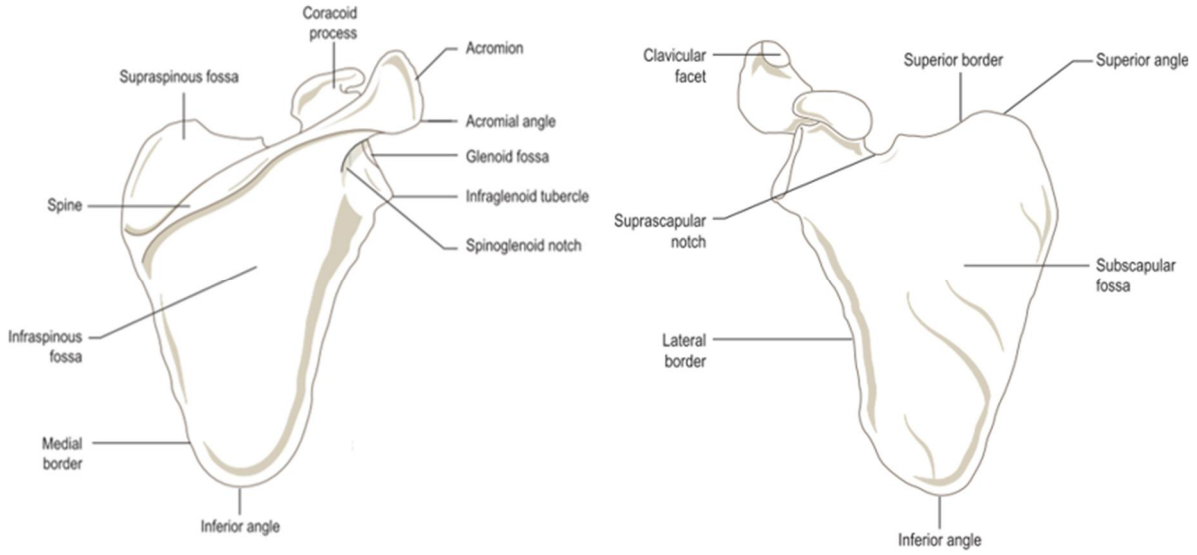

(a) (b)

Figure 2-7 – Posterior (a) and anterior (b) views of a right scapula (Adapted from Palastanga & Soames, 2012).

2.3.2. Articular system

Considering its structure, the shoulder joint is classified as a synovial joint, while considering its function, it is a diarthrosis. Given its structure, the shoulder joint is further classified as being of the type ball-and-socket, as the ball-shaped head of humerus fits into the cup-like glenoid cavity. This type of joint allows movements in the 3 axes, so that it is a multiaxial joint (Tortora & Derrickson, 2012).

As a synovial joint, the shoulder joint is surrounded by an articular capsule. The ligaments that strengthen the capsule are called capsular ligaments, being divided into glenohumeral ligaments and the transverse humeral ligament. The glenohumeral ligaments are 3 longitudinal bands of fibres, which reinforce the anterior part of the articular capsule: superior, middle, and inferior glenohumeral ligaments. Composed of transverse fibers of the articular capsule, the transverse humeral ligament links the greater and lesser tubercles of the humerus. Besides the capsular ligaments, 2 other ligaments are considered as accessory ligaments. The coracohumeral ligament merges with the articular capsule, while the coracoacromial ligament forms along with the coracoid and acromion processes a fibro-osseous arch superior to the humeral head (Palastanga & Soames, 2012). These ligaments are depicted in Figure 2-8.

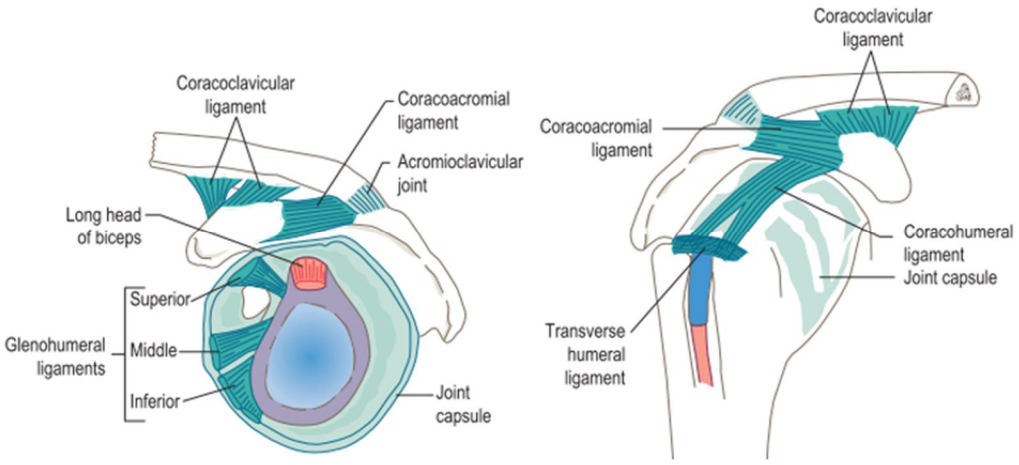

Figure 2-8 – Ligaments of the articular capsule of the shoulder: (a) lateral view of the glenoid cavity, with the humeral head supressed to allow the visualization of the glenohumeral ligaments, and (b) representation of the transverse humeral ligament, and coracohumeral and coracoacromial ligaments (Adapted from Palastanga & Soames, 2012).

Due to its geometry, the shoulder joint permits a wide range of movements, being even the joint, within the human body, with the greater range of movement. Although movements can occur around an infinite number of axes crossing the humeral head, the motions of the shoulder joint are commonly decomposed into movements in the 3 cardinal planes, as illustrated in Figure 2-9. The main movements in the coronal plane are abduction and adduction, in the sagittal plane are flexion and extension, and in the transverse plane are medial and lateral rotation (Palastanga & Soames, 2012).

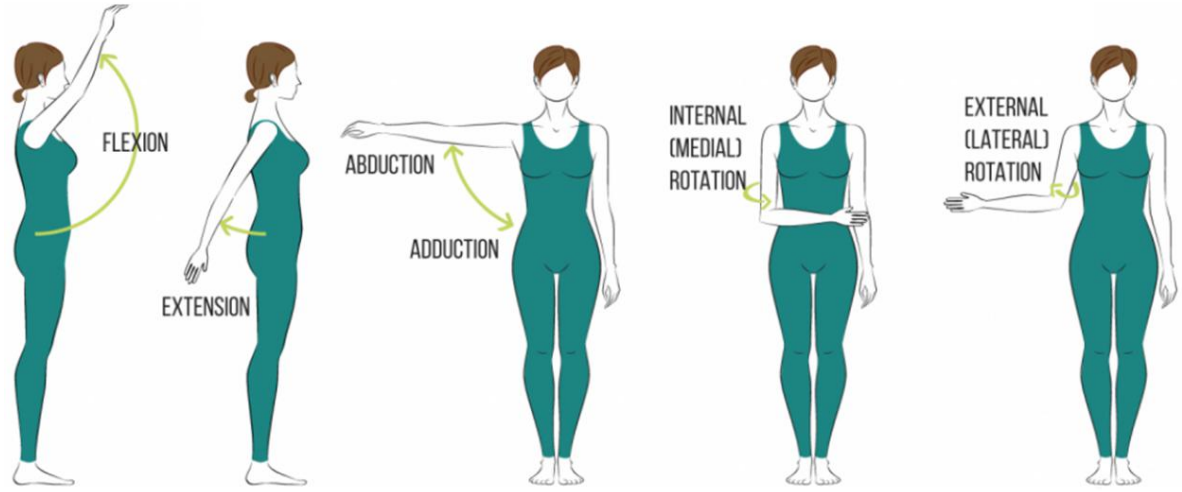

Figure 2-9 – Movements of shoulder joint: (a) Flexion and extension, (b) adduction and abduction, and (c) medial and lateral rotation (Adapted from “Movements of shoulder joint,” 2016).

2.3.3. Muscular system

The shoulder complex involves the action of several muscles, as illustrated in Figure 2-10, all of which play an essential role in the shoulder movement. In addition to promoting motion at the shoulder joint, some muscles act as dynamic stabilizers of the joint by compressing the humeral head against the

glenoid cavity. The main stabilizers of the shoulder joint are the supraspinatus, infraspinatus, teres minor and subscapularis muscles, which compose the rotator cuff (Gasbarro et al., 2017).

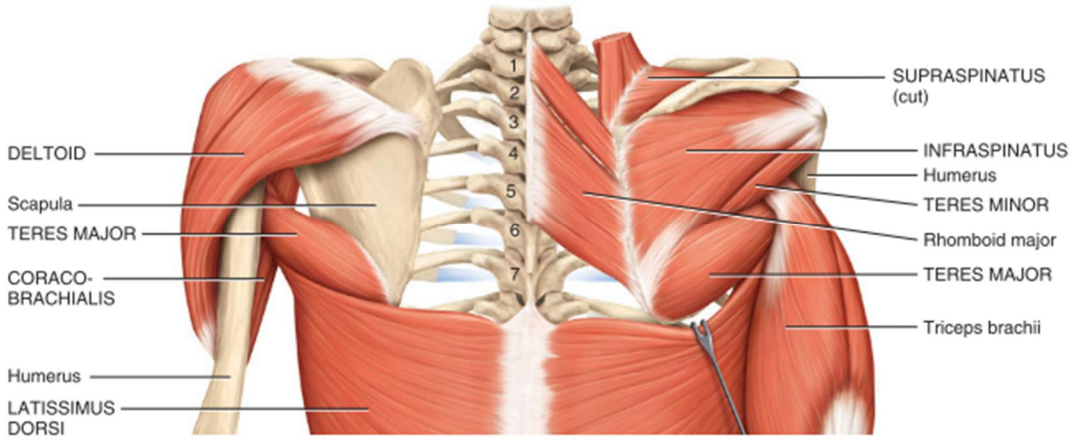

(a)

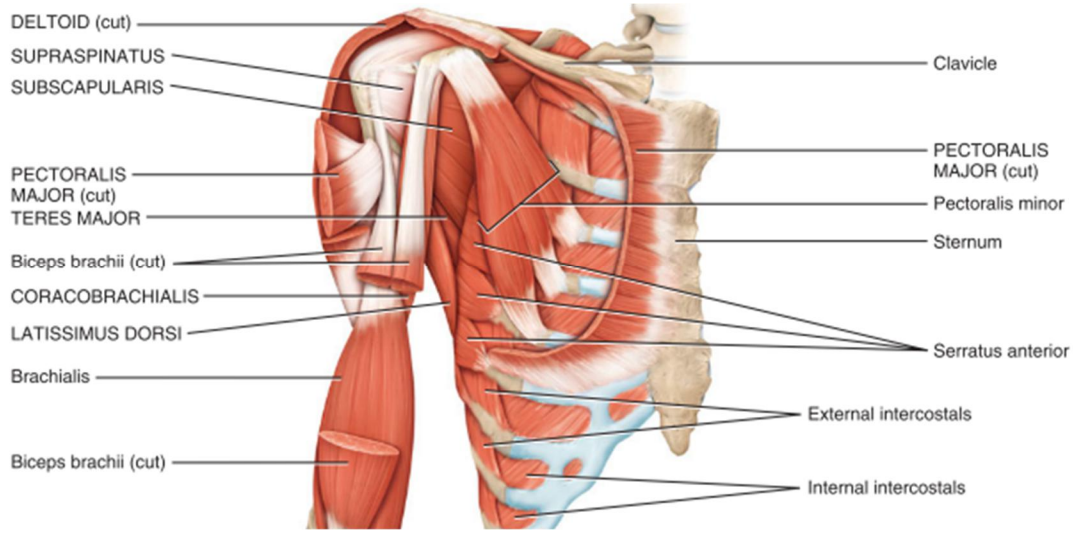

(b)

Figure 2-10 – Posterior (a) and anterior (b) views of the upper limb muscles involved in the humerus movement (Retrieved from Tortora & Derrickson, 2012).

2.4. Shoulder arthroplasty

Although the first report of a shoulder arthroplasty refers to 1893, and to a French surgeon named Jules-Émile Péan, the pioneer of the modern shoulder arthroplasty was Charles S Neer II in the 1950s (Sheridan et al., 2012). Since that time, the shoulder arthroplasty has continuously evolved. The aim of this section is to present a brief overview about the type of shoulder arthroplasties and implant options available.

2.4.1. Types of shoulder arthroplasties

Shoulder arthroplasties are indicated for patients experiencing shoulder pain and decreased range of motion that compromises their daily routine activities. These symptoms may be caused by primary glenohumeral osteoarthritis, post-traumatic arthritis, rheumatoid arthritis, osteonecrosis, arthritis due to

shoulder instability or prior shoulder instability surgery, and rotator cuff tear arthropathy (Mata-Fink & Bell, 2016). According to each indication, shoulder arthroplasties can be divided into 3 main categories: hemiarthroplasty, total shoulder arthroplasty (TSA), and reverse total shoulder arthroplasty (RTSA) illustrated in Figure 2-11 (Sheridan et al., 2012).

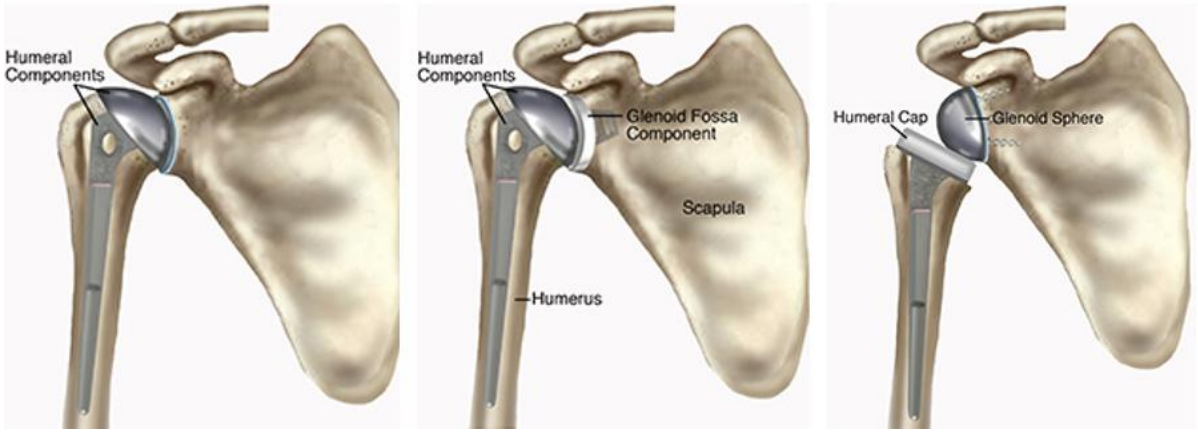

(a) (b) (c)

Figure 2-11 – Types of shoulder replacement: (a) Hemiarthroplasty, (b) total shoulder arthroplasty, and (c) reverse total shoulder arthroplasty (Adapted from “Total Shoulder Arthoplasty,” n.d.).

Hemiarthroplasty, illustrated in Figure 2-11 – (a), is indicated whenever the glenoid cannot be replaced, which can be due to glenoid dysplasia, bone loss or high risk of glenoid loosening, just to name a few reasons. Accordingly, it is an approach that maintains the glenoid intact, and it may involve either resurfacing or replacement of the humeral head. The resurfacing technique is appropriate for osteoarthritis (OA) or avascular necrosis (AVN) in cases where the glenoid articular surface is well preserved, and the humeral head presents only moderate deformity. On the other hand, when the humeral head presents significant bone loss or osteoporosis, an humeral head replacement is indicated (Sheridan et al., 2012).

In the event of both humeral head and glenoid presenting articular cartilage loss with an intact and functioning rotator cuff, a TSA is indicated, illustrated in Figure 2-11 – (b). It is important to ensure the existence of suitable bone stock in the glenoid, otherwise a hemiarthroplasty should be performed. Short- and medium-term studies show superior outcomes for TSA than for hemiarthroplasty. At 10 years, a 92 % glenoid survival rate is reported (Sheridan et al., 2012).

The third mentioned technique, RTSA, illustrated in Figure 2-11 – (c), consists of reversing the natural configuration of the shoulder joint, i.e., the socket becomes a ball and vice-versa. The use of this approach is indicated for cuff tear arthropathy, trauma surgery, revision shoulder arthroplasties, and glenohumeral instability secondary to rotator cuff failure. This configuration constrains the implant, allowing a lengthening of the deltoid lever arm. Despite having a high complication rate, there is evidence of significant improvements in both pain relief and function (Sheridan et al., 2012).

2.4.2. Shoulder implants options

Shoulder implants may be grouped into 4 different generations according to its configurations. As mentioned before, Neer (1974) introduced the first-generation of shoulder implants. His protheses

consisted of a cobalt alloy single piece (humeral-head monoblock), available in a limited range of sizes. However, fluoroscopic studies demonstrated that this implant had a limited ability to reproduce the natural kinematics of the shoulder joint (Boileau et al., 2006; Sheridan et al., 2012).

Later, in the 1990s, modular implants, the so called second-generation protheses, emerged to match the wide variability of dimensions of the humeral head and medullary canal. Nevertheless, the goal of mimicking the shoulder anatomy was not achieved due to frequently mispositioning and oversizing of the head. In addition to not replicating the shoulder anatomy, new complications appeared such as over-tensioning of the joint and increased wear of the glenoid cartilage or the polyethylene component in a hemiarthroplasty or TSA, respectively. The increased wear might be associated with the alteration of humeral retroversion that originates eccentric loading at the periphery of the glenoid. It could explain the rapid deterioration of the clinical results in patients with second-generation shoulder implants (Boileau et al., 2006).

A better understanding of the anatomical relationships within the glenohumeral joint led to the appearance of the so called third-generation of shoulder implants. These implants allow matching the depth of the head to its diameter and respecting the neck-shaft angle. There is evidence that resecting the humeral head by the anatomical neck, and choosing an appropriate depth of the head to correspond to the retroversion, inclination, and medial and posterior offsets, restores the lever arms of the rotator cuff muscles (Boileau et al., 2006). According to Pearl & Kurutz (1999), the structure and geometry of the natural shoulder joint anatomy is recreated with a greater extent by third-generation implants than by second-generation implants.

The most recent type of shoulder protheses is the stemless implants, known as the fourth-generation of humeral components. The main advantages of stemless protheses are the preservation of bone stock, less stress shielding effect, elimination of diaphyseal stress concentrations, ease of revision surgery, and humeral head placement independent from orthopaedic axis. Bone stock is useful for fixation of periprosthetic humeral fractures and in case of a future revision surgery, which is particularly critical given the increasing number of shoulder arthroplasties in a younger population. The loading focuses on the most proximal humeral bone, reducing the stress shielding effect. The metaphyseal reaming rather than the diaphyseal reaming leads to the absence of diaphyseal stress concentrations which may decrease the rate of fracture. Ease of stem removal facilitates a possible revision, and the humeral head placement independent of the humeral diaphysis allows the reconstruction of the proximal humerus for alignment in deformity surgery (Churchill & Athwal, 2016; Harmer et al., 2016).

Humeral resurfacing prostheses are an additional type of implants. With respect to stemmed implants, the major advantages of resurfacing implants are the minimal removal of bone, allowing an easier revision surgery, and the minimization of the potential risk of humerus' fracture by avoiding stress concentrations. Moreover, they provide a precise reproduction of the shoulder anatomy as far as offset, retroversion and inclination are concerned. Despite the good initial clinical results, equivalent to those of stemmed implants, a rate of loosening of 25 % at a mean of 4.2 years following surgery is reported (Boileau et al., 2006). They are not to be confused with stemless implants. Humeral resurfacing

prostheses replace the joint surface with a metal cap, whereas stemless implants consist of a humeral head replacement that anchor exclusively in the humeral metaphysis.

2.4.2.1. Stemless implants

To the author's knowledge, there are 8 manufacturers fabricating stemless prostheses, most of which with its own unique geometry. Hence, a significant variability exists in the geometry of the implants, as described in Table 2-1. Besides the geometry, several characteristics differ among the 10 stemless systems, such as fixation mode, collar type, and bone contact area. The fixation mode in 9 of the implants is impaction, which allows the surgeon to press fit the implants into the prepared metaphyseal bone. The ECLIPSE™ Stemless Shoulder Prosthesis is the only system that offers screw-in fixation. This implant incorporates a threaded central post implanted by screw-in, which allows a compressive force in the metaphyseal region. Regarding the collar type, the systems ECLIPSE™ Stemless Shoulder Prosthesis, GLOBAL ICON™ Stemless Shoulder System, and SIMPLICITI™ Shoulder System have a full, solid, collar which rests on the proximal humeral resection surface. The Eclipse and Global Icon systems are designed to rest on the cortical rim, while the Simpliciti rests on the trabecular bone inside the cortical rim. The implants Easytech™ anatomical, Sidus™ Stem-Free Shoulder and Unic® Stemless have an open window ring collar which rests on the trabecular bone of the resection surface. All the remaining implants are collarless. The implants presenting a high bone-implant contact area are characterized by having solid collars and solid fins. Moreover, a low bone-implant contact area is associated with either an open collar or the absence of it, and open-windowed fins (Churchill & Athwal, 2016).

Table 2-1 – Key features of stemless arthroplasty implants. The fixation types S and I refer to Screw-in and Impaction, respectively. The Morse taper types M and F refer to Male and Female, respectively (Adapted from Churchill & Athwal, 2016).

	Arthrex	**Zimmer Biomet**			**FX Solutions**	**Lima**	**Matheys**	**Wright Medical**	**Depuy Synthes**	**Evolutis**
	Eclipse	TESS	Nano	Sidus	Easytech	SMR Stemless	Affinis Short	Simpliciti	Global Icon	Unic Stemless
Introduced	2005	2004	2013	2012	2015	2015	2008	2010	2017	Not available
FDA approval	No	No	No	Yes	No	No	No	Yes	No	No
2-year minimum follow-up report	Yes	Yes	No	Yes	No	No	No	Yes	No	No
8-year minimum follow-up report	Yes	Yes	No	No	No	No	No	No	No	No
Fixation	S	I	I	I	I	I	I	I	I	I
Collar type	Solid	None	None	Open	Open	None	None	Solid	Solid	Open
Bone contact area	High	High	High	Low	Low	High	Low	High	High	High
Morse taper	M	M	F	M	F	M	M	F	F	M
Component pieces	3	3	2	2	3	4	2	2	2	2
Convertible	No	No	Yes	No	No	Yes	No	No	No	No

The implants to be analysed in this study are the ECLIPSE™ Stemless Shoulder Prosthesis from Arthrex, GLOBAL ICON™ Stemless Shoulder System from DePuy Synthes, SMR® Stemless from Lima, SIMPLICITI™ Shoulder System from Wright Medical, and Sidus™ Stem-Free Shoulder from Zimmer, all of which are illustrated in Figure 2-12.

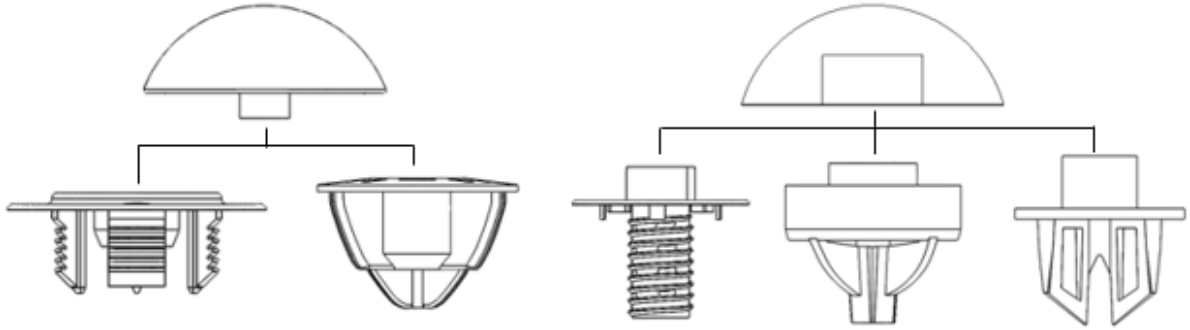

Figure 2-12 – Representation of the stemless implants to be studied in this work: (a) Global Icon, (b) Simpliciti, (c) Eclipse, (d) SMR, and (e) Sidus.

Table 2-1 shows that there is a lack of clinical and radiologic reports for most stemless shoulder systems. Regarding the TESS anatomic prosthesis (Biomet Inc, Warsaw), Huguet et al. (2010) reported comparable functional results to those of classical prostheses, and radiologic evidence of maintained implant stability 3 years after the arthroplasty. No signs of radiolucencies, osteolysis, and stress shielding were reported around the implant. Maier et al. (2015) described early stemless functional and proprioceptive outcomes comparable to those of standard stemmed prostheses in patients with glenohumeral osteoarthritis. In 2017, Spranz et al. compared the functional results of stemless and stemmed arthroplasties, obtaining similar results regarding active range of motion and Constant score for both types of implants. Additionally, after a long-term follow-up of 8 years, Beck et al. (2018) concluded that this stemless implant showed significant improvements in clinical scores. There were no signs of radiographic loosening of the humeral component, and the survivorship rate of the implant was 93.5 % at 8 years. Studies addressing the TESS reverse system demonstrated that stemless RSA did not feature inferior clinical outcomes than stemmed RSA at short to mid-term follow-up, although further long-term studies are needed to assess its definite performance (Kadum et al., 2011; Ballas & Béguin, 2013; Moroder et al., 2016).

Regarding the ECLIPSE™ system (Arthrex, Karlsfeld, Germany), Habermeyer et al. (2015) concluded that the functional and radiologic results of this stemless system were comparable to those of standard stemmed systems at a mean follow-up of 72 months. Yet, bone resorption in the proximal humerus was observed in 41.3 % of the patients. The first long-term study on the effectiveness of stemless protheses became available only in 2017. It consisted in an evaluation of clinical and radiologic outcomes 9 years following the stemless arthroplasty. The authors concluded that the outcomes were comparable to those of third and fourth generation standard shoulder arthroplasties. However, bone mineral density loss in radiographs of the humerus was reported in 29.4 % of patients (Hawi et al., 2017). Moreover, although further investigation is needed, there is evidence that deep infections may be more frequent following implantation of the ECLIPSE™ system than with other conventional stemmed implants (Johansson et

al., 2017). Later, Heuberer et al. (2018) reported no loosening of the humeral head during a follow-up of 58 months, even though internal stress shielding (loss in bone density around the hollow screw) was seen in 42.5 % of patients. Nonetheless, the clinical mid-term outcome after stemless implantation was not affected by the radiological changes. Gallacher et al. (2018) also reported excellent functional and radiographic outcomes at 2 to 6 years' follow-ups.

Concerning the SIMPLICITI™ system (Wright Medical, formerly Tornier), Churchill et al. (2016) demonstrated good results at a minimum of 2 years of follow-up. The clinical results evaluated were the range of motion and the Constant, Simple Shoulder Test, and American Shoulder and Elbow Surgeons scores, which improved significantly. Radiologically, there was no evidence of loosening, osteolysis, or subsidence of the humeral components or surviving glenoid components.

Recently, Krukenberg et al. (2018) reported short-term results for the Sidus™. Outcomes after a 2 years' follow-up showed neither migration nor loosening in radiologic results, which together with the good clinical outcomes are comparable with other stemless protheses. A lower bone density was reported in 3.8 % of patients.

Besides the good results obtained for primary stemless arthroplasties, Vanhees et al. (2013) concluded that performing a revision of a humeral component with a stemless system is technically possible with good functional and radiologic outcomes. Moreover, it can be considered for younger patients in case of preserved metaphyseal humeral bone stock.

There is evidence that the stemless anatomical arthroplasty has equivalent clinical and radiologic results to the standard stemmed arthroplasty. Nevertheless, the complications reported in the literature, such as reduction in bone density, and the lack of long-term studies addressing more implants prevent general and definite recommendations, especially considering the significant design differences in the available stemless implants. Accordingly, further investigation is needed to increase knowledge about the performance of stemless implants (Churchill & Athwal, 2016).

2.5. Background on biomechanical modelling

Since more than 4 decades ago that joint replacements are studied and evaluated using the finite element method to improve the understanding of the performance of the bone-implant system, or of a specific device. The development of complex finite element models intends to assist the design and pre-clinical testing of new prostheses, as well as to compare their performance with existing designs. Besides the mechanical performance, biological processes that are affected when a joint is replaced may also be addressed, such as bone remodelling, fracture healing and osteoporosis. An emerging application is the use of the finite element method as a decision support tool for the planning of orthopaedic surgeries, providing information about function and potential risk of failure on a patient-specific way (Prendergast, 1997; Taylor & Prendergast, 2015).

There are several complications, regarding joint replacements, which can be addressed by finite element models, such as wear damage accumulation of the cement mantle, debonding of the stem-cement

interface and cement-bone-interface, osseointegration, bone adaptation (bone remodelling), and contact mechanics, just to name a few (Taylor & Prendergast, 2015). Additional finite element studies on joints' kinematics and contact mechanics, under dynamic conditions, have also been performed (Halloran et al., 2005). Focusing on the bone remodelling studies, these have been used to evaluate the bone adaption process after a joint replacement, addressing the hip, knee, and shoulder joints (Fernandes et al., 2002; Gupta et al., 2006; Quental et al., 2012b; Sharma & Robertson, 2013; Quilez et al., 2017).

Historically, most joint arthroplasties affect the hip and knee. Consequently, a vast number of numerical simulations have focused on these joints due to the interest of clinical and industrial researchers. Perhaps because of its complexity, the number of studies addressing the shoulder joint is small, especially compared to the hip and knee. Nevertheless, the increase of shoulder arthroplasties over the last decade, associated with the persistence of several complications that can be addressed using numerical models, improvements in software and computational power, raised the amount of shoulder numerical simulations (Favre et al., 2009). The majority of shoulder joint studies focus on the scapula, especially on the glenoid as the aseptic loosening of the glenoid component is one of the main complications of the total shoulder arthroplasty (Bohsali, 2006). In contrast, the humerus has been less studied than the scapula.

Regarding finite element studies addressing the humerus, Pressel et al. (2000) evaluated the stress distribution in the humerus after a stemmed hemiarthroplasty using finite element models, and reported the occurrence of stress shielding due to the relatively stiff shaft of the implant. Quental et al. (2012b) addressed the bone remodelling process of the humerus after a stemmed total shoulder arthroplasty, considering different conditions for the load, bone quality, and bone-cement and bone-implant interfaces. Despite still being scarce, computational studies addressing stemless implants have recently been performed. Razfar et al. (2015) compared the proximal humeral bone stresses between stemless, short stemmed, and standard stemmed generic implant models, concluding that a reduction in stem length originated cortical stresses that better mimicked the intact humerus, which could be responsible for the reduction of stress shielding in the proximal humerus. Favre & Henderson (2016) assessed the micromotion of the stemless implant Sidus™ during upper limb activities. For 99 % of the activities evaluated, the micromotions computed were below the threshold after which bone ingrowth no longer occurs. Reeves et al. (2018) reported the effect of stemless humeral component fixation designs on bone stress and strain response, but only generic geometries were considered in their study. Among others, one variable measured was the simulated potential bone response at the stage immediately after the surgery, computed by the percentage of bone volume that would be expected to resorb, remain unchanged, or remodel based on the strain energy density changes between the implanted and intact models. The fixation feature geometry of the implant was seen to influence the simulated humeral bone response: centrally pegged implants caused low simulated resorbing potentials in cortical and trabecular bones, with boundary-crossing implants showing the highest simulated trabecular remodelling potentials. Santos et al. (2018) compared the bone remodelling process of the humerus after a stemless and a resurfacing shoulder arthroplasty. However, only a single geometry of a stemless implant, based

on Sidus™, was evaluated. Compared to the resurfacing implant studied, Santos et al. (2018) concluded that the stemless implant considered caused less bone resorption at the fixation site, which could suggest a better long-term fixation of the stemless implant. To the author's knowledge, there is no study addressing the effect of distinct stemless humeral component fixation designs, available in the market, on the humeral bone adaptation process.

2.6. Novel aspects of the work

To the author's knowledge, this is the first study to perform such an extensive evaluation of the impact of the geometry of 5 stemless implants, available in the market, on the bone adaption process of the humerus after a shoulder arthroplasty. Moreover, it overcomes the limitations addressed by Reeves et al. (2018), i.e., the bone remodelling process was effectively simulated. Five geometries of stemless implants were modelled and used to develop three-dimensional finite element models, which can also be used in future studies, contributing for further investigation on the performance of stemless implants. Despite being more focused on collared implants, this study also addresses an issue raised by Churchill & Athwal (2016), who mentioned the necessity to assess whether the collar, and possibly the open window ringed collar, distributes stress more properly to the proximal metaphyseal bone and avoids stress shielding.

3. Bone remodelling model

Mathematical models that describe the bone behaviour when it is subjected to changes in loading conditions are crucial to better understand the bone adaptation process related to the mechanical behaviour. Over the last decades, several authors have proposed mathematical models of bone remodelling. A group of these models considers bone as a linear elastic material with changes in bone density as a function of local mechanical stimuli. Other models apply structural optimization methods to compute the optimal distribution of a cellular material presenting a variable density (Fernandes et al., 1999). The bone remodelling model used in this work was developed by Fernandes et al. (1999). It assumes the trabecular microstructure as orthogonal elements strictly oriented in 3 orthogonal directions. This model is based on Wolff's trajectorial theory, which affirms that processes such as bone growth and fracture healing produce trabeculae oriented with respect to the directions of principal stress. The mathematical formulation of the bone adaptation process, including the material model and the optimization problem from which the bone remodelling law is derived is briefly presented next.

3.1. Material model

The bone remodelling model assumes trabecular bone as a cellular material, with its microstructure being modelled as the periodic repetition of a unit cell. In this study, the configuration of the unit cell is cubic with throughout rectangular holes with dimensions a_1, a_2 and a_3. These open cells were introduced in the original model by Folgado et al. (2004), aiming to better approximate the trabecular bone microstructure by conferring to it a higher porous character. As the modelled cellular material is orthotropic, it allows the simulation of bone as an oriented material.

For each point within the body, the microstructure is characterized by its relative density and orientation, computed through the parameters $\mathbf{a} = [a_1, a_2, a_3]^T$ and Euler angles $\boldsymbol{\theta} = (\theta_1, \theta_2, \theta_3)^T$, respectively, as illustrated in Figure 3-1. The relative density ρ_r depends on the cell parameters and is obtained by:

$$\rho_r = 1 - a_1 a_2 - a_1 a_3 - a_2 a_3 + 2a_1 a_2 a_3 \tag{3-1}$$

where $a_i \in [0,1]$ and $i = 1,2,3$. Cortical bone is obtained for $a_i = 0$ whereas a value of $a_i = 1$ corresponds to void.

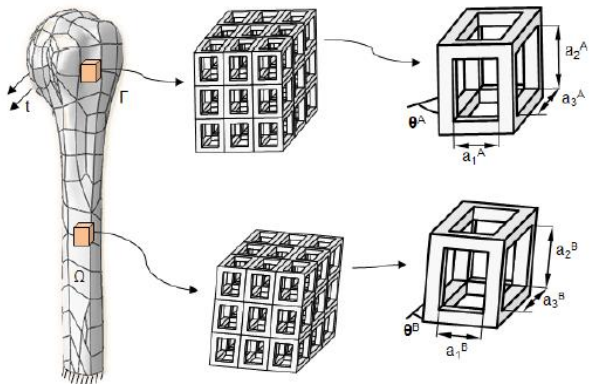

Point A
$$\begin{cases} \rho_r^A = 1 - a_1^A a_2^A - a_1^A a_3^A - a_2^A a_3^A + 2a_1^A a_2^A a_3^A \\ \boldsymbol{\theta}^A = (\theta_1^A, \theta_2^A, \theta_3^A) \end{cases}$$

Point B
$$\begin{cases} \rho_r^B = 1 - a_1^B a_2^B - a_1^B a_3^B - a_2^B a_3^B + 2a_1^B a_2^B a_3^B \\ \boldsymbol{\theta}^B = (\theta_1^B, \theta_2^B, \theta_3^B) \end{cases}$$

Figure 3-1 – Material model of bone (Adapted from Santos, 2017).

The material elastic properties are computed using the homogenization method. In homogenization theory it is assumed that the material properties are periodic functions of the microscopic variable, when compared with the overall macroscopic variable. For a homogeneous base material, cortical bone in this study, the homogenized elastic material properties $\mathrm{E}^{\mathrm{H}}_{ijkm}$ are mathematically expressed as follows:

$$\mathrm{E}^{\mathrm{H}}_{ijkm} = \frac{1}{|Y|}\int_{¥}\left(\mathrm{E}_{ijkl} - \mathrm{E}_{ijpm}\frac{\partial X_p^{kl}}{\partial\, y_m}\right)dy \tag{3-2}$$

where E_{ijkl} represents the elastic material properties of the base material, Y corresponds to the volume of the unit cell, ¥ is the solid part of the cell, and X^{kl} are a set of periodic functions, which result from the solution of 6 equilibrium equations defined within the microstructure. This method is fully described in Guedes & Kikuchi, (1990).

3.2. Optimization problem

A general structural optimization problem usually consists in minimizing the structural compliance, i.e., maximizing the structural stiffness, subjected to a constraint on volume (or mass). However, in the context of bone remodelling, the constraint on volume is not appropriate because bone is an open system with respect to mass. Consequently, instead of constraining bone volume or mass, an additional term was introduced in the objective function to consider the cost of bone maintenance. This term is controlled by the parameter k, which represents the metabolic cost to the organism of maintaining bone tissue (Fernandes et al., 1999). Considering the design variables $\mathbf{a}$ and $\boldsymbol{\theta}$ that characterize the body's microstructure, the objective function can be expressed as:

$$\min_{\mathbf{a},\boldsymbol{\theta}}\left\{\sum_{P=1}^{NC}\alpha^P\left(\int_{\Gamma} t_i^P\, u_i^P\; d\Gamma\right) + k\int_{\Omega}\rho_r(\mathbf{a})^m\, d\Omega\right\} \tag{3-3}$$

subjected to:

$$\begin{gathered} 0 \le a_i \le 1, i = 1{,}2{,}3 \\ \int_{\Omega}\mathrm{E}^{\mathrm{H}}_{ijkl}(\mathbf{a},\boldsymbol{\theta})\varepsilon_{ij}(\mathbf{u}^P)\varepsilon_{kl}(\boldsymbol{\upsilon}^P)\, d\Omega = \int_{\Gamma} t_i^P\, u_i^P\, d\Gamma \end{gathered} \tag{3-4}$$

where NC is the number of applied load conditions with the load weight factors α^P, satisfying $\sum_{P=1}^{NC}\alpha^P = 1$. The variable Ω is the volume occupied by the structure with boundary Γ, having the surfaces loads $\mathbf{t}^P$, and the corresponding displacements fields $\mathbf{u}^P$ applied to it. The variable ρ_r is the relative density, and the parameter m represents a corrective factor for the preservation of intermediate densities (Folgado, 2004). In Equation (3-4), $\boldsymbol{\varepsilon}$ is the strain field and $\boldsymbol{\upsilon}^P$ represents the virtual displacements. Both parameters k and m are crucial in the adjustment of the model to different biological scenarios. An increase in the parameter k reflects a high bone maintenance cost leading to a bone structure with a lower bone mass. On the other hand, an increase in the parameter m prevents the formation of regions with extreme densities, increasing the intermediate density regions (Quental et al., 2014b). Concluding, this optimization formulation reflects the balance between terms representing mechanical advantage and metabolic cost, as the first term of the Equation (3-3)

corresponds to a weighted average of the structural compliance for each load case, and the second term is associated with the metabolic cost of bone tissue maintenance (Fernandes et al., 1999).

The stationary conditions of the optimization problem expressed in Equations (3-3) and (3-4) with respect to the design variables $\mathbf{a}$ and $\boldsymbol{\theta}$ are mathematically expressed as:

$$\sum_{P=1}^{NC}\left[-\alpha^{P}\int_{\Omega}\frac{\partial \mathrm{E}_{ijkl}^{\mathrm{H}}(\mathbf{a},\boldsymbol{\theta})}{\partial \mathbf{a}}\varepsilon_{ij}(\mathbf{u}^{P})\varepsilon_{kl}(\boldsymbol{\upsilon}^{P})\,d\Omega\right]+k\int_{\Omega}m\rho_{r}^{m-1}\frac{\partial \rho}{\partial \mathbf{a}}=0 \tag{3-5}$$

and:

$$\sum_{P=1}^{NC}\left[-\alpha^{P}\int_{\Omega}\frac{\partial \mathrm{E}_{ijkl}^{\mathrm{H}}(\mathbf{a},\boldsymbol{\theta})}{\partial \boldsymbol{\theta}}\varepsilon_{ij}(\mathbf{u}^{P})\varepsilon_{kl}(\boldsymbol{\upsilon}^{P})\,d\Omega\right]=0 \tag{3-6}$$

where the displacement field $\mathbf{u}^{P}$ and the adjoint field $\boldsymbol{\upsilon}^{P}$ are computed from the stationary conditions with respect to $\mathbf{u}$ and $\boldsymbol{\upsilon}$, respectively. The bone remodelling law is represented by Equations (3-5) and (3-6). When they are both satisfied, the equilibrium of the bone adaptation process is achieved (Fernandes et al., 1999; Folgado, 2004). For further detail, see Folgado (2004).

3.3. Computational simulation

To solve this computational model, it is necessary to go through an iterative process. First, the homogenized elastic properties are computed for the initial parameters $\mathbf{a}_0$ and $\boldsymbol{\theta}_0$. Then, the finite element method, FEM, is applied to compute the displacement field, which is followed by a check of the necessary optimal conditions. If these conditions are satisfied, the process stops. If they are not satisfied the process continues by updating the parameters $\mathbf{a}_k$ and $\boldsymbol{\theta}_k$ obtained via Equation (3-7), and the process restarts as shown in Figure 3-2. The design variables at each k_{th} iteration are updated by:

$$(\mathbf{a})_{k+1}=\begin{cases}max[(1-\zeta)(\mathbf{a})_k, a_{min}], if\ (\mathbf{a})_k+s(\mathbf{D}_a)_k\le max[(1-\zeta)(\mathbf{a})_k, a_{min}]\\ (\mathbf{a})_k+s(\mathbf{D}_a)_k, otherwise\\ min[(1-\zeta)(\mathbf{a})_k, a_{max}], if\ (\mathbf{a})_k+s(\mathbf{D}_a)_k\ge min[(1-\zeta)(\mathbf{a})_k, a_{max}]\end{cases} \tag{3-7}$$

$$(\boldsymbol{\theta})_{k+1}=(\boldsymbol{\theta})_k+s(\mathbf{D}_\theta)_k$$

where a_{min} and a_{max} are the minimum and maximum boundaries of $\mathbf{a}$, respectively. The parameter s represents the user defined step length of the optimization process. The variables $\mathbf{D}_a$ and $\mathbf{D}_\theta$ correspond to the descent directions of $\mathbf{a}$ and $\boldsymbol{\theta}$, respectively, given by Equations (3-5) and (3-6). Lastly, ζ defines the upper and lower bound constraints in the design variables to prevent large transitions among iterations.

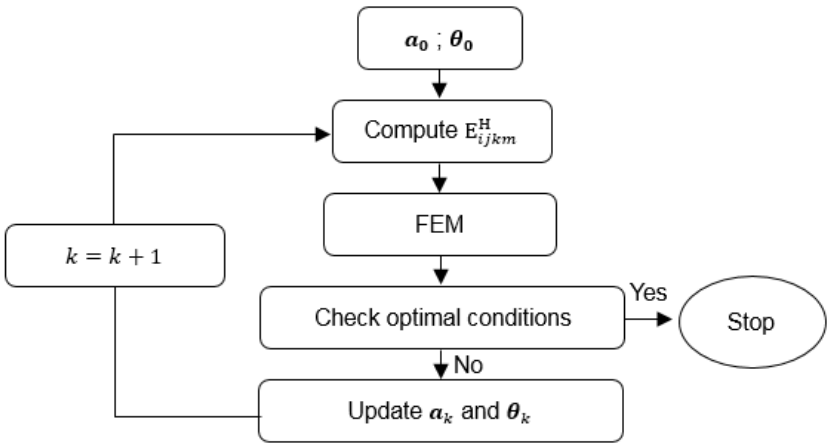

Figure 3-2 – Flow diagram of the bone remodelling computational simulation (Adapted from Fernandes et al., 2002).

4. Computational modelling

This chapter presents a detailed description about the geometric modelling process of the intact bone and implants, the finite element model, the bone remodelling simulations and the methods considered for the analysis of the results.

4.1. Geometric model

In this section, the geometric modelling process followed to obtain the solid model of the intact bone and implants, and the simulation of the virtual arthroplasties is described.

4.1.1. Intact bone

To obtain a three-dimensional (3-D) geometric model of a human body structure, several steps need to be followed: image acquisition, image segmentation, mesh adjustments and solid model generation (Ribeiro et al., 2009). Apart from image acquisition, which was not performed in this work, these steps are further described next.

The 3-D anatomical model of the proximal right humerus was obtained using computed tomography (CT) scan images, from a 38-year-old male cadaver, acquired by the Visible Human Project (VHP) (Spitzer et al., 1996).

4.1.1.1. Image segmentation

Image segmentation is defined as the partitioning of an image into nonoverlapping, constituent regions that are homogeneous with respect to some characteristic such as intensity or texture (Pham et al., 2000). The segmentation process can be performed conjugating 3 techniques: global thresholding, active contour method based on region competition and manual segmentation (Ribeiro et al., 2009).

For this first modelling step, the open-source software ITK-SNAP® (version 3.6.0, 2017) was used. This software allows not only manual segmentation but also semiautomatic segmentation (Yushkevich et al., 2006).

For the application of the global thresholding technique, the user selects 2 intensity values, thresholds, which bound the intensities of the tissue of interest. Hence, thresholding distinguishes the desirable tissue, image foreground, from the undesirable tissue, image background, and thus estimates the region occupied by the tissue of interest. The values of a threshold image are comprehended between -1 and 1.

According to Fat et al. (2012), humerus cortical density varies from 1700 to 2000 Hounsfield Units (HU) and bone marrow and soft tissue have densities of 0 HU. Notice that HU are a quantitative scale for describing radiodensity, which is based on the attenuation values of tissues. Since the humerus medullary canal was not intended to be segmented, the values for the lower and upper thresholds chosen were 100 HU and 1800 HU, respectively, as shown in Figure 4-1.

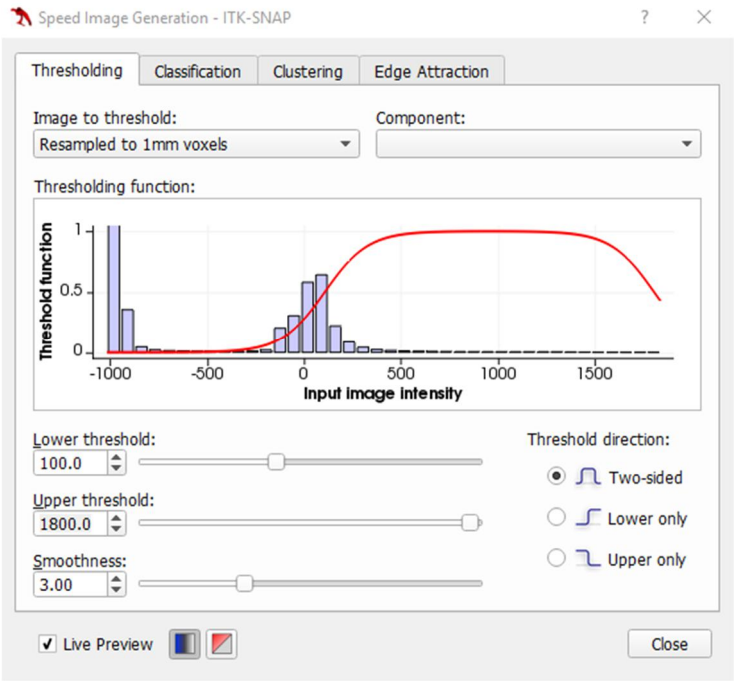

Figure 4-1 – Thresholding definition properties on ITK-SNAP®.

There are some limitations in this process, namely the generation of a coarse image and the inclusion of tissues out of the range of interest, as illustrated in Figure 4-2, due to the partial volume effect. Nonetheless, global thresholding is often used as a pre-processing stage for the application of the active contour method (Ribeiro et al., 2009).

(a) (b)

Figure 4-2 - Coronal section of the right humerus: (a) Original CT scan image, and (b) segmented CT scan image with global thresholding.

The following step is the active contour method based on region competition. This iterative method consists in having closed parametric curves or surfaces, such as spherical bubbles, with physical properties that when submitted to forces, deform adapting to image features. For each iteration, the method calculates internal and external forces. Internal forces are derived from surface geometry ensuring smooth surface variations, whereas external forces lead to bubbles deformation to adjust to the object boundaries, based on the probability of a voxel belonging to the foreground or the background. The process finishes when the user finds a suitable solution or when the spherical bubbles have enclosured all the voxels with greater probability of being part of the foreground (Ribeiro et al., 2009).

Figure 4-3 illustrates the evolution of the active contour method from iteration 0, rough estimate of anatomical structure of interest, to iteration 170 where a suitable solution is found.

Because the result of the active contour method presents some inaccuracies, due to segmentation errors, a manual segmentation was performed to improve the final 3-D model represented in Figure 4-3 – d. To perform this task the user must have *a priori* knowledge about the anatomy of the structure to be modelled. The output generated by ITK-SNAP® is a 3-D surface mesh obtained using the marching cubes algorithm (Ribeiro et al., 2009).

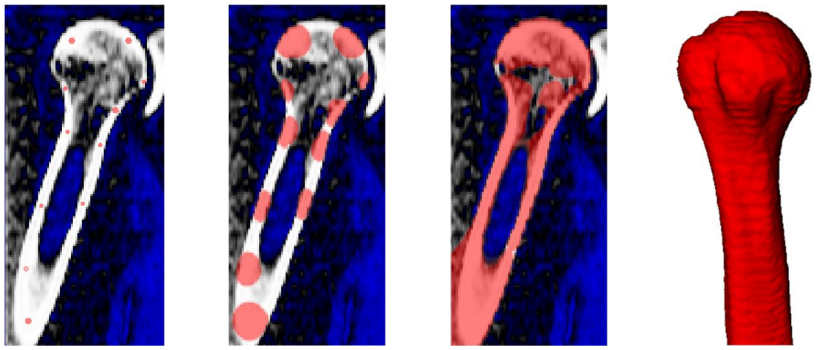

(a) (b) (c) (d)

Figure 4-3 – Segmentation process of the humerus: (a-c) Coronal section of the right humerus for iterations 0, 60, and 170 of the active contour method, and (d) anterior view of the 3-D model.

4.1.1.2. Surface mesh correction

The 3-D surface mesh generated by ITK-SNAP® presents some undesirable features, such as a stair-step shape surface and an excess of nodes and facets, which express inaccurate and irrelevant information about the natural anatomical surface curvature. Therefore, to improve the 3-D surface mesh, an open-source software called MeshLab® (version 2016.12) was used (Cignoni et al., 2008). To supress the undesired features, the duplicate faces, as well as duplicate vertices, zero area faces, and unreferenced vertices were removed. Additionally, a Laplacian smoothing filter was applied to the surface mesh to repair the step-like artefacts and improve the surface mesh appearance (Ribeiro et al., 2009). Figure 4-4 shows the corrections performed to the surface mesh. The adjusted 3-D surface mesh was exported from MeshLab® as a point cloud data file.

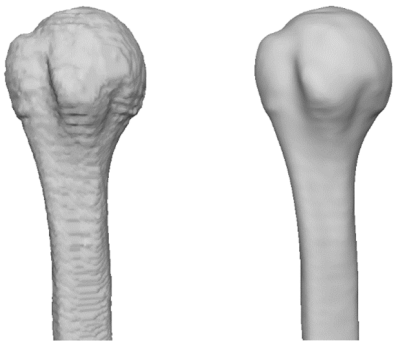

(a) (b)

Figure 4-4 – Anterior view of the 3-D surface mesh in software MeshLab®: (a) 3-D surface mesh obtained from the segmentation process, and (b) smoothed 3-D surface mesh after mesh adjustments.

4.1.1.3. 3-D Solid model

The commercial software Solidworks® (Student Edition, Academic Year 2016-2017) was used to create the 3-D solid model from the 3-D surface mesh generated. This software contains a toolbox, ScanTo3D®, which receives as input a point cloud data file and creates automatically a solid model according the user-defined level of detail (Ribeiro et al., 2009). The feature lines observed in Figure 4-5 represent the surface mesh automatically generated by Solidworks®.

Figure 4-5 – Anterior view of the 3-D solid model of the proximal right humerus obtained using the software Solidworks®.

4.1.2. Implants

For the sake of brevity, a sample of 5 stemless shoulder arthroplasty implants were modelled using the commercial software Solidworks® (Student Edition, Academic Year 2016-2017). Within this sample, all the implants geometries have a significant variability which is believed to give an insight about the geometries commercialized. These models were based on the ECLIPSE™ Stemless Shoulder Prosthesis from Arthrex, GLOBAL ICON™ Stemless Shoulder System from DePuy Synthes, SMR® Stemless from Lima Corporate, SIMPLICITI™ Shoulder System from Wright and Sidus™ Stem-Free Shoulder from Zimmer. For the sake of simplicity, from now on, the modelled implants will be referred as Eclipse, Global Icon, SMR, Simpliciti and Sidus, respectively. Regarding the remaining implants mentioned in Section 2.4.2.1, because both Easytech™ and Affinis® Short systems present similarities in the geometry when compared to the Global Icon and Sidus implants, respectively, they were not analysed. Regarding the 3 implants provided by Zimmer Biomet, only the Sidus™ system was studied due to its relevance, since it was the only implant, among these 3 implants, with FDA approval. The Unic® Stemeless system was not evaluated due to the lack of information in the literature regarding it.

Despite the wide range of configurations among the 5 implants, all the designed models followed the standard geometry, described in this section, to standardize the simulation of the virtual shoulder arthroplasties and eliminate inconsistencies in the results.

Regarding the sizing options, all the dimensions for each implant were chosen according to the recommendations of the manufacturers, the advice of an orthopaedic surgeon, and the literature.

According to Williams et al. (2015) it is better to choose an undersized head than an oversized as long as the criteria for stability are met. Furthermore, Klawitter et al. (2014), states that assuming the articular portion of the humeral head as spherical, the height, *H*, and diameter, *D*, of the humeral head implant component relate with the radius of curvature, *R*, of the humeral head by:

$$R = \frac{D^2 + 4H^2}{8H} \tag{4-1}$$

The dimensions *R*, *D*, and *H* are graphically represented in Figure 4-6. The Equation (4-1) will help to decide the most suitable size for the humeral head implant component for each model.

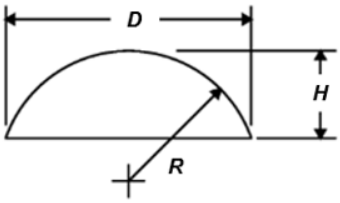

Figure 4-6 – Representation of a segment of a sphere cap illustrating the radius of curvature, *R*, of the sphere, and the height, *H*, and diameter, *D*, of the cap (Adapted from Klawitter et al., 2014).

The radius and centre of the humeral head were estimated in Matlab® (version R2017b, 2017) by fitting a sphere to the humeral head, described by a set of 3-D data points.

4.1.2.1. Eclipse

The first implant model, Eclipse, is based on the ECLIPSE™ Stemless Shoulder Prosthesis, illustrated in Figure 4-7. This is a three-component system: Humeral Head, Cage Screw and Trunion.

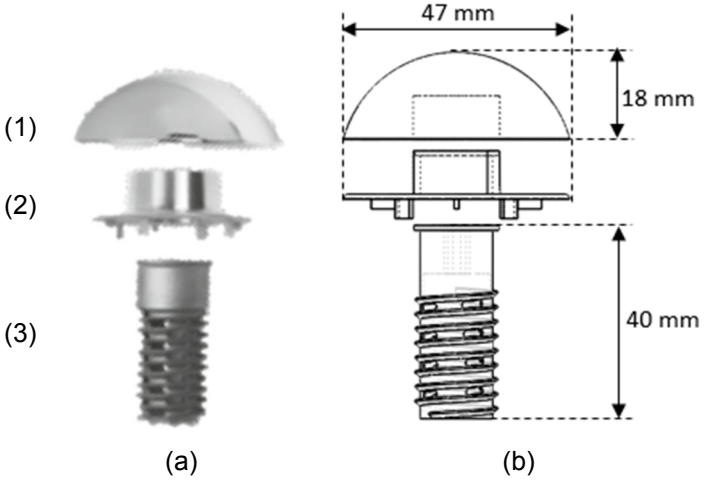

Figure 4-7 - ECLIPSE™ Stemless Shoulder Prosthesis (Adapted from Arthrex, 2018): (a) Front view of (1) humeral head, (2) trunion and (3) cage screw, and (b) computational model with the chosen sizes for the humeral head (*D*=47 mm, *H*=18 mm), trunion (*D*=47 mm) and cage screw (large, *L*=40 mm).

The last 2 components form the humeral implant where the cage screw is inserted over the trunion, and the humeral implant connects to the humeral head by a Morse taper (Churchill & Athwal, 2016). Regarding the sizing options, the 3 components are available in standard sizes, described in Table 4-1,

and the humeral head component is also available, if needed, in a 2 mm elevated version (Arthrex, 2018).

Table 4-1 – Standard ECLIPSE™ Stemless Shoulder Prosthesis sizing options (Arthrex, 2018). The dimensions specified for the humeral head are diameter *D* and height *H*, for the trunion is the diameter *D* and for the cage screw is the component length *L*.

Humeral Head (mm)	*D*	39	41	43	45	47	49	51	53
	H	16	16	16	17	18	18	19	20
Trunion (mm)	*D*	39	41	43	45	47	49	51	53
Cage Screw (mm)	small	medium			large		extra large		
	30	35			40		45		

The model was designed based on Figure 4-7 – (a) (Arthrex, 2018). The surgical technique guide provides some instructions concerning the implant dimensions: the trunion should match the resected plane of the cortical rim as closely as possible, the size of the humeral head must correspond to the size of the trunion, and the length of the cage screw is the distance from the resected surface to the lateral cortex. If the length of the cage screw is between 2 sizes, the shortest size should be chosen (Arthrex, 2018). The most suitable sizing option defined for the humerus being studied is presented in Figure 4-7 – (b).

An illustration of the ECLIPSE™ Stemless Shoulder Prosthesis and the Eclipse computational solid model are presented in Figure 4-8.

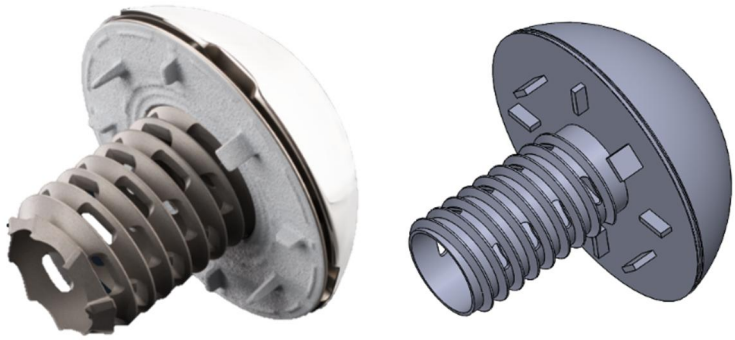

(a) (b)

Figure 4-8 – ECLIPSE™ Stemless Shoulder Prosthesis (Adapted from Arthrex, 2018): (a) Original implant, and (b) Eclipse computational solid model.

4.1.2.2. Global Icon

The second implant model, Global Icon, is based on the GLOBAL ICON™ Stemless Shoulder System, illustrated in Figure 4-9. This is a two-component system: Humeral Head and Anchor Plate. The 2 components are connected by a Morse taper and they are available in several sizes. Besides the standard sizing options for the humeral head and anchor plate implants, presented in Table 4-2, a 3 mm elevated humeral head is also available to allow the anatomical best-fit circle of the proximal humerus (DePuy Synthes, 2017a).

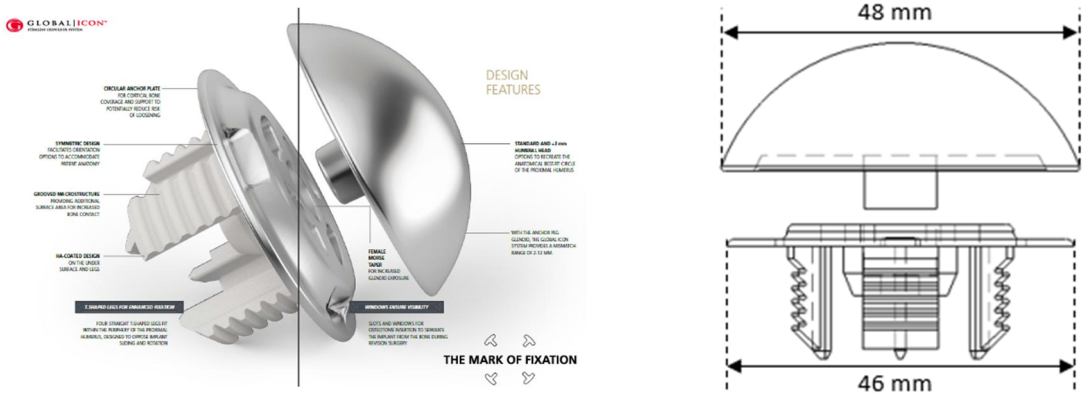

(a) (b)

Figure 4-9 – GLOBAL ICON™ Stemless Shoulder System (Retrieved from DePuy Synthes, 2017a): (a) Original implant, and (b) frontal view of the humeral head and anchor plate of Global Icon computational model with the chosen size for the humeral head (*D*=48 mm) and anchor plate (*D*=46 mm).

The model was designed based on Figure 4-9 – (a) (DePuy Synthes, 2017a). The surgical technique guide provides some instructions concerning the implant dimensions: the anchor plate should provide as much coverage as possible without overhanging the bone, and the humeral head size selected must be equal to or larger than the selected anchor plate (DePuy Synthes, 2017b). The most suitable sizing option for the humerus under analysis is presented in Figure 4-9 – (b).

Table 4-2 - Standard GLOBAL ICON™ Stemless Shoulder System sizing options (DePuy Synthes, 2017b). The dimension specified for the humeral head and anchor plate is the diameter *D*, in millimetres.

Humeral Head	size	40	42	44	46	48	50	52	54	56
Anchor Plate	size	40	42	44	46	48	50	52	54	56

An illustration of the GLOBAL ICON™ Stemless Shoulder System and the Global Icon computational solid model are presented in Figure 4-10.

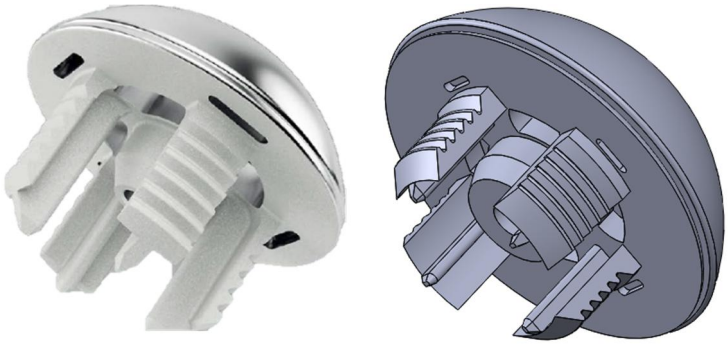

(a) (b)

Figure 4-10 – GLOBAL ICON™ Stemless Shoulder System (Adapted from DePuy Synthes, 2017b): (a) Original implant, and (b) Global Icon computational solid model.

4.1.2.3. SMR

The third implant model, SMR, is based on the SMR® Stemless, illustrated in Figure 4-11. This is a four-component system: Core, Adaptor with Screw and Humeral Head.

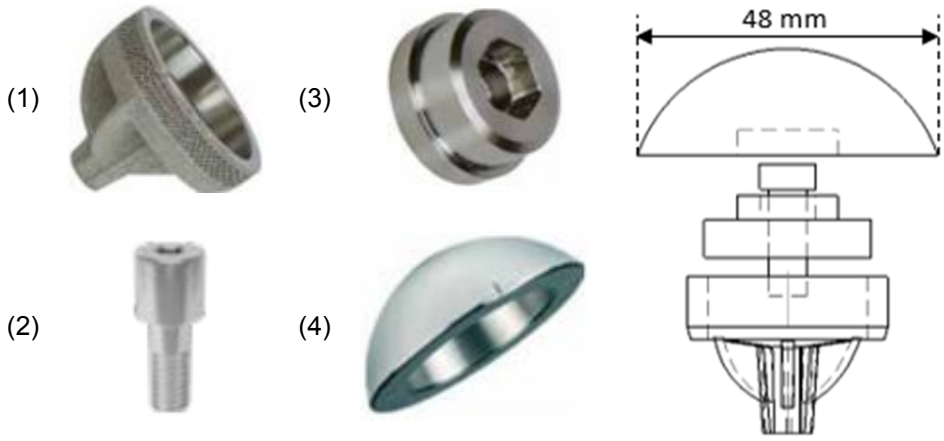

Figure 4-11 – SMR® Stemless (Adapted from Lima Corporate, 2016d): (a) Components of the original implant: (1) core, (2) screw, (3) adaptor, and (4) humeral head, and (b) frontal view of all components of the SMR computational model with the chosen size for the humeral head (*D*=48 mm).

In this system the screw connects the adaptor to the core, while the humeral head is connected to these components by a Morse taper. Regarding the sizing options, the core is available in 4 distinct diameters and in 2 different heights, as shown in Figure 4-12, and the adaptor is available in concentric and eccentric configurations (2 mm and 4 mm).

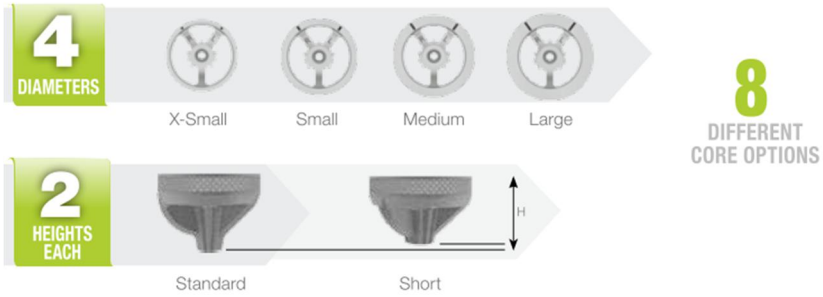

Figure 4-12 – Sizing options for the SMR® Stemless' core component (Retrieved from Lima Corporate, 2016a).

The humeral head is available not only in a standard configuration, described in Table 4-3, but also in a flattened configuration, and in a cuff tear arthropathy (CTA) configuration (Lima Corporate, 2016c). The chosen configurations for the adaptor and humeral head components are concentric and standard, respectively.

Table 4-3 – Available sizing options, diameter *D*, for the standard humeral heads components (Lima Corporate, 2016d).

Humeral Heads (mm)	CoCrMo	40	42	44	46	48	50	52	54
	Ti6Al4V	–	42	44	46	48	50	52	54

The model was designed based on Figure 4-11 – (a) (Lima Corporate, 2016d). The diameter and height of the core were defined considering that it should be centric to the resected humeral surface without involving the cortex (Lima Corporate, 2016d). The most suitable sizing option for the humerus of this study is presented in Figure 4-11 – (b).

An illustration of the SMR® Stemless and the SMR computational solid model are presented in Figure 4-13.

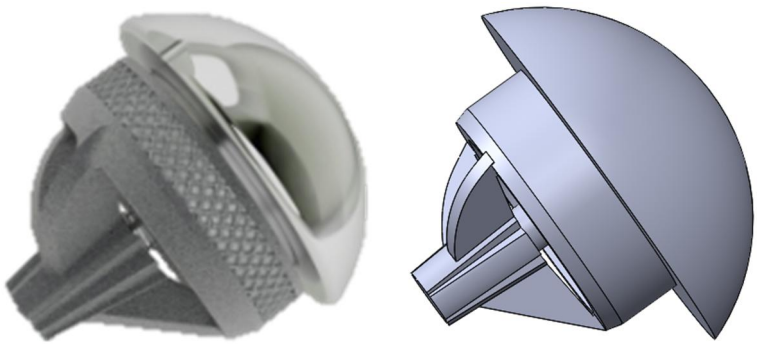

(a) (b)

Figure 4-13 – SMR® Stemless (Adapted from Lima Corporate, 2016b): (a) Original implant, and (b) SMR computational solid model.

4.1.2.4. Simpliciti

The fourth implant model, Simpliciti, is based on the SIMPLICITI™ Shoulder System, illustrated in Figure 4-14. This is a two-component system: Humeral Head and Nucleus that are connected by a Morse taper.

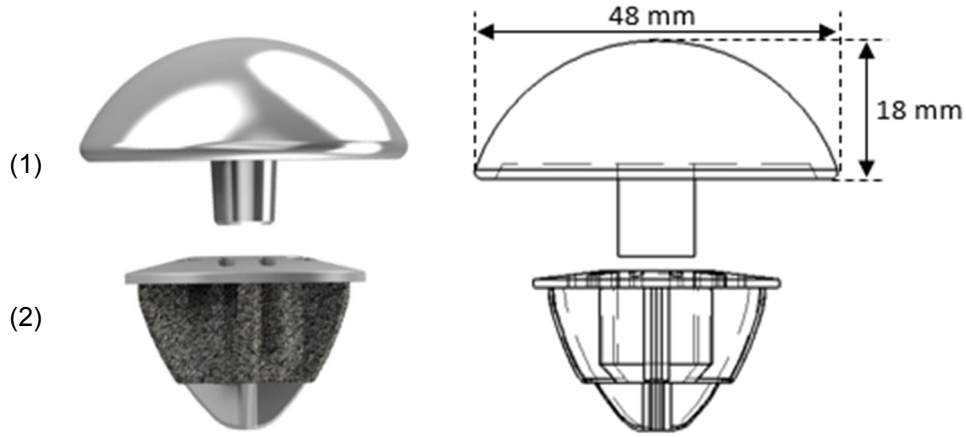

(a) (b)

Figure 4-14 – SIMPLICITI™ Shoulder System (Adapted from Wright, 2017): (a) Front view of (1) humeral head and (2) nucleus, and (b) Simpliciti computational model with the chosen size for the humeral head (*D*=48 mm, *H*=18 mm).

The manufacturer offers 3 distinct sizes for the nucleus whose quantitative dimensions are not available, and several sizes for the humeral head, presented in Table 4-4. In addition to the humeral head standard configuration, a soft-tissue balancing approach (STB) humeral head is also offered.

Table 4-4 – Sizing options for standard humeral heads (Wright, 2016). The specified dimensions for the humeral head are the diameter *D* and height *H*.

SIMPLICITI Humeral Head (mm)	*D*	39	41	43	46	48	50	50	52	52
	H	14	15	16	17	18	16	19	19	23

The model was designed based on Figure 4-14 – (a). The nucleus size was defined as the largest size that did not overhang the humerus at any point (Wright, 2016). The most suitable sizing option for the humerus being studied is presented in Figure 4-14 – (b).

An illustration of the SIMPLICITI™ Shoulder System and the Simplicity computational solid model are presented in Figure 4-15.

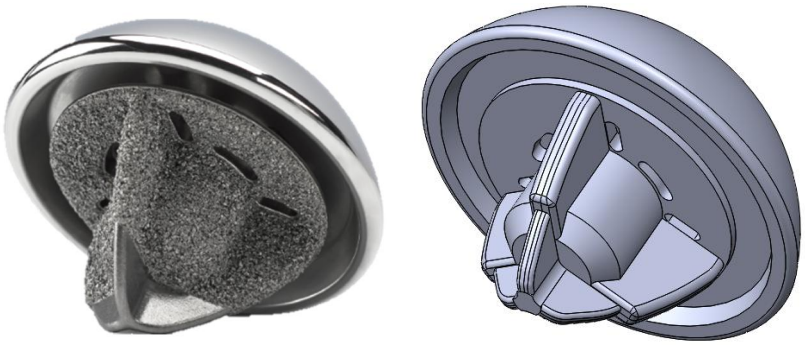

(a) (b)

Figure 4-15 – SIMPLICITI™ Shoulder System (Adapted from Wright, 2017): (a) Original implant, and (b) Simpliciti computational solid model.

4.1.2.5. Sidus

The fifth implant model, Sidus, is based on the Sidus™ Stem-Free Shoulder. This is a two-component system: Humeral Head and Humeral Anchor that are connected by a Morse taper (Churchill, 2014).

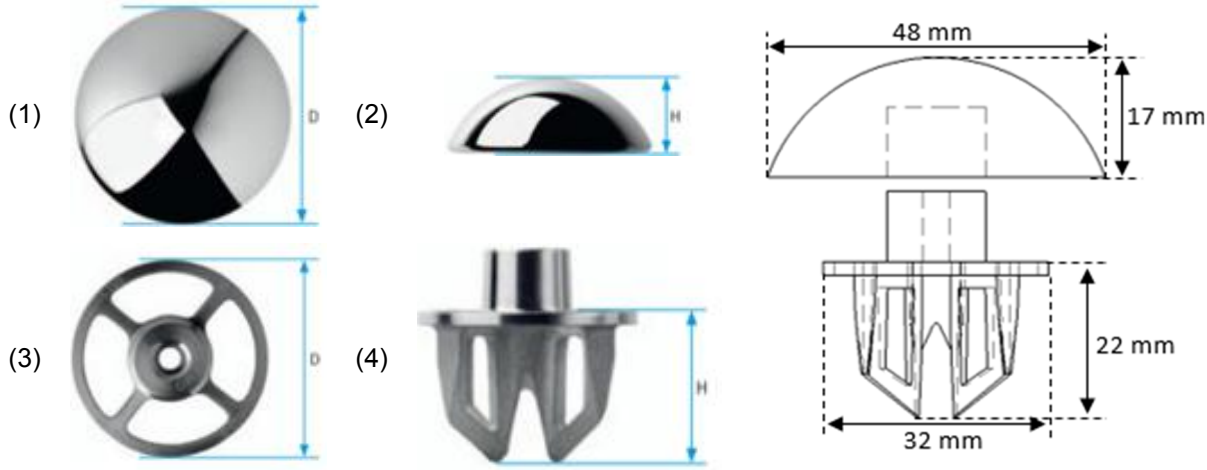

(a) (b)

Figure 4-16 – Sidus™ Stem-Free Shoulder (Retrieved from Zimmer, 2012b): (a) Components of the original implant: (1) Superior view of humeral head, (2) frontal view of humeral head, (3) superior view of humeral anchor, and (4) frontal view of humeral anchor, and (b) Sidus computational model with the chosen sizes for humeral head (*D*=48 mm, *H*=17 mm) and humeral anchor (*D*=32 mm, *H*=22 mm).

The manufacturer offers several sizing options for both components. For each humeral anchor size, only a specific set of humeral head sizes can be used, as shown in Table 4-5. Regarding the humeral anchor, the sizes S, M and L correspond, respectively, to 16 mm, 19 mm and 22 mm in height *H*, and 24 mm, 28 mm and 32 mm in diameter *D.*

Table 4-5 – Sidus™ Stem-Free Shoulder sizing options (Adapted from Zimmer, 2012b). The dimensions specified are the diameter *D* and height *H.*

Humeral Head (mm)	*D*	38	40	42	44	44	46	48	50	52
	H	13	14	15	16	16	16	17/20	18/21	19/23
Humeral Anchor		S				M			L	

The model was designed by Santos (2017), who kindly provided the 3-D geometry. The humeral anchor component provided was used without changes, but the humeral head component was modified to avoid the oversizing of the implant. The most suitable sizing option for the humerus under analysis is presented in Figure 4-16 – (b).

An illustration of the Sidus™ Stem-Free Shoulder and the Sidus computational solid model are presented in Figure 4-17.

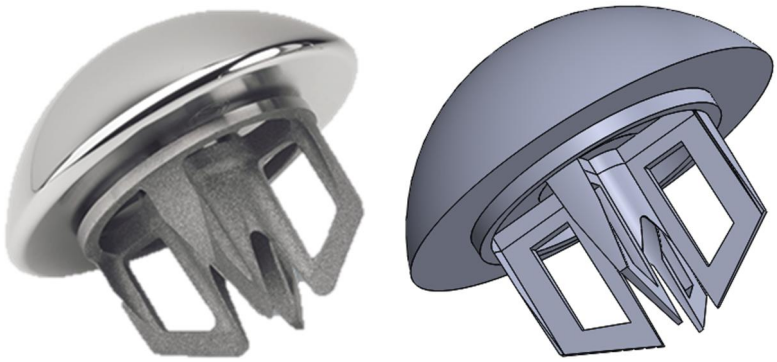

(a) (b)

Figure 4-17 – Sidus™ Stem-Free Shoulder (Adapted from Zimmer, 2014): (a) Original Implant, and (b) Sidus computational solid model.

4.1.3. Simulation of the virtual shoulder arthroplasties

The shoulder arthroplasties were virtually simulated in Solidworks®. This section describes the steps followed to replace the humeral head by the 5 stemless implants modelled.

4.1.3.1. Eclipse implantation

The steps followed to replace the humeral head by the modelled implant were based on the surgical technique guide (Arthrex, 2018). A few key steps of the surgical procedure are described next and illustrated in Figure 4-18. Initially, the humeral head should be resected at the level of the anatomical neck. The trunion is placed over the cut surface, its underside surface fully contacting the bone, and the cage screw is centrally inserted perpendicular to the resected surface. Last, the humeral head is impacted over the trunion.

(a) (b) (c) (d)

Figure 4-18 – Surgical procedure of ECLIPSE™ Stemless Shoulder Prosthesis implantation (Adapted from Arthrex, 2018): (a) Resection of humeral head, (b) preparation of the hole, for the colocation of the cage screw, (c) trunion implantation and cage screw colocation, and (d) humeral head impaction.

The insertion of the Eclipse model into the intact bone model was performed in Solidworks®. Accordingly, a plane at the level of the anatomical neck was created corresponding to the resection plane. The humeral head was resected using the Solidworks® cutting tools, and the trunion was placed at the resected surface. After its placement, the cage screw and the humeral head were accurately positioned over the trunion, obtaining the result illustrated in Figure 4-19. To finish, the Solidworks® model was imported to Abaqus®.

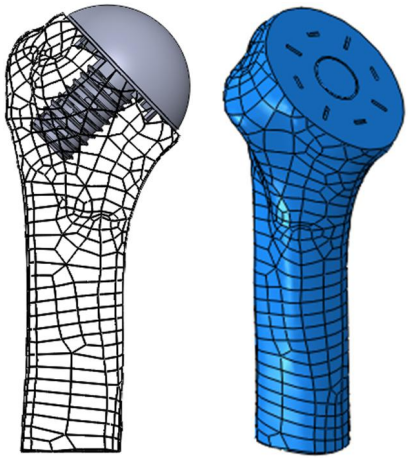

(a) (b)

Figure 4-19 – Illustration of the implanted model: (a) Anterior view of the Solidworks® model after the Eclipse implantation, and (b) final Abaqus® model without the Eclipse implant.

4.1.3.2. Global Icon implantation

The steps followed to replace the humeral head by the modelled implant were based on the surgical technique guide (DePuy Synthes, 2017b). A few key steps of the surgical procedure are described next and illustrated in Figure 4-20. First, the humeral head should be resected at the level of the anatomical neck. Then, the metaphysis is prepared, and the anchor plate is impacted until its underside surface fully contacts the bone. Last, the humeral head is impacted over the anchor plate.

(a) (b) (c) (d)

Figure 4-20 – Surgical procedure of GLOBAL ICON™ Stemless Shoulder System implantation (Adapted from DePuy Synthes, 2017b): (a) Guided humeral head resection, (b) preparation of the metaphysis prior to anchor plate implantation, (c) anchor plate implantation, and (d) humeral head implantation.

The insertion of the Global Icon model into the intact bone model was performed in Solidworks®. Accordingly, a plane at the level of the anatomical neck was created corresponding to the resection plane. Then, the humeral head was resected using the Solidworks® cutting tools, and the anchor plate was placed at the resected surface. Last, the humeral head was accurately positioned over the anchor plate obtaining the result illustrated in Figure 4-21. To conclude, the Solidworks® model was imported to Abaqus®.

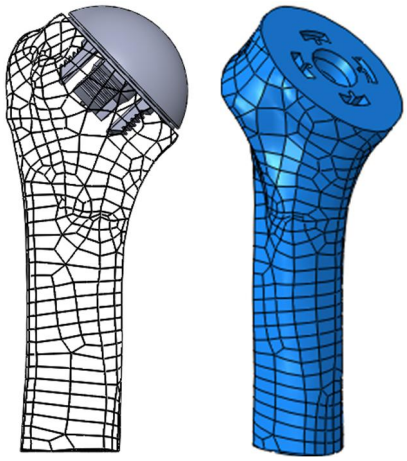

(a) (b)

Figure 4-21 – Illustration of the implanted model: (a) Anterior view of the Solidworks® model after the Global Icon implantation, and (b) final Abaqus® model without the Global Icon implant.

4.1.3.3. SMR implantation

The steps followed to replace the humeral head by the modelled implant were based on the surgical technique guide (Lima Corporate, 2016d). A few key steps of the surgical procedure are described next and illustrated in Figure 4-22. First, the humeral head should be resected at the level of the anatomical neck. Then, the metaphysis is prepared, and the core is inserted. The alignment of the core's fins has special indications: the curved fins of the implant must be placed according to the greater tuberosity. Additionally, the marks L (left) or R (right), corresponding to the shoulder side that is being operated, should be placed in a superolateral position. To conclude, the remaining components are positioned, and the humeral head is impacted until it sits flush on the osteotomy plane.

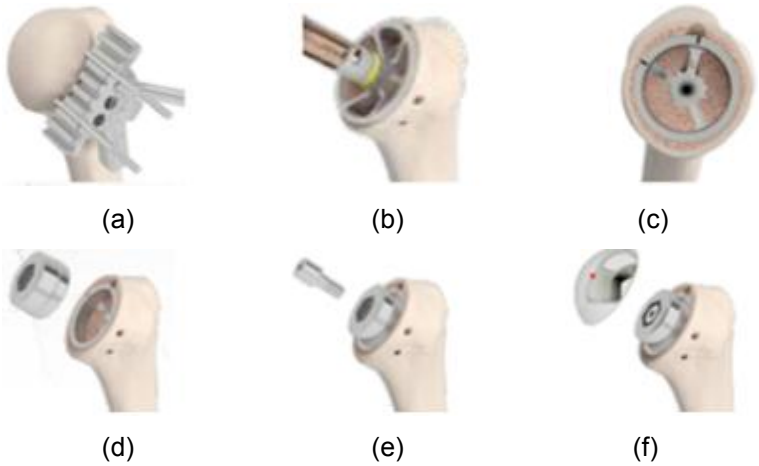

Figure 4-22 – Surgical procedure of SMR® Stemless (Adapted from Lima Corporate, 2016d): (a) Humeral head resection, (b) metaphysis reaming, (c) core implantation, (d) adaptor colocation, (e) connection of the adaptor to the core by the screw, and (f) humeral head impaction.

The insertion of the SMR model into the intact bone model was performed in Solidworks®. Accordingly, a plane at the level of the anatomical neck was created corresponding to the resection plane. Then, the humeral head was resected using the Solidworks® cutting tools and the core was placed at the metaphysis. Following its colocation, the adaptor and the screw were assembled with the core. The humeral head was accurately positioned over the humeral implant, obtaining the result illustrated in Figure 4-23. To conclude, the Solidworks® model was imported to Abaqus®.

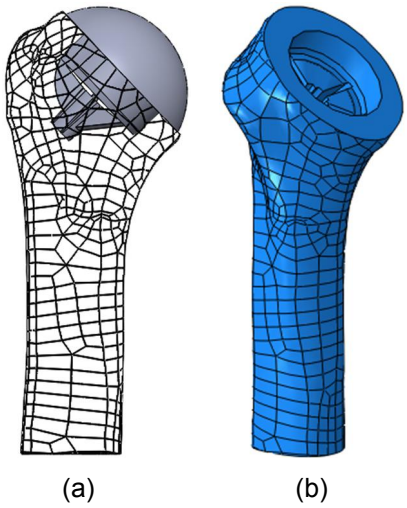

Figure 4-23 – Illustration of the implanted model: (a) Anterior view of the Solidworks® model after the SMR implantation, and (b) final Abaqus® model without the SMR implant.

4.1.3.4. Simpliciti implantation

The steps followed to replace the humeral head by the modelled implant were based on the surgical technique guide (Wright, 2016). A few key steps of the surgical procedure are described next and illustrated in Figure 4-24. First, the humeral head is resected at the level of the anatomical neck. Posteriorly, the metaphysis is prepared, and the nucleus is impacted, perpendicularly to the resected plane, until the collar is resting a few millimetres above the resected surface so that one fin points

directly superiolaterally. Last, the humeral head is impacted until the implant is flush against the humeral cut.

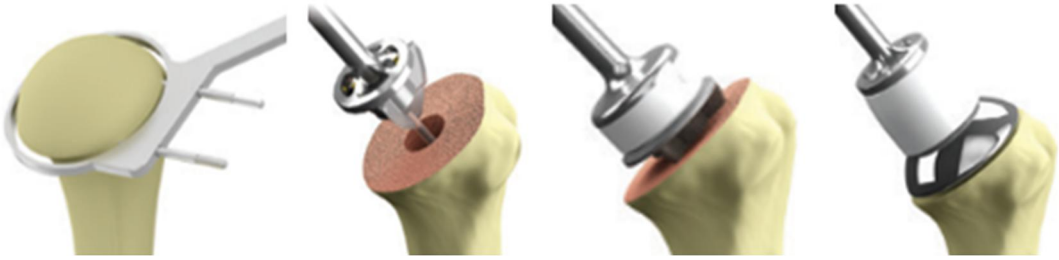

(a) (b) (c) (d)

Figure 4-24 - Surgical procedure of SIMPLICITI™ Shoulder System (Adapted from Wright, 2016): (a) Guided humeral head resection, (b) preparation of the metaphysis for colocation of the nucleus, (c) nucleus implantation, and (d) humeral head implantation.

The insertion of the Simpliciti model into the intact bone model was performed in the software Solidworks®. Initially, a plane at the level of the anatomical neck was created corresponding to the resection surface. The humeral head was resected using the Solidworks® cutting tools and the anchor plate was placed at the resected surface. After this placement, the humeral head was accurately positioned over the nucleus obtaining the result illustrated in Figure 4-25. Finally, the Solidworks® model was imported to Abaqus®.

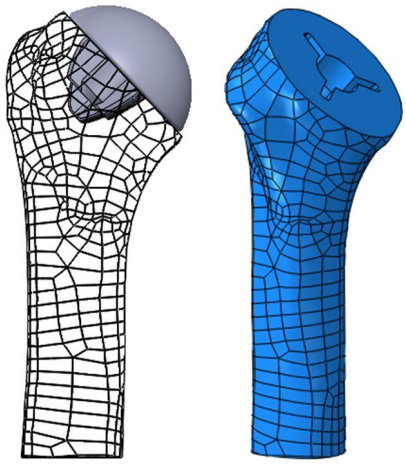

(a) (b)

Figure 4-25 – Illustration of the implanted model: (a) Anterior view of the Solidworks® model after the Simpliciti implantation, and (b) final Abaqus® model without the Simpliciti implant.

4.1.3.5. Sidus implantation

The steps followed to replace the humeral head by the modelled implant were based on the surgical technique guide (Zimmer, 2012). A few key steps of the surgical procedure are described next and illustrated in Figure 4-26. Initially, the humeral head should be resected exactly at the level of the anatomical neck. Then, the metaphysis is prepared, and the anchor is impacted until it sits flush with the countersunk area. To conclude, the humeral head implant is impacted over the anchor until it sits flush on the osteotomy plane.

(a) (b) (c) (d)

Figure 4-26 - Surgical procedure of Sidus™ Stem-Free Shoulder (Adapted from Zimmer, 2012b): (a) Humeral head resection, (b) metaphysis preparation, (c) anchor impaction, and (d) humeral head impaction.

The insertion of the Sidus model into the intact bone model was performed in Solidworks®. Initially, a plane at the level of the anatomical neck was created corresponding to the resection plane. Then, the humeral head was resected using the Solidworks® cutting tools and the anchor was positioned at the resected plane. Next, the humeral head was accurately placed over the anchor to obtain the result illustrated in Figure 4-27. To conclude, the Solidworks® model was imported to Abaqus®.

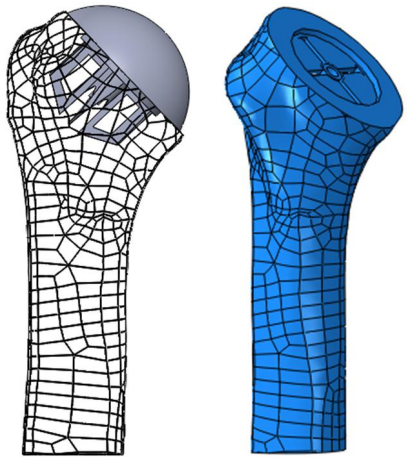

(a) (b)

Figure 4-27 – Illustration of the implanted model: (a) Anterior view of the Solidworks® model after the Sidus implantation, and (b) final Abaqus® model without the Sidus implant.

4.2. Finite element model

This section presents a description about the finite element (FE) modelling conditions considered. The finite element method (FEM) software used was Abaqus®. Henceforth, the bone subjected to a virtual shoulder arthroplasty will be referred to as implanted bone.

4.2.1. Physical properties

Bone was modelled as a linear elastic material with an orthotropic microstructure. Its material properties are obtained through the homogenization method briefly described in Section 3.1 considering a Young's modulus of 17.5 GPa and a Poisson's ratio of 0.3 for dense cortical bone (Gupta & Dan, 2004; Quental et al., 2012b). All implants are composed of 2 metal alloys, a titanium alloy ($TiAl_6V_4$) and a cobalt-chromium alloy (CoCrMo). The implants were modelled as linear elastic,

homogeneous and isotropic materials. A detailed description of the material properties considered for each component of the 5 stemless implants modelled is provided in Table 4-6.

The interactions between bone and the coated or blasted regions of the different components of the implants were modelled considering an ideal condition, for which full osseointegration occurred, and a worst-case condition, for which no osseointegration occurred. Regarding the Eclipse model, the trunion undersurface is coated with titanium plasma spray (TPS) and calcium phosphate (Arthrex, 2018). In the Global Icon model both anchor plate's undersurface and legs are coated with hydroxyapatite and have a grooved macrostructure (DePuy Synthes, 2017a). The SMR's core component is made of trabecular titanium which provides significant osseointegration with significantly high bone ingrowth percentages (Lima Corporate, 2016a). A significant part of the Simpliciti's nucleus has a highly porous coating, sintered titanium beads, conceding bone ingrowth (Tornier, 2014; Wright, 2017). In the Sidus model, the undersurface and fins of the anchor are rough stimulating long lasting osseointegration (Zimmer, 2012).

Table 4-6 – Material Properties (Quental et al., 2012b).

Model	**Component**	**Material**	**Young's modulus (E, GPa)**	**Poisson's ration (ν)**
Eclipse	Humeral Head	Cobalt-Chromium alloy	230	0.3
	Cage Screw	Titanium alloy	115	0.3
	Trunion	Titanium alloy	115	0.3
Global Icon	Humeral Head	Cobalt-Chromium alloy	230	0.3
	Anchor Plate	Titanium alloy	115	0.3
SMR	Humeral Head	Cobalt-Chromium alloy	230	0.3
	Core	Titanium alloy	115	0.3
	Adaptor	Titanium alloy	115	0.3
	Screw	Titanium alloy	115	0.3
Simpliciti	Humeral Head	Cobalt-Chromium alloy	230	0.3
	Nucleus	Titanium alloy	115	0.3
Sidus	Humeral Head	Cobalt-Chromium alloy	230	0.3
	Humeral Anchor	Titanium alloy	115	0.3

The use of rough surfaces and calcium phosphate coatings enhances early osseointegration (Aebli et al., 2003). Consequently, for the ideal condition, interactions between bone and the coated or blasted surfaces, highlighted in green in Figure 4-28, were defined as bonded using a tie constraint (Dassault Systèmes, 2015). For the worst-case condition, a contact formulation was considered instead (Dassault Systèmes, 2015). The friction coefficients used are listed in Table 4-7. For the Global Icon and Sidus models, the friction coefficient was assumed to be 0.6 because no additional information was found regarding the type of rough titanium coating applied.

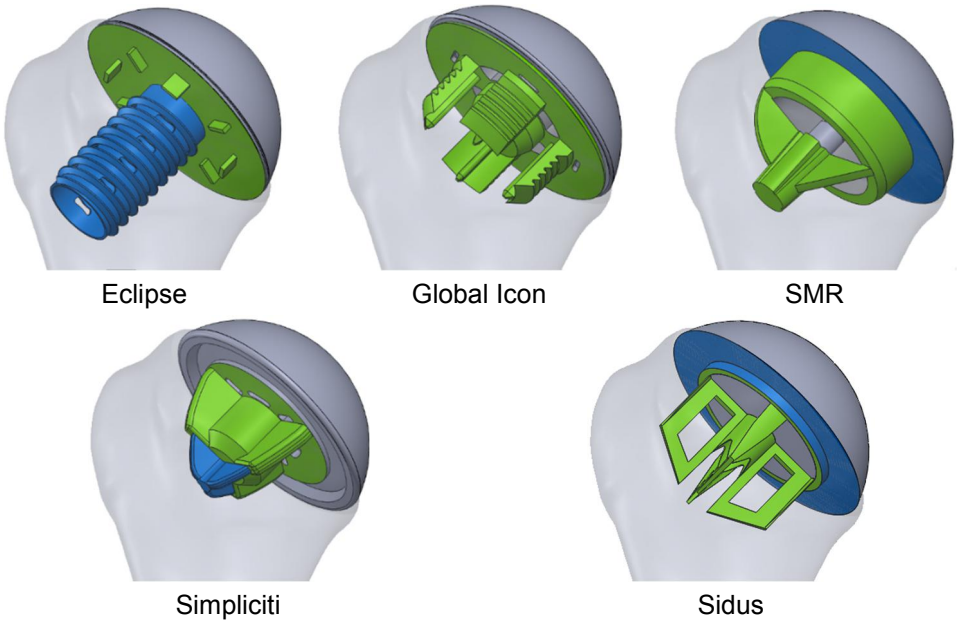

Figure 4-28 - Anterior view of the interactions between the bone and the implant for all 5 models. The surfaces highlighted in green and blue represent, respectively, a bonded contact (tie constraint) and a frictional contact (penalty formulation).

The interactions between the humeral head and the humeral implant, for all 5 models, were simulated as bonded with a tie constraint. In Eclipse model, the cage screw was simulated bonded to the trunion. Likewise, all the 3 components of the SMR humeral implant were bonded to each other with a tie constraint. Both undersurfaces of the SMR and Sidus humeral heads are in contact with the resection surface of the bone. Accordingly, these interactions were modelled as frictional contact with a penalty frictional formulation. The interactions between the Eclipse cage screw and bone, the Simpliciti nucleus' bottom and bone, the undersurface of the Eclipse humeral head and the upper surface of the trunion (Magosch et al., 2012), and the upper lateral surface of the Sidus' anchor and bone were also simulated using a contact formulation. All contact interactions are highlighted in blue in Figure 4-28.

Table 4-7 – Friction coefficients applied for the different interactions considered in the finite element models developed.

Materials	**Coefficients of Friction**
Bone - TPS	0.6 (Grant et al., 2007)
Bone – Trabecular Titanium	2.2 (Lima Corporate, 2016a)
Bone - Sintered Titanium Beads	0.53 (Rancourt & Drouin, 1990)
Bone – Chromium-Cobalt	0.26 (Sobocinski, 2015)
Bone - Titanium	0.36 (Eberle & Augat, 2007)
Titanium - Chromium-Cobalt	0.3 (Swaminathan & Gilbert, 2012)

4.2.2. Loading and boundary conditions

On one hand, the loading conditions should be comprehensive to mimic in vivo loading but, on the other hand, they must be feasible from the computational point of view. In this study, 6 load cases, related to 10º, 60º and 90º positions of abduction in the coronal plane and anterior flexion in the sagittal plane,

were considered (Santos et al., 2018). Each load case includes the glenohumeral reaction force and the action of 11 muscles. The muscles considered are the Pectoralis Major, Latissimus Dorsi, Deltoid, Supraspinatus, Infraspinatus, Subscapularis, Teres Minor, Teres Major, Coracobrachialis, Triceps brachii and Biceps brachii. For more details about these muscles, see Section 2.3.3.

The load applied to the humerus was estimated by an inverse dynamic analysis of a multibody musculoskeletal model of the upper limb composed of 7 rigid bodies, 6 anatomical joints, and 21 muscles (Quental et al., 2012a). Although the humerus studied here and that from Quental et al. (2012a), are based on the same subject, the global coordinate systems considered are different. Therefore, a transformation of coordinates had to be applied to transform the forces, and their application points, from the coordinate system of Quental et al. (2012a) to that of the finite element model. Having had access to the 3-D geometric model of Quental et al. (2012a), a Matlab® routine was developed to identify the rotation matrix that transforms one reference frame to the other.

Besides the origins and insertions of the muscles, the wrapping of the muscles over the humerus was also considered. Note that only muscles with a resultant force higher than 1 N were considered. The muscle forces were applied on attachment points (Dassault Systèmes, 2015) whose coordinates were provided by the multibody system model applied. Coupling constraints were defined to transfer the force from the attachment points to the corresponding nodes on the bone surface (Dassault Systèmes, 2015). The muscle attachment sites, illustrated in Figure 4-29, were defined as the nodes on the bone surface contained within a sphere centred on each attachment point. The muscle forces related to the wrapping of muscles over the humerus were coupled to the nodes on the surface of the humerus that were contained within a sphere centred on the point closest to the projection of the force onto the humerus. All these procedures were implemented in a Matlab® routine.

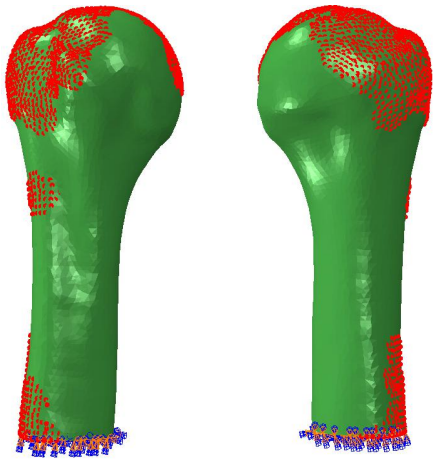

(a) (b)

Figure 4-29 – Anterior (a) and posterior (b) view of the intact model. The nodes in red represent the regions where load is applied. It includes all the regions correspondent to action of the 11 muscles, as well as the glenohumeral joint reaction force, for all the load cases. It is also represented the encastre condition in the lower extremity of the model.

The application of the glenohumeral joint reaction force followed a procedure similar to that adopted for the muscle wrapping forces. For the sake of briefness, detailed data regarding the muscle and joint

reaction forces, i.e., directions and applications points, are not presented here due to the great amount of data.

The coupling constraints were defined using uniform and quadratic weighting methods, for muscle and glenohumeral joint forces, respectively. In the uniform weighting method the force is distributed equally through all nodes, whereas in the quadratic weighting method the force in each node decreases with the square radial distance to the attachment point (Dassault Systèmes, 2015).

To prevent rigid body motion, the humerus was fixed at its lower extremity with an encastre condition, restricting all displacements and rotations (Dassault Systèmes, 2015) as shown in Figure 4-29.

4.2.3. Mesh generation

Tetrahedral and hexahedral elements are commonly used in 3-D problems. When it comes to a complex 3-D geometry, the use of tetrahedral elements is frequently preferable because a general 3-D domain cannot always be decomposed into an assembly of hexahedral elements (Cifuentes & Kalbag, 1992). Due to the complexity of the structures being modelled, linear tetrahedral (C3D4) elements were used to define the finite element meshes of the intact bone, the implanted bone, and all the implants.

To choose a proper element size, a convergence analysis was performed. Since the humeral head is the region of most interest in this study, 2 points were selected in this region, identified as Ref1 and Ref2 in Figure 4-30. For each point, the Von Mises stress was evaluated per element size, as well as the time taken to complete each simulation. For the optimal mesh, an average element edge of 1.8 mm was selected.

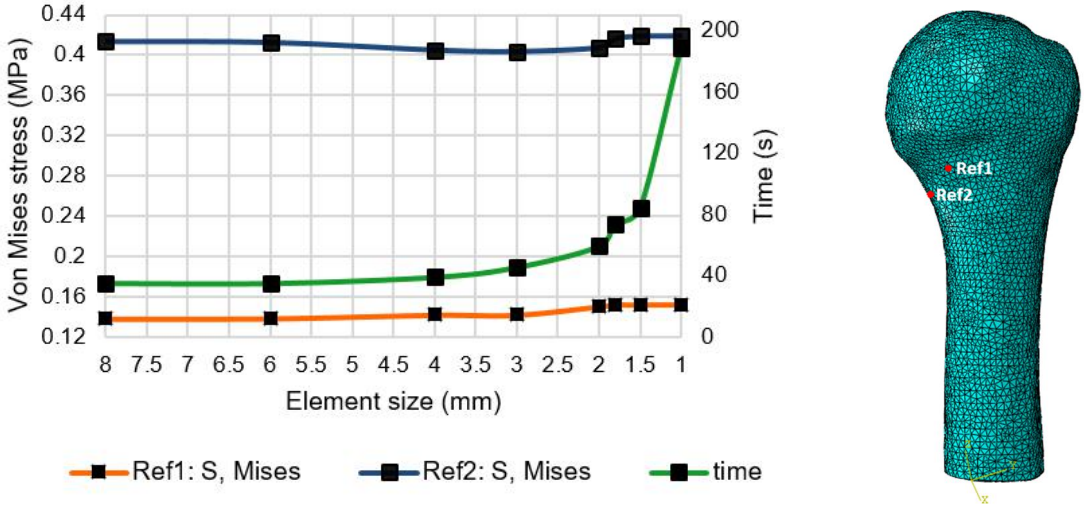

Figure 4-30 – Mesh convergence analysis to select the appropriate mesh for the intact bone. For each element size, the Von Mises stress and time were analysed. In the posterior view of intact bone, are shown the selected points, Ref1 and Ref2.

Concerning the implants, all models were defined with an average element size of 1.8 mm. Figure 4-31 presents an overview of the finite element meshes.

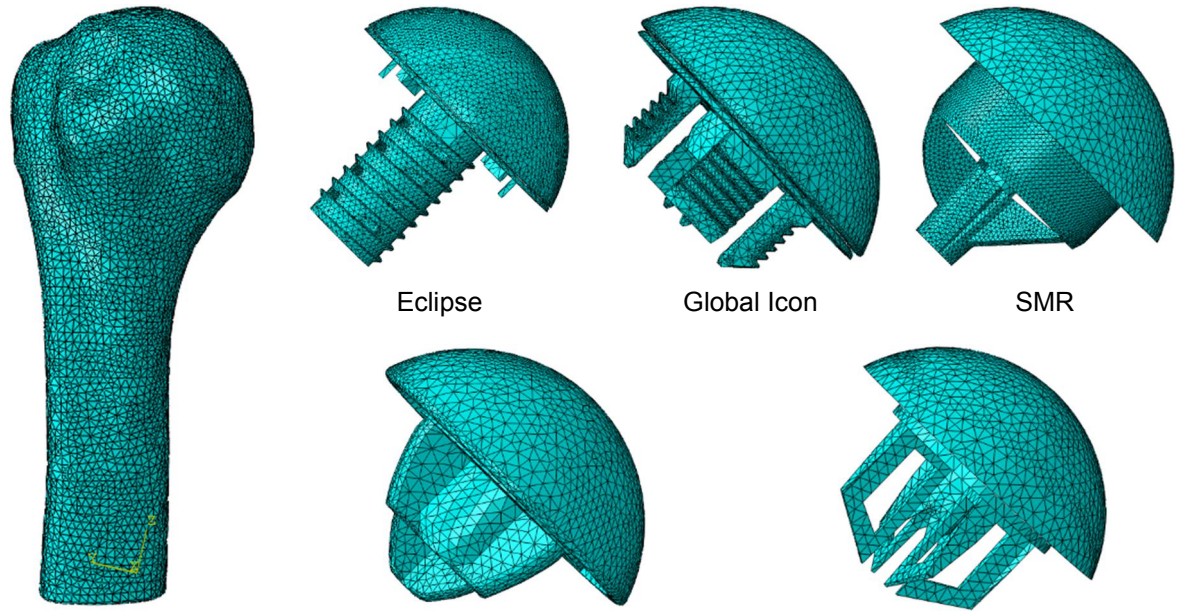

Figure 4-31 – Anterior view of the finite element meshes for the intact bone and all 5 implant models.

Nevertheless, due to changes in geometry following the insertion of the implant, some FE meshes required further adjustments. These adjustments, listed in Table 4-8, consisted mainly in refining a local part by changing locally the average element size. Additionally, a coarser mesh was defined at the humerus' diaphysis of 2 models to reduce the computational cost.

4.3. Bone remodelling simulations

The settings and conditions of the bone remodelling simulations are explained in this section. The load weight factors α^P, described in Equation (3-3), were calculated according to the relative frequencies of arm movements during daily activities. For the arm elevation angles of 10°, 60° and 90°, the weight factors are 0.251371, 0.055667 and 0.011659 for abduction, and 0.537375, 0.119003 and 0.024924 for flexion, respectively (Coley et al., 2008, 2009). A node-based approach (Jacobs et al., 1995) and a step length s of 20 were followed for the bone remodelling simulations.

4.3.1. Validation of the bone remodelling model for the intact bone

Before applying the bone remodelling model to the 5 bone-implant assemblies, simulations of the intact bone model were performed to validate the application of the bone remodelling model. The goal was to assess if the model could successfully reproduce the actual bone density distribution of the humerus under analysis. For that purpose, different simulations were performed considering 8 values for the parameter k, ranging from 1×10^{-5} to 3.5×10^{-4}, and 5 values for the parameter m ranging from 1 to 5. For the sake of comparison, all simulations were run for 200 iterations.

Table 4-8 – Description of mesh refinements of the different components of the finite element models developed. The symbol × means that no local refinement was performed.

Model		Global element size (mm)	Local element size (mm)	Nodes	Elements
Intact Bone		1.8	×	31578	166782
Eclipse	Implanted Bone	1.8	3 (on humerus' diaphysis) 1.2 (on the surface of interaction with cage screw)	50195	275852
	Humeral Head	1.8	×	12546	62908
	Trunion	1.8	×	1974	5587
	Cage Screw	1.8	1.2 (on all its superficial surface)	7465	23770
Global Icon	Implanted Bone	1.8	×	56344	309868
	Humeral Head	1.8	×	6919	33090
	Anchor Plate	1.8	×	10069	38175
SMR	Implanted Bone	1.8	0.8 (on the surface of interaction with core)	54447	293362
	Humeral Head	1.8	×	5503	27802
	Core	1.8	0.8 (on all its superficial surface)	9631	42730
	Adaptor and Screw	1.8	×	1530	6502
Simpliciti	Implanted Bone	1.8	2.5 (on humerus' diaphysis) 1.5 (on the surface of interaction with nucleus)	34709	186610
	Humeral Head	1.8	×	6625	32775
	Nucleus	1.8	1.5 (on its lower superficial surface)	3555	13358
Sidus	Implanted Bone	1.8	×	32016	164272
	Humeral Head	1.8	×	5636	28221
	Anchor	1.8	×	1830	5836

The actual bone density distribution of the humerus was mapped from the CT scan images used to create the 3-D geometry of the bone. The different attenuation values μ of tissues, typically represented as gray values, confer contrast to CT scan images. Therefore, each pixel of the CT scan image has a numerical value assigned to it, known as CT-value, which is calculated by comparison with the attenuation value of water, μ_{water} as:

$$\mathrm{CT-value} = \frac{\mu - \mu_{water}}{\mu_{water}} \times 1000 \tag{4-2}$$

The unit of CT-values is Hounsfield unit, HU (Buzug, 2008). Using bonemapy (version 0.4.1, 2013), an Abaqus® freeware plug-in (Hogg, 2013), the CT-values were automatically assigned to each node

of the FE mesh of the intact bone. According to Gupta & Dan (2004), the apparent bone density ρ can be computed from the CT-values using a linear calibration derived from 2 reference points of the CT scan images. For the case of moist bone (with marrow in situ), the first point in the linear relationship should be the CT-value of water, $\rho = 0$ g cm^{-3}, corresponding to the non-bone condition, while the second point should be the CT-value of cortical bone, $\rho = 1.8$ g cm^{-3}. The equation of the linear calibration is:

$$\rho = \mathrm{a} + \mathrm{b} \times \text{CT-value} \tag{4-3}$$

where the parameters a and b are obtained through the calibration. Considering the cortical bone apparent density, 1.8 g cm^{-3} (Gupta & Dan, 2004), as the maximum bone apparent density, the relative bone density ρ_r can be computed through the following expression:

$$\rho(\text{g cm}^{-3}) = 1.8\,\rho_r \tag{4-4}$$

The Equations (4-3) and (4-4) were implemented in a Matlab® routine to compute the initial relative density for each FE mesh node of the intact bone model. As expected, the obtained density distribution presented higher densities in the superficial nodes, whilst the inner nodes presented lower densities, corresponding to cortical and trabecular bone, respectively. However, the abrupt change in densities on the external boundary of the bone led to the appearance of superficial nodes with lower densities, an effect known as partial volume effect (Taddei et al., 2004). This phenomenon occurs when, within a voxel, there are tissues with different densities, leading to an averaging of the different densities (Peters & Maret, 2013). To correct this phenomenon, the density of all superficial nodes was altered so that the intact bone model could have a uniform cortical bone layer. The maximum density present in the obtained density distribution was considered for the cortical layer.

To start the simulations from a more realistic condition, the bone density distribution estimated from the CT scan images was considered as initial condition. For the sake of simplicity, henceforth, the apparent density will be just referred as density.

4.3.2. Bone remodelling of the humerus after the virtual shoulder arthroplasty

The main goal of this study is to evaluate the changes in the bone adaptation process of the humerus after a shoulder arthroplasty under a healthy condition. Notice that events responsible for abnormally unbalancing the bone adaptation process, such as osteoporosis, are not considered here, and thus the assumption of a healthy condition. The bone remodelling simulations for the implanted models were performed considering the parameters k and m selected in the validation step, which were deemed as the best to reproduce the actual bone density distribution of the bone under analysis. As explained in Section 4.2.1., the simulations were performed for a fully osseointegration condition and a fully absent osseointegration condition. To analyse the sensitivity of the results to the parameter k, additional

simulations were performed considering parameters k 50 % larger and 50 % smaller than that deemed as best. The parameter m remained constant in this sensitivity analysis.

All simulations were performed for 200 iterations. The initial condition was defined as the bone density distribution obtained for the intact bone model, after 200 iterations using the set of parameters selected as best. Because after implantation the meshes of the intact and implanted bones are different, a Matlab® routine was developed to map the material properties from the intact bone to the implanted bone. For each node of the implanted model, the routine computes a weighted average density based on the distance of the nearest nodes of the intact model.

4.4. Analysis of the results

4.4.1. Validation of the bone remodelling model for the intact bone

Qualitative and quantitative analyses were performed to assess which set of bone remodelling model parameters best reproduced the actual bone density distribution of the humerus being studied. On one hand, the results were visually compared with the CT scan images and, on the other hand, a statistical analysis was performed to compare the predicted bone densities with those from the CT scan images. The root-mean-square error (RMSE) based on relative and absolute differences of bone density, $\Delta\rho_r$ and $\Delta\rho_a$, respectively, was computed (Quental et al., 2014b). The differences $\Delta\rho_r$ and $\Delta\rho_a$ are expressed as:

$$\Delta\rho_r = \frac{\rho_i^{BR} - \rho_i^{CT}}{\rho_i^{CT}} \tag{4-5}$$

$$\Delta\rho_a(\text{g cm}^{-3}) = \rho_i^{BR} - \rho_i^{CT} \tag{4-6}$$

where ρ_i^{BR} and ρ_i^{CT} are the densities of node i from the bone remodelling simulations and the CT scan images, respectively. Notice that the RMSE computed here weighed each node i by its volume V_i, i.e.:

$$\text{RMSE} = \sqrt{\frac{\sum_{i=1}^{n}(\Delta\rho_i \times V_i)^2}{\sum_{i=1}^{n} V_i}} \tag{4-7}$$

where n denotes the total number of nodes to be evaluated and $\Delta\rho_i$ is the density difference for each node i. The unit of the RMSE is not mentioned because it depends of the density difference used, the unit of the volume is cm^3. The mean and standard deviation (SD) of the bone density distribution were also computed for each simulation, and a mean error (ME) expressed as:

$$\text{ME}(\%) = \frac{\bar{x}_{BR} - \bar{x}_{CT}}{\bar{x}_{CT}} \times 100 \tag{4-8}$$

was computed between the simulations and the CT scan images. The variables $\bar{x}_{BR}$ and $\bar{x}_{CT}$ are the mean density of the humeral head at the end of the bone remodelling simulation and in the CT scan images, respectively. The nodes evaluated belong to a region that excludes the superficial nodes as they were artificially changed, as well as the nodes below the surgical neck since the humeral head is the major region of interest given the implants' geometry.

4.4.2. Bone remodelling of the humerus after the virtual shoulder arthroplasty

To remove possible numerical factors from the analysis of the results, the bone remodelling simulations after a shoulder arthroplasty were compared to the bone density distribution of the intact bone obtained for 400 iterations. Notice that the implanted models were run for 200 iterations, starting from the density distribution of the intact bone obtained after 200 iterations. Figure 4-32 illustrates, and summarizes, the methodology adopted.

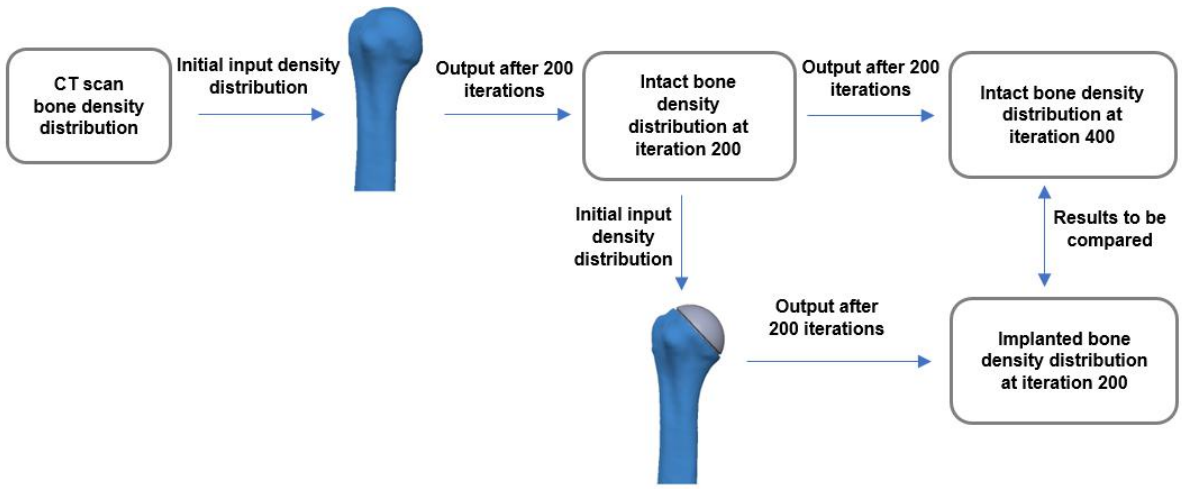

Figure 4-32 – Illustration of the bone material properties during the bone remodelling simulations.

For a qualitative analysis, the changes in bone density were evaluated through visual comparison. For a quantitative analysis, the change in bone mass was computed for 8 proximal regions of the humerus, defined based on Reeves et al. (2017). The bone is divided into anterior, posterior, medial and lateral sections, and each of these sections is divided into superficial and deep sections by a transversal plane. Figure 4-33 presents a scheme of the regions of interest (ROI) described.

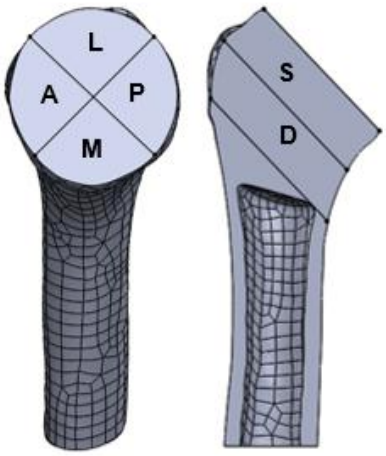

(a) (b)

Figure 4-33 – Regions of interest of the humerus: (a) A, L, P, and M represent, respectively, anterior, lateral, posterior and medial. (b) Anterior view of longitudinal cut of the humerus, in which S and D represent superficial and deep.

The change in bone mass is mathematically expressed as:

$$\Delta bm(\%) = \frac{\sum_{i=1}^{n}(\rho_i^{200WI} - \rho_i^{400WOI}) \times V_i}{\sum_{i=1}^{n} \rho_i^{200WOI} \times V_i} \times 100 \quad (4\text{-}9)$$

where n is the total number of nodes within the ROI under analysis, V_i is the volume associated to each node i, ρ_i^{200WI} is the density of node i $(i \in R\,O\,I)$ for the implanted model at the end of the bone remodelling simulation , and ρ_i^{200WOI} and ρ_i^{400WOI} are the densities of node i $(i \in R\,O\,I)$ for the intact bone model at the iterations 200 and 400, respectively.

For a better understanding about the effect of the implants on the overall change in bone mass, an additional analysis was performed. For each implant, the mass of the humeral head before the arthroplasty, defined as the stage 0^-, the mass of the humeral head immediately after the virtual arthroplasty, the stage 0^+, and the mass of the humeral head at the end of the bone remodelling simulation, the stage 1, were computed. The bone mass is expressed as:

$$mass(\mathrm{g}) = \sum_{i=1}^{n} \rho_i \times V_i \quad (4\text{-}10)$$

where n is the total number of nodes within the humeral head, ρ_i is the bone density of node i, and V_i is the volume associated to each node i. Notice that the Equation (4-10) is only applied to the stages 0^- and 0^+. For the stage 1, the bone mass is computed considering the change in bone mass Δbm instead. This allows to remove possible numerical factors from the results, as the bone remodelling simulations after a shoulder arthroplasty were compared to the bone density distribution of the intact bone obtained for 400 iterations. The mass $mass_1$, at stage 1, is expressed as:

$$mass_1(\mathrm{g}) = mass_{0^+}\left(1 + \frac{\Delta bm(\%)}{100\ \%}\right) \quad (4\text{-}11)$$

where $mass_{0^+}$ is the mass at stage 0^+.

Finally, the overall change in bone mass Δbm_O after the surgical procedure with respect to the stage 0^-, corresponding to the amount of mass removed by each implant during the surgical procedure, was computed by:

$$\Delta bm_O(\%) = \frac{mass_{0^+} - mass_{0^-}}{mass_{0^-}} \times 100 \quad (4\text{-}12)$$

where $mass_{0^+}$ and $mass_{0^-}$ are the mass at stages 0^+ and 0^-, respectively. The overall change in bone mass Δbm_O at the end of the bone remodelling simulation with respect to the stage 0^- is computed by:

$$\Delta bm_O(\%) = \frac{mass_1 - mass_{0^-}}{mass_{0^-}} \times 100 \quad (4\text{-}13)$$

where $mass_1$ and $mass_{0^-}$ are the mass at stages 1 and 0^-, respectively.

Through the evaluation of the overall change in bone mass before and after the shoulder arthroplasty, it is possible to assess how much mass an implant removes from the humeral head, and to what extent the mass changes during the bone adaption process. The region analysed was limited to the proximal end of the humerus, above the surgical neck.

5. Results

This chapter presents the results obtained regarding the validation of the bone remodelling model and the adaptation of the humerus due to the insertion of the 5 stemless implants modelled.

5.1. Validation of the bone remodelling model for the intact bone

Bone remodelling simulations were performed for 200 iterations ensuring that the average change in bone density between consecutive iterations was below 1×10^{-3} g cm^{-3} at the end of each simulation. The bone density distribution estimated from the CT scan images considered as initial condition ranged between 0.071402 g cm^{-3} and 1.8 g cm^{-3}. The evaluated values were 1×10^{-5}, 5×10^{-5}, 1×10^{-4}, 1.5×10^{-4}, 2×10^{-4}, 2.5×10^{-4}, 3×10^{-4} and 3.5×10^{-4} for the parameter k, and 1, 2, 3, 4 and 5 for the parameter m. The RMSE for the absolute and relative differences of bone density are illustrated in Figure 5-1. For a more detailed analysis, the RMSE, mean, SD, and ME between the densities of the bone remodelling simulations and the CT scan images computed for each simulation are presented in Table 5-1. For the sake of comparison, the RMSEs were normalized by the maximum RMSE value obtained for each difference, so that it is dimensionless and, at most, unitary.

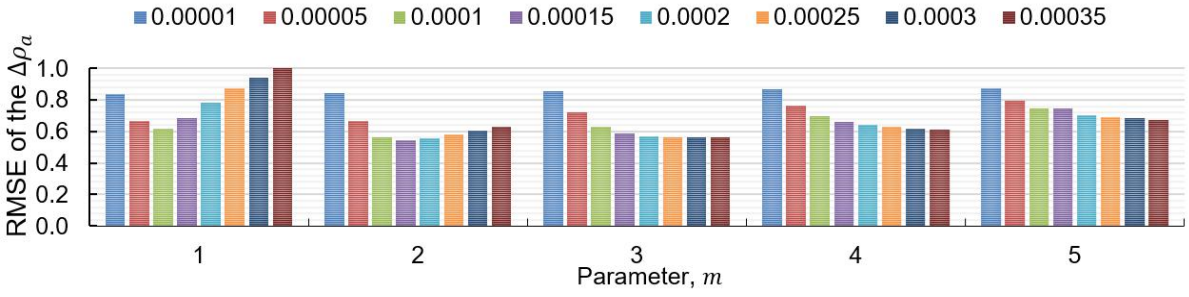

(a)

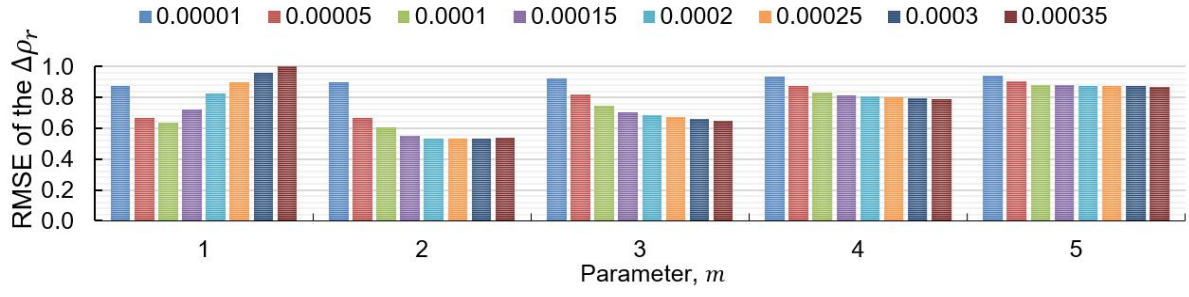

(b)

Figure 5-1 – Normalized RMSEs, based on the absolute difference $\Delta\rho_a$ (a) and relative difference $\Delta\rho_r$ (b), between the density of the bone remodelling simulations and the CT scan images for each set of parameters k and m evaluated. The RMSEs presented for $\Delta\rho_a$ and $\Delta\rho_r$ are normalized by the maximum RMSE value obtained for each difference, i.e., 0.0247 g cm$^{-\frac{3}{2}}$ and 0.0507 cm$^{\frac{3}{2}}$, respectively.

Table 5-1 – Normalized RMSEs based on $\Delta\rho_a$ and $\Delta\rho_r$ between the density of the bone remodelling simulations and the CT scan images, mean and SD of the performed bone remodelling simulations, and the error between the mean of the bone density distribution, for each simulation, with the mean of actual bone density distribution. The RMSEs presented for $\Delta\rho_a$ and $\Delta\rho_r$ are normalized by the maximum RMSE value obtained for each difference, i.e., 0.0247 g cm$^{-\frac{3}{2}}$ and 0.0507 cm$^{\frac{3}{2}}$, respectively.

m	k	RMSE		Mean (SD) [g cm^{-3}]	ME (%)
		$\Delta\rho_a$	$\Delta\rho_r$		
1	1×10^{-5}	0.8374	0.8749	0.7582 (0.3681)	46.32
	5×10^{-5}	0.6641	0.6665	0.6356 (0.3686)	22.67
	1×10^{-4}	0.6167	0.6367	0.5106 (0.3609)	1.45
	1.5×10^{-4}	0.6857	0.7248	0.4154 (0.3490)	19.83
	2×10^{-4}	0.7827	0.8227	0.3442 (0.3360)	33.57
	2.5×10^{-4}	0.8717	0.9015	0.2911 (0.3233)	43.82
	3×10^{-4}	0.9437	0.9588	0.2516 (0.3111)	51.44
	3.5×10^{-4}	1.0000	1.0000	0.2219 (0.3000)	57.17
2	1×10^{-5}	0.8426	0.9009	0.7643 (0.3568)	47.51
	5×10^{-5}	0.6641	0.6665	0.6356 (0.3686)	22.67
	1×10^{-4}	0.5643	0.6062	0.5766 (0.2835)	11.28
	1.5×10^{-4}	0.5421	0.5512	0.5118 (0.2568)	1.23
	2×10^{-4}	0.5567	0.5330	0.4655 (0.2375)	10.17
	2.5×10^{-4}	0.5821	0.5313	0.4313 (0.2233)	16.77
	3×10^{-4}	0.6081	0.5355	0.4051 (0.2126)	21.82
	3.5×10^{-4}	0.6318	0.5414	0.3842 (0.2041)	25.85
3	1×10^{-5}	0.8553	0.9221	0.7714 (0.3533)	48.86
	5×10^{-5}	0.7214	0.8191	0.7014 (0.3075)	35.35
	1×10^{-4}	0.6290	0.7439	0.6385 (0.2665)	23.21
	1.5×10^{-4}	0.5881	0.7058	0.5960 (0.2399)	15.01
	2×10^{-4}	0.5715	0.6851	0.5660 (0.2224)	9.24
	2.5×10^{-4}	0.5654	0.6717	0.5436 (0.2102)	4.91
	3×10^{-4}	0.5638	0.6610	0.5259 (0.2012)	1.48
	3.5×10^{-4}	0.5640	0.6512	0.5111 (0.1941)	1.37
4	1×10^{-5}	0.8657	0.9342	0.7763 (0.3534)	49.82
	5×10^{-5}	0.7656	0.8723	0.7245 (0.3092)	39.82
	1×10^{-4}	0.6966	0.8326	0.6806 (0.2715)	31.34
	1.5×10^{-4}	0.6619	0.8148	0.6522 (0.2478)	25.87
	2×10^{-4}	0.6423	0.8056	0.6324 (0.2320)	22.04
	2.5×10^{-4}	0.6295	0.7993	0.6173 (0.2207)	19.14
	3×10^{-4}	0.6197	0.7935	0.6050 (0.2120)	16.76
	3.5×10^{-4}	0.6118	0.7876	0.5944 (0.2049)	14.71
5	1×10^{-5}	0.8733	0.9412	0.7796 (0.3546)	50.46
	5×10^{-5}	0.7973	0.9024	0.7400 (0.3152)	42.80
	1×10^{-4}	0.7468	0.8823	0.7083 (0.2827)	36.70
	1.5×10^{-4}	0.7468	0.8823	0.7083 (0.2827)	36.70
	2×10^{-4}	0.7051	0.8746	0.6752 (0.2486)	30.31
	2.5×10^{-4}	0.6934	0.8735	0.6648 (0.2382)	28.30
	3×10^{-4}	0.6837	0.8721	0.6562 (0.2299)	26.63
	3.5×10^{-4}	0.6752	0.8700	0.6486 (0.2229)	25.17

The lowest RMSEs were obtained for a parameter k of 1.5×10^{-4} and a parameter m of 2 for the absolute difference of bone density, and a parameter k of 2.5×10^{-4} and a parameter m of 2, for the relative difference of bone density.

However, the solution characterized by the parameter k of 1.5×10^{-4} and the parameter m of 2 has the lowest mean error, meaning that its average density distribution in the humeral head is more similar to the actual bone density distribution than the solution of the parameter k of 2.5×10^{-4} and the parameter m of 2. Accordingly, the solution for the parameter k of 1.5×10^{-4} and the parameter m of 2 is deemed as the best to reproduce the actual bone density distribution of the humerus under analysis.

For a qualitative analysis of the results, Figure 5-2 compares the bone density distribution obtained computationally with that of the CT scan images. For the sake of briefness, only 3 slices are shown. Despite differences existing between the computational predictions and the CT scan images, the bone density distributions are generally comparable.

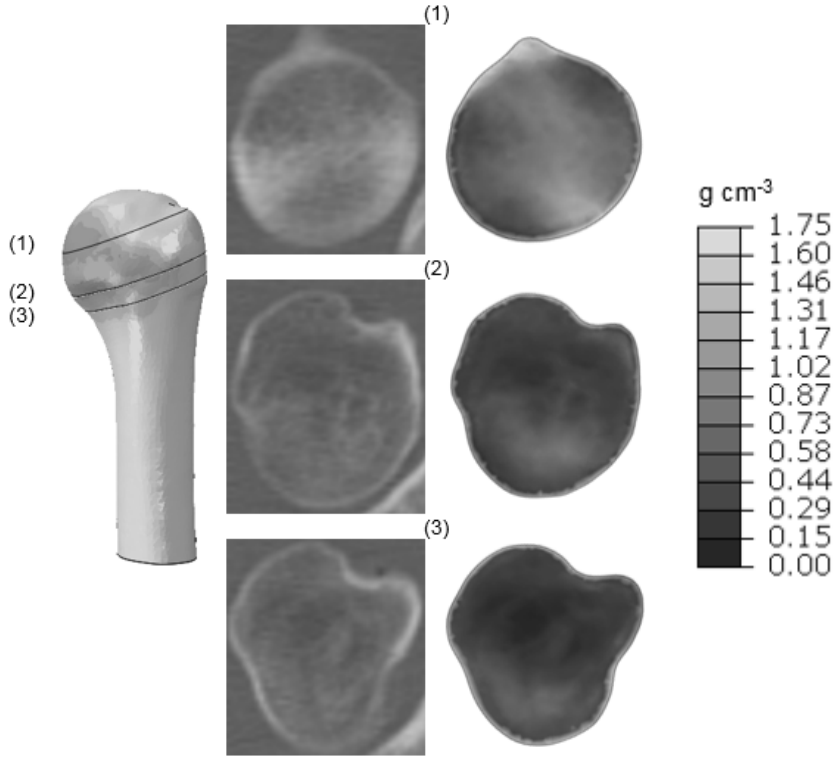

Figure 5-2 – Comparison between the CT scan images (a) and the bone remodelling result (bone density) (b) for the selected parameters k and m, 1.5×10^{-4} and 2, respectively.

5.2. Bone remodelling of the humerus after the virtual shoulder arthroplasty

Like before, bone remodelling simulations were performed for 200 iterations. The average change in bone density was always below 1×10^{-3} g cm^{-3} at the end of all simulations. Figure 5-3 presents the

absolute changes in bone density computed for each implanted bone with respect to the intact bone. For the sake of simplicity, negative changes in bone density were classified as bone resorption, while positive changes were classified as bone apposition. The equilibrium condition, depicted in green, is defined for an absolute change, $\Delta\rho$, in bone density below 0.1 g cm^{-3} (-0.1 g cm^{-3} $< \Delta\rho <$ 0.1 g cm^{-3}). Both bone resorption and bone apposition were divided into two levels. Bone resorption is depicted in red ($\Delta\rho < -0.2$ g cm^{-3}) and orange (-0.2 g cm^{-3} $\leq \Delta\rho \leq -0.1$ g cm^{-3}), whereas bone apposition is depicted in dark blue ($\Delta\rho >$ 0.2 g cm^{-3}) and light blue (0.1 g cm^{-3} $\leq \Delta\rho \leq$ 0.2 g cm^{-3}).

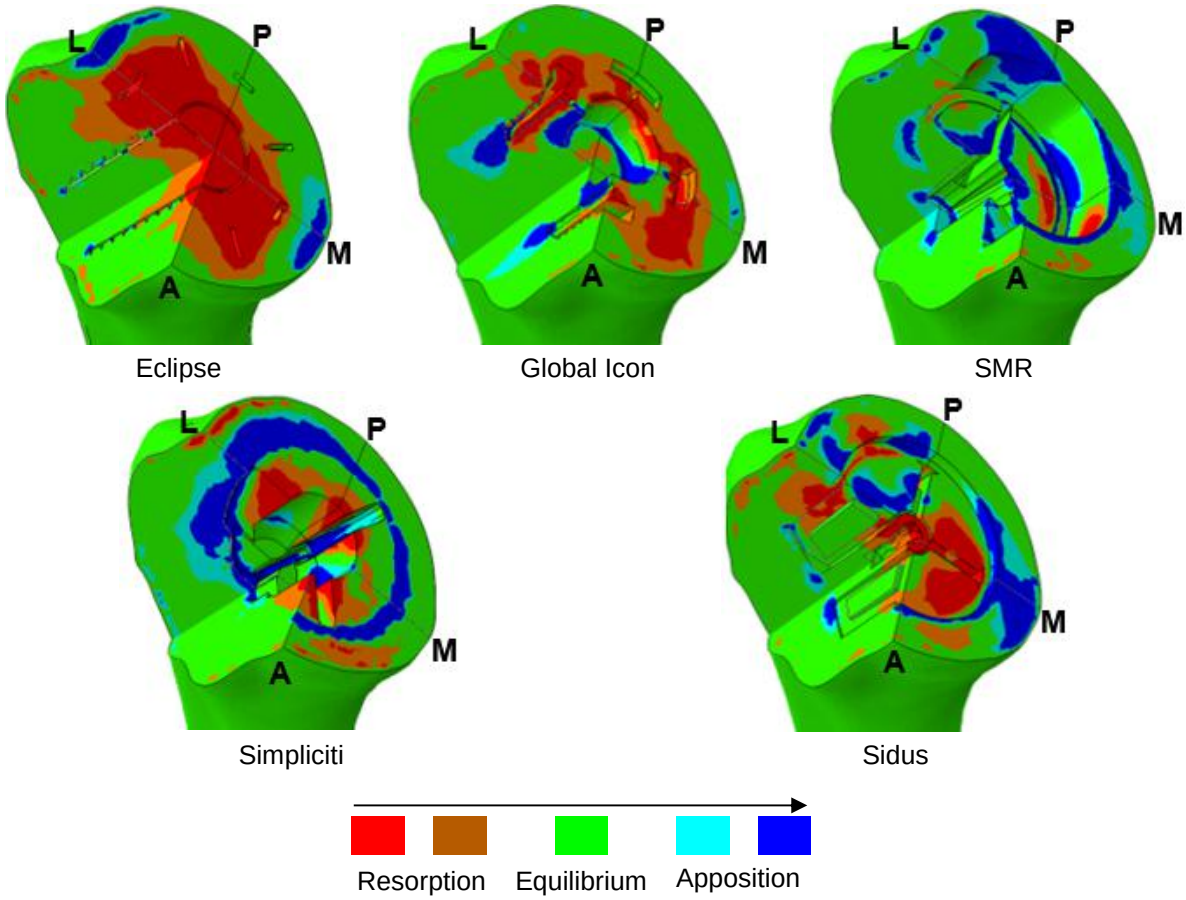

Figure 5-3 – Absolute changes, $\Delta\rho$, in bone density with respect to the intact bone, considering parameters k and m of 1.5 × 10^{-4} and 2, respectively. The legend L, P, M and A refers to the anatomical terms lateral, posterior, medial and anterior, respectively. The green color represents an equilibrium condition (-0.1 g cm^{-3} $< \Delta\rho <$ 0.1 g cm^{-3}). Bone resorption condition is depicted in red ($\Delta\rho < -0.2$ g cm^{-3}) and orange (-0.2 g cm^{-3} $\leq \Delta\rho \leq -0.1$ g cm^{-3}). Bone apposition is depicted in dark ($\Delta\rho >$ 0.2 g cm^{-3}) and light blue (0.1 g cm^{-3} $\leq \Delta\rho \leq$ 0.2 g cm^{-3}).

Regarding the Eclipse implant, bone resorption is observed in the central and superficial regions of the humerus in contact with the trunion. On the other hand, bone apposition is seen around the distal cage screw, and, superficially, between the border of the trunion and the lateral and medial regions of the resected humerus. For the Global Icon model, bone resorption is mostly seen in the superficial region of the resected humerus, while bone apposition is observed in the interface between bone and the distal end of the implant's fins, and in the central protuberance of the implant. Aside from some superficially anterior regions presenting bone resorption, the predominant effect in the SMR model was bone apposition, which occurred at the angular interfaces between bone and the core component, and in the

bone surface in contact with the humeral head of the implant. In the Simpliciti model, the boundary between bone and the peripheral border of the nucleus' collar showed bone apposition. A similar result is also observed along the nucleus' fins. Bone resorption occurred mainly in the central, superficial region of the resected humerus, covered by the nucleus collar. The Sidus implant caused superficial bone resorption mainly at the central medial region of the resected humerus. Bone apposition was predicted in the interfaces between bone and the distal borders of the anchor' fins, as well as in the superficial medial regions of the humerus in contact with the humeral head implant. In all 5 models, bone resorption is observed in the superficial, anteromedial regions. Regions presenting bone resorption may indicate unloaded bone stock due to the presence of the implant, and bone apposition may be due to the load being transferred to the bone in the mentioned regions.

Table 5-2 presents in detail the changes in bone mass for each ROI and each implant. Negative values reflect bone mass loss whereas positive values reflect bone mass gain. For consistency, the colour code used refers to bone adaption phenomena such as bone resorption, bone apposition and equilibrium condition according to Figure 5-3. However, the equilibrium condition was arbitrarily defined for a change in bone mass below 5 %, and the boundary of the remaining level was arbitrarily defined for a change in bone mass of 10 %.

Table 5-2 – Changes in bone mass, in percentage, for each ROI with respect to the intact bone, considering k and m parameters of 1.5×10^{-4} and 2, respectively. The colour code refers to Figure 5-3. However, the equilibrium condition was arbitrarily defined for a change in bone mass below 5 %, and the boundary of the remaining level was arbitrarily defined for a change in bone mass of 10 %.

ROI		Eclipse		Global Icon		SMR		Simpliciti		Sidus	
S	L	-20.03	-17.48	-3.11	-6.85	-4.50	-1.87	7.44	0.65	-16.57	-11.83
	P	-7.79		-7.49		10.51		1.76		-1.69	
	M	-9.58		-8.82		-0.57		-2.82		-8.10	
	A	-28.53		-9.45		-8.45		-4.76		-22.82	
D	L	-8.70	-8.72	15.81	4.92	1.49	0.55	23.46	9.76	-7.67	-2.54
	P	0.92		-3.69		5.94		6.89		7.59	
	M	-5.72		0.87		-0.40		8.33		-0.76	
	A	-19.27		7.69		-2.22		1.26		-11.06	
Total		-13.93		-1.81		-0.67		4.54		-7.84	

Both Eclipse and Sidus implants caused a loss in bone mass in the superficial region of the humerus, losing 13.9 % and 7.8 % of bone mass, respectively, in all the humeral head region. Overall, the remaining 3 implants did not cause significant changes in bone mass since at the end of the simulation the implants presented a moderate change in bone mass, inferior to 5 %. Among these 3 implants, the Simpliciti implant stood out from the rest by presenting a relevant bone mass gain, 9.8 %, in the deep region of the humeral head.

One interesting finding is that all humeral implants containing a solid collar that covers the entire resected surface caused a superficial negative effect in the change in bone mass compared to a collar that does not cover the entire resected surface. Unfortunately, regarding the absence of a solid collar, no conclusions can be drawn about its effect on the superficial change in bone mass. Notice that despite

both Sidus and SMR implants not having a solid collar, the SMR implant does not preserve the bone inside the core, which prevents its evaluation.

The overall change in bone mass due to the virtual shoulder arthroplasty and the posterior bone adaptation process is graphically represented in Figure 5-4. The stages considered were the stage before the arthroplasty, 0^-, the stage immediately after the arthroplasty, 0^+, and the stage in the end of the bone remodelling simulation, 1, after the adaptation of bone to the implant.

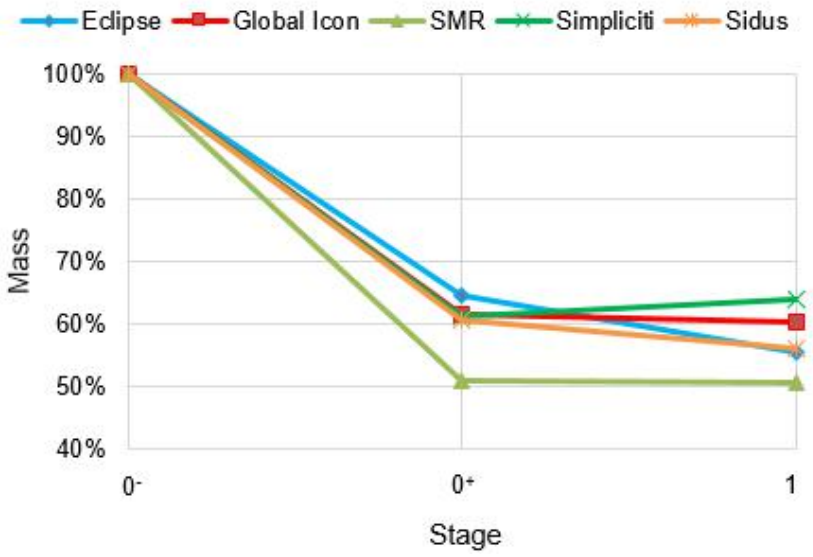

Figure 5-4 – Percentage of bone mass in three distinct stages: 0^- denotes the humeral head mass before the arthroplasty, 0^+ represents the mass of humeral head immediately after the arthroplasty, and 1 denotes the humeral head mass, after the adaptation of bone to the implant.

For a detailed analysis, Table 5-3 presents the overall change in bone mass, in percentage, with respect to the stage before the arthroplasty. Note that negative values represent bone mass loss.

Table 5-3 – Overall change in bone mass, in percentage, with respect to the stage before the arthroplasty.

	Stage	Eclipse	Global Icon	SMR	Simpliciti	Sidus
Surgery/Implantation ↓	0^-	0.00	0.00	0.00	0.00	0.00
	0^+	-35.54	-38.43	-48.94	-38.83	-39.28
Bone adaptation ↓	1	-44.52	-39.54	-49.28	-36.05	-44.04

The SMR implant is the implant that removed the largest amount of bone mass during the arthroplasty, whereas the Eclipse is the implant that removed less bone mass. Despite the Eclipse implant being the implant that caused the largest bone mass loss during the bone adaption process, it is the SMR model that presented the lowest bone mass. Yet, it is worth noticing that the change in bone mass due to the bone adaptation process caused by the SMR implant was only 0.7 %.

The qualitative and quantitative results obtained considering a fully absent osseointegration condition are presented in Figure 5-5 and Table 5-4, respectively. Overall, all 5 models showed a reduction in bone resorption and an increase in bone apposition in comparison to the full osseointegration condition. For the Eclipse model, the major difference was the bone apposition in the regions where the trunion's fins contact the bone. In the Global Icon model, a reduction in bone resorption in the

superficial, central region is observed, whereas areas of bone apposition appeared in the superficial, posterolateral region of the resected humerus. The major difference in the SMR model consisted on an increase of bone apposition in the superficial, posterior, and medial regions of the resected humerus.

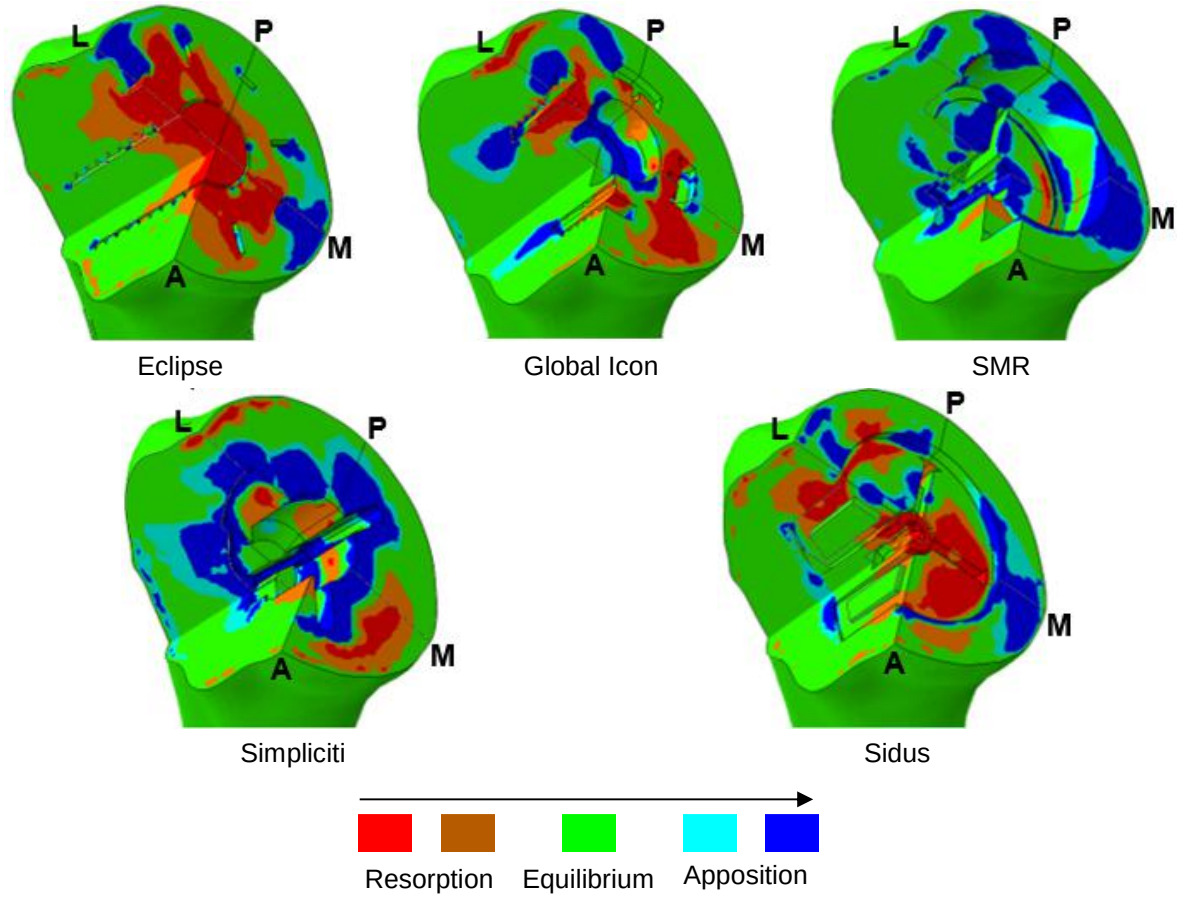

Figure 5-5 – Absolute changes in bone density with respect to the intact bone, considering parameters k and m of 1.5×10^{-4} and 2, respectively, and a fully absent osseointegration condition. The legend L, P, M and A refers to the anatomical terms lateral, posterior, medial and anterior, respectively. The green color represents an equilibrium condition (-0.1 g cm^{-3} $< \Delta\rho <$ 0.1 g cm^{-3}). Bone resorption condition is depicted in red ($\Delta\rho < -0.2$ g cm^{-3}) and orange (-0.2 g cm^{-3} $\leq \Delta\rho \leq -0.1$ g cm^{-3}). Bone apposition is depicted in dark ($\Delta\rho >$ 0.2 g cm^{-3}) and light blue (0.1 g cm^{-3} $\leq \Delta\rho \leq$ 0.2 g cm^{-3}).

Regarding the Simpliciti model, the bone resorption in the superficial, central region of the resected humerus was replaced by a high level of bone apposition. An increase of bone apposition also occurred in the deep region of the resected humerus. On the other hand, there was an increase in bone resorption in the superficial, anteromedial region. In the Sidus model, there were no visually noticeable changes in the results, but quantitatively, bone apposition increased in the superficial, posterior region. The Eclipse model presented the greatest bone mass loss, 10.6 %, followed by the Sidus model with a more moderate bone mass loss of 4.2 %. The Global Icon and SMR models also presented a moderate change in bone mass of 1.8 % and 3.6 %, respectively, whereas the Simpliciti model had a gain in its bone mass of 9.5 %.

Table 5-4 – Changes in bone mass, in percentage, for each ROI with respect to the intact bone, considering parameters k and m of 1.5 × 10^{-4} and 2, respectively, and a fully absent osseointegration condition. The colour code refers to Figure 5-5. However, the equilibrium condition was arbitrarily defined for a change in bone mass below 5 %, and the boundary of the remaining level was arbitrarily defined for a change in bone mass of 10 %.

ROI		Eclipse		Global Icon		SMR		Simpliciti		Sidus	
S	L	-12.30	-12.32	2.88	-2.19	-1.98	3.14	13.97	5.25	-11.62	-5.72
	P	-2.24		2.78		15.76		12.97		7.47	
	M	-6.19		-6.30		10.70		-0.78		-0.87	
	A	-24.87		-8.72		-7.60		-4.99		-17.55	
D	L	-7.09	-8.06	22.25	7.36	4.93	4.03	34.75	15.10	-6.64	-2.13
	P	1.29		-2.32		11.84		10.12		11.12	
	M	-5.26		1.25		3.54		12.12		-1.36	
	A	-19.04		10.58		-0.93		5.19		-12.10	
Total		-10.60		1.90		3.58		9.45		-4.18	

5.2.1. Sensitivity analysis

The total change in bone mass is presented in Table 5-5 for all implants considering a parameter m of 2 and parameters k of 0.75×10^{-4} and 2.25×10^{-4}. For the sake of briefness, the remaining results are only presented in the Appendix. The parameters k of 0.75×10^{-4} and 2.25×10^{-4} are 50 % smaller and 50 % larger, respectively, than that deemed as best. The results showed that a decrease in the parameter k led to a decrease in bone resorption and an increase in bone apposition, whereas an increase in the parameter k leads to an increase in bone resorption and a decrease in bone apposition. Nonetheless, despite the quantitative changes in bone mass, no relevant differences were observed qualitatively, i.e., all 5 models maintained their relative performances.

Table 5-5 – Total change in bone mass, in percentage, with respect to the intact bone considering a parameter m of 2 and parameters k of 0.75×10^{-4} and 2.25×10^{-4}. The colour code refers to Figure 5-5. However, the equilibrium condition was arbitrarily defined for a change in bone mass below 5 %, and the boundary of the remaining level was arbitrarily defined for a change in bone mass of 10 %.

Parameters	Eclipse	Global Icon	SMR	Simpliciti	Sidus
k = 0.75×10^{-4} m = 2	-9.1	2.3	1.8	7.3	-4.2
k = 2.25×10^{-4} m = 2	-17.7	-5.1	-2.8	2.1	-11.0

6. Discussion

The objective of this study was to assess to what extent the bone adaptation process of the proximal humerus is affected by the distinct geometries of 5 stemless implants, available in the market. To accomplish that, 3-D finite element models of the stemless implants were applied along with a bone adaption model. The bone remodelling simulations were performed using the parameters selected in the bone remodelling model validation step, which were deemed as the best to simulate the actual humerus density distribution. The parameters selected as best presented low RMSE and ME between the computational predictions and the actual bone density distribution of the humerus under analysis, which provides confidence on the results. For the implanted bone models, the initial condition was defined as the bone density distribution obtained for the intact bone model using the set of parameters selected as best. The analysis of the results was performed qualitatively, by visually comparing the absolute changes in bone density with respect to the intact bone and, quantitatively, by computing the changes in bone mass for different ROI. Overall, the results obtained show that the differences in the implants' geometry influence the bone adaption process.

Overall, the Eclipse model presented the highest total bone mass loss, followed by the Sidus model, whereas the Global Icon and SMR models presented a moderate bone mass loss. The Simpliciti model stood out from the rest as it was the only one leading to an increase in total bone mass. The results obtained in this work show a great change in bone mass in the anterior superficial region, as well as relevant changes in the lateral superficial region of the proximal humerus. Apart from the changes in bone mass due to bone adaptation, it is worth noticing that the SMR implant is the one that removes more mass during its implantation, as opposed to the Eclipse model, which is the implant that preserves more bone. However, although the SMR model removes more bone mass, it is the one that shows the less impact on the bone remodelling of the humerus showing very little bone resorption. From the bone adaption process point of view, the Global Icon, SMR, and Simpliciti implants showed a good performance. However, the superior bone resorption level predicted for the Global Icon and Simpliciti models at the superficial central region of the implant's fixation might suggest a better long-term performance of the SMR, even regardless of the gain in bone mass predicted for the Simpliciti implant, because the bone loss observed for the former implants could lead to loosening over time (Quental et al., 2014a; Reeves et al., 2018). Nevertheless, further investigation focusing on the long-term implant stability could give a better understanding on whether preserving bone stock should be preferred, despite bone resorption might occurring, over removing more bone stock during the surgical procedure, but avoiding bone resorption. For the fully absent osseointegration condition, there was a general increase in bone apposition and a decrease in bone resorption. Nevertheless, the findings from the full osseointegration condition remained, as the relationship among the 5 implant models did not change.

Regarding the influence of the collar type on the bone adaption process, for the 3 implants that present a solid collar (Eclipse, Global Icon, and Simpliciti), bone resorption occurred in the superficial, central region of the resected humerus, which is covered by the collar. This might be explained by the stress shielding phenomenon, i.e., the loads are transferred through the implant, causing a decrease in the

mechanical stimulus in the bone that leads to bone resorption. Previous mid-term radiologic results about the Eclipse implant also showed bone mass loss and occurrence of stress shielding in this region (Habermeyer et al., 2015; Heuberer et al., 2018). Churchill & Athwal (2016) suggested that in the case of stress shielding and bone resorption occurring, collared implants may provide more stability contrarily to collarless implants. However, the bone loss observed in this study for the collared implants, at the superficial central region of the implant's fixation under the collar, could lead to implant loosening (Quental et al., 2014a). Therefore, further computational investigation should assess the long-term stability of stemless implants. Nevertheless, the short, mid and long-term radiologic studies about stemless implants report no loosening of the humeral component due to stress shielding (Habermeyer et al., 2015; Churchill et al., 2016; Hawi et al., 2017; Heuberer et al., 2018). Bone formation in the superficial region of the resected humerus was observed for the Simpliciti model at the edge of the solid collar. Its solid collar rests on the trabecular bone inside the cortical rim, instead of resting on the cortical rim. This type of solid collar might be advantageous as it allows a better transfer of loads to the metaphyseal region. The 2 implants that do not have a solid collar allow the contact between the humeral head component and the resected bone surface, which allows the transfer of load through these regions, and thus leads to bone apposition. The bone resorption in the superficial region of the Sidus model may be due to the open collar as no load is transferred to this region. The SMR implant is collarless and very little bone resorption occurred in the superficial region. Yet, notice that no bone stock exists inside the core. Because there is only one collarless implant model and one implant model with an open collar, no definite conclusions can be taken about these types of collars.

With respect to the fixation mode, the Eclipse implant is fixed by screw-in in the central region of the resected humerus, while the remaining 4 implants are impacted into the bone. The Global Icon implant is fixed through impaction with 4 peripheral legs and one central protuberance, the Sidus implant through 4 cross shaped open-windowed fins, and the Simpliciti and SMR implants through a central body with 3 fins that avoid the implant rotation. Unfortunately, since only one implant fixed by screw-in was analysed, no definite recommendations can be made regarding the fixation mode. Comparing the fixation features of the 4 implants fixed by impaction, the Sidus model showed a bone loss superior than that observed for the Simpliciti, Global Icon, and SMR models. However, this cannot be directly linked to the amount and shape of fins because other distinct features, such as the fixation position, might have played a role as well. According to Reeves et al. (2017) and Alidousti et al. (2017), the average apparent density in the proximal humerus decreases from the superficial to deep regions, and increases from the central to peripheral regions. Therefore, to seek fixation in a denser region, the design of the stemless implants should take advantage of the peripheral regions within the first 15-20 mm beneath the humeral head resection surface. Among these 4 implants, the Sidus implant is the system whose fins cover a more central region.

To the author's knowledge, there are no other FE studies addressing the effect of the geometry of distinct stemless implants, available in the market, in the bone remodelling process of the humerus. Reeves et al. (2018) addressed the effect of stemless humeral component fixation feature design on bone stress and strain response considering generic stemless implants. The implants analysed were classified

according to the fixation feature location: central, peripheral, and boundary-crossing (when the central-peripheral boundary is crossed). Among others, one variable measured was the simulated potential bone response at the stage immediately after surgery, computed by the percentage of bone volume that would be expected to resorb, remain unchanged, or remodel based on the strain energy density changes between the implanted and intact models. In their conclusions, central implants presented the best performance as those implants produced the least simulated resorbing potential in cortical and trabecular bone, with boundary-crossing implants having the highest simulated trabecular remodelling potentials. The results obtained in this work cannot be directly compared with those obtained by Reeves et al. (2018) because, first, they simulated a potential bone response at the stage immediately after surgery instead of effectively simulating an iterative bone remodelling process, and second, there are no identical implants' geometries in the 2 studies. The results obtained in this work show a great change in bone mass in the anterior superficial region, as well as relevant changes in the lateral superficial region, which is in agreement with the findings of Reeves et al. (2018), as well as the radiologic outcomes of stemless implants reported by Habermeyer et al. (2015) and Krukenberg et al. (2018), and a single-photon emission CT/CT by Berth et al. (2015) who evaluated the local metabolic bone activity after a stemless shoulder arthroplasty. Moreover, Gallacher et al. (2018) reported radiolucencies lines beneath the trunion base plate of the Eclipse implant, stating that they could represent stress shielding, which was confirmed in this study. Recently, in a study about the bone remodelling process due to the Sidus Stem-Free Shoulder System, Santos et al. (2018) reported, through the computation of the change in bone mass, that the stemless model analysed showed bone resorption around the anchor, and bone apposition around the anchor edges and at the end of the anchor open-windowed fins. Quantitatively, the greatest bone mass loss occurred, superficially, in the anterior-superior and posterior-superior ROIs, while a moderated gain in bone mass occurred, deeply, in the posterior-superior ROI. The remaining ROIs showed bone mass loss within -3 % to -9 %. Despite some differences, which may be due to the different definition of the ROIs, the quantitative results obtained in this work for the Sidus implant are in accordance with those from Santos et al. (2018), as the greatest bone mass loss occurred, superficially, in the lateral and anterior ROIs, and a gain in bone mass was observed in the deep posterior ROI. Qualitatively, some local differences are observed compared to Santos et al. (2018). The averaging of the change in bone mass for each ROI hide some local effects which could explain these differences. In this work, a smaller amount of bone resorption is estimated in the superficial central region. In the lateral region, bone resorption around the implant's fins and less bone formation at the end of the implant's fins is observed. The differences observed between this study and that from Santos et al. (2018) are likely due to the differences in the loading conditions. This study considers not only the forces produced at the muscle attachment sites but also those due to the wrapping of muscles over the anatomical structures whereas Santos et al. (2018) only considered the forces at the muscle attachment sites.

Despite its contributions, the present work contains some limitations. First, only one humerus' geometry was studied. Even though it would have been valuable to have more than one humerus geometry, the dimensions of the humerus analysed fall within those of typical humeri, and thus the results are expected to be representative of humeri in general (Hertel et al., 2002). Regarding the loading conditions, the use

of 6 load cases strengths the model. Yet, the addition of more load cases would allow a closer approximation to reality. In the remodelling simulations, the osseointegration process was not modelled. To evaluate the impact of this limitation, two extreme conditions for osseointegration were considered: an idealized condition of full osseointegration and a worst-case condition of absence of osseointegration. Even though quantitative differences were observed in the results due to the osteointegration conditions, no differences were observed qualitatively. The implants' models were not provided by the manufacturers, thus all the 5 prostheses were modelled according to the information available on the surgical technique guides or in the product's brochures. In other words, differences may exist between the modelled implants and the implants produced by the manufacturers. The significant variability in the geometry of the implants analysed prevented definite conclusions about some design features due to the absence of an identical implant only differing in one design feature. Nevertheless, the overall analysis could give an extensive insight about the performance of 5 commercialized stemless implants. The model was validated considering only its ability to reproduce the actual density distribution of the humerus. However, to provide further confidence on the results, further analyses were performed to evaluate the influence of the parameter k on the results. The sensitivity analysis performed showed that a change of 50 % in the parameter k did not change the findings of this study.

7. Conclusion and future work

The goal of the present work was to assess the influence of the geometry of 5 stemless implants, available in the market, in the bone adaption process of the humerus after a shoulder arthroplasty. To accomplish that, 3-D finite element models associated with a bone remodelling model were used. The validation of the bone remodelling model through the simulation of the actual density distribution of the humerus provided confidence in the results. Additionally, this work was strengthened by the application of 6 loads, including muscle and joint reaction forces, which were based on the same subject studied here.

Overall, the geometry was shown to influence the bone adaption process of the humerus. From the bone remodelling point of view, the Global Icon, SMR, and Simpliciti implants showed a good performance, whereas the Eclipse implant had the worst performance, followed by the Sidus implant. However, the superior bone resorption level predicted for the Global Icon and Simpliciti models at the superficial central region of the implant's fixation might suggest a better long-term performance of the SMR, even regardless of the gain in bone mass predicted for the Simpliciti implant, because the bone loss observed for the former implants could lead to loosening over time (Quental et al., 2014a; Reeves et al., 2018). Although these findings may give indications to manufacturers and orthopaedic surgeons about the influence of the geometry in the bone adaptation process of the humerus, long-term clinical and radiological outcomes addressing more implants are essential to better understand the performance of stemless implants in the long-term.

To the author's knowledge, this is the first study to perform such an extensive evaluation of the impact of the geometry of stemless implants, available in the market, on the bone adaption process of the humerus after a shoulder arthroplasty. Nonetheless, much work remains to be done.

A larger number of humeri should be considered in future studies. Additionally, further investigation is needed to assess the stability of the implants. The results obtained for the bone remodelling process together with the stability assessment would allow to understand the consequences of bone mass loss in the long-term stability of the implant. A better understanding about the influence of each feature design of stemless implants on the bone adaption process is needed. For that purpose, for each implant available in the market, an identical model should be developed, only changing one feature design, and comparing its bone remodelling results with the original model. This will allow to understand, without biasing, the influence of that specific feature design. Examples of a feature design could be the type of collar, the number of fins, and the type of fixation.

8. References

Aebli, N., Krebs, J., Stich, H., Schawalder, P., Walton, M., Schwenke, D., Theis, J. C. (2003). In vivo comparison of the osseointegration of vacuum plasma sprayed titanium- and hydroxyapatite-coated implants. *Journal of Biomedical Materials Research - Part A*, *66*(2), 356–363.

Alidousti, H., Giles, J. W., Emery, R. J. H., & Jeffers, J. (2017). Spatial mapping of humeral head bone density. *Journal of Shoulder and Elbow Surgery*, *26*(9), 1653–1661.

Arthrex. (2018). Arthrex ECLIPSE™ – Stemless Shoulder Prosthesis - Surgical Technique. Retrieved from http://www.clinicaltrials.gov/ct2/show/NCT01790113?term=arthrex+eclipse&rank=1

Ballas, R., & Béguin, L. (2013). Results of a stemless reverse shoulder prosthesis at more than 58 months mean without loosening. *Journal of Shoulder and Elbow Surgery*, *22*(9).

Beck, S., Beck, V., Wegner, A., Dudda, M., Patsalis, T., & Jäger, M. (2018). Long-term survivorship of stemless anatomical shoulder replacement. *International Orthopaedics*, *42*(6), 1327–1330.

Berth, A., März, V., Wissel, H., Awiszus, F., Amthauer, H., & Lohmann, C. H. (2015). SPECT/CT demonstrates the osseointegrative response of a stemless shoulder prosthesis. *Journal of Shoulder and Elbow Surgery*, *25*(4), e96–e103.

Berth, A., & Pap, G. (2013). Stemless shoulder prosthesis versus conventional anatomic shoulder prosthesis in patients with osteoarthritis. *Journal of Orthopaedics and Traumatology*, *14*(1), 31–37.

Bohsali, K. I. (2006). Complications of Total Shoulder Arthroplasty. *The Journal of Bone and Joint Surgery (American)*, *88*(10), 2279.

Boileau, P., Sinnerton, R. J., Chuinard, C., & Walch, G. (2006). Arthroplasty of the shoulder. *The Journal of Bone and Joint Surgery. British Volume*, *88–B*(5), 562–575.

Brodner, W., Bitzan, P., Lomoschitz, F., Krepler, P., Jankovsky, R., Lehr, S., Gottsauner-Wolf, F. (2004). Changes in bone mineral density in the proximal femur after cementless total hip arthroplasty. *The Journal of Bone and Joint Surgery. British Volume*, *86–B*(1), 20–26.

Buzug, T. (2008). *Computed tomography: From photon statistics to modern cone-beam CT*. *Computed Tomography: From Photon Statistics to Modern Cone-Beam CT*. Springer.

Churchill, R. S. (2014). Stemless shoulder arthroplasty: Current status. *Journal of Shoulder and Elbow Surgery*, *23*(9), 1409–1414.

Churchill, R. S., & Athwal, G. S. (2016). Stemless shoulder arthroplasty—current results and designs. *Current Reviews in Musculoskeletal Medicine*, *9*(1), 10–16.

Churchill, R. S., Chuinard, C., Wiater, J. M., Friedman, R., Freehill, M., Jacobson, S., Nicholson, G. P. (2016). Clinical and radiographic outcomes of the simpliciti canal-sparing shoulder arthroplasty system. *Journal of Bone and Joint Surgery - American Volume*, *98*(7), 552–560.

Cifuentes, A. O., & Kalbag, A. (1992). A performance study of tetrahedral and hexahedral elements in 3-D finite element structural analysis. *Finite Elements in Analysis and Design*, *12*(3–4), 313–318.

Cignoni, P., Cignoni, P., Callieri, M., Callieri, M., Corsini, M., Corsini, M., Ranzuglia, G. (2008). MeshLab: an Open-Source Mesh Processing Tool. *Sixth Eurographics Italian Chapter Conference*, (February 2015), 129–136.

Coley, B., Jolles, B. M., Farron, A., & Aminian, K. (2008). Arm position during daily activity. *Gait and Posture*, *28*(4), 581–587.

Coley, B., Jolles, B. M., Farron, A., & Aminian, K. (2009). Detection of the movement of the humerus during daily activity. *Medical and Biological Engineering and Computing*, *47*(5 SPEC. ISS.), 467–474.

Dassault Systèmes. (2015). Abaqus 2016 Online Documentation - Abaqus/CAE User's Guide. Retrieved August 25, 2018, from http://130.149.89.49:2080/v2016/index.html

DePuy Synthes. (2017a). Global Icon™ Stemless Shoulder System - Design Rationale.

DePuy Synthes. (2017b). Global Icon™ Stemless Shoulder System - Surgical Technique.

Eberle, S., & Augat, P. (2007). Preventing Contact Convergence Problems in Bone- Implant Contact Models. *ANSYS Conference 25th CADHEM Users Meeting 2007*, 21–25.

Fat, D. L., Kennedy, J., Galvin, R., O'Brien, F., Grath, F. M., & Mullett, H. (2012). The Hounsfield value for cortical bone geometry in the proximal humerus-an in vitro study. *Skeletal Radiology*, *41*(5), 557–568.

Favre, P., & Henderson, A. D. (2016). Prediction of stemless humeral implant micromotion during upper limb activities. *Clinical Biomechanics*, *36*, 46–51.

Favre, P., Snedeker, J. G., & Gerber, C. (2009). Numerical modelling of the shoulder for clinical applications. *Philosophical Transactions of the Royal Society A: Mathematical, Physical and Engineering Sciences*, *367*(1895), 2095–2118.

Fernandes, P. R., Folgado, J., Jacobs, C., & Pellegrini, V. (2002). A contact model with ingrowth control for bone remodelling around cementless stems. *Journal of Biomechanics*, *35*(2), 167–176.

Fernandes, P., Rodrigues, H., & Jacobs, C. (1999). A model of bone adaptation using a global optimisation criterion based on the trajectorial theory of wolff. *Computer Methods in Biomechanics and Biomedical Engineering*, *2*(2), 125–138.

Folgado, J. (2004). *Modelos Computacionais para Análise e Projecto de Próteses Ortopédicas*. Instituto Superior Técnico.

Folgado, J., Fernandes, P. R., Guedes, J. M., & Rodrigues, H. C. (2004). Evaluation of osteoporotic bone quality by a computational model for bone remodeling. *Computers & Structures*, *82*(17–19), 1381–1388.

Gallacher, S., Williams, H. L. M., King, A., Kitson, J., Smith, C. D., & Thomas, W. J. (2018). Clinical and radiologic outcomes following total shoulder arthroplasty using Arthrex Eclipse stemless humeral component with minimum 2 years' follow-up. *Journal of Shoulder and Elbow Surgery*.

Gargiulo, P., Gislason, M. K., Edmunds, K. J., Pitocchi, J., Carraro, U., Esposito, L., Jónsson, H. (2017). CT-Based Bone and Muscle Assessment in Normal and Pathological Conditions. In *Reference Module in Biomedical Sciences*. Elsevier.

Gasbarro, G., Bondow, B., & Debski, R. (2017). Clinical anatomy and stabilizers of the glenohumeral joint. *Annals of Joint*, *2*, 58–58.

Grant, J. A., Bishop, N. E., Götzen, N., Sprecher, C., Honl, M., & Morlock, M. M. (2007). Artificial composite bone as a model of human trabecular bone: The implant-bone interface. *Journal of Biomechanics*, *40*(5), 1158–1164.

Guedes, J., & Kikuchi, N. (1990). Preprocessing and postprocessing for materials based on the homogenization method with adaptive finite element methods. *Computer Methods In Applied Mechanics and Engineering*, *83*(2), 143–198.

Gupta, S., & Dan, P. (2004). Bone geometry and mechanical properties of the human scapula using computed tomography data, *17*(2), 61–70.

Gupta, S., New, A. M. R., & Taylor, M. (2006). Bone remodelling inside a cemented resurfaced femoral head. *Clinical Biomechanics*, *21*(6), 594–602.

Habermeyer, P., Lichtenberg, S., Tauber, M., & Magosch, P. (2015). Midterm results of stemless shoulder arthroplasty: A prospective study. *Journal of Shoulder and Elbow Surgery*, *24*(9), 1463–1472.

Halloran, J. P., Petrella, A. J., & Rullkoetter, P. J. (2005). Explicit finite element modeling of total knee replacement mechanics. *Journal of Biomechanics*, *38*(2), 323–331.

Harmer, L., Throckmorton, T., & Sperling, J. W. (2016). Total shoulder arthroplasty: are the humeral components getting shorter? *Current Reviews in Musculoskeletal Medicine*, *9*(1), 17–22.

Hawi, N., Magosch, P., Tauber, M., Lichtenberg, S., & Habermeyer, P. (2017). Nine-year outcome after anatomic stemless shoulder prosthesis: clinical and radiologic results. *Journal of Shoulder and Elbow Surgery*, *26*(9), 1609–1615.

Hertel, R., Knothe, U., & Ballmer, F. T. (2002). Geometry of the proximal humerus and implications for prosthetic design. *Journal of Shoulder and Elbow Surgery*, *11*(4), 331–338.

Heuberer, P. R., Brandl, G., Pauzenberger, L., Laky, B., Kriegleder, B., & Anderl, W. (2018). Radiological changes do not influence clinical mid-term outcome in stemless humeral head replacements with hollow screw fixation: a prospective radiological and clinical evaluation. *BMC Musculoskeletal Disorders*, *19*(1), 28.

Hogg, M. (2013). bonemapy 0.4.1 : Python Package Index. Retrieved April 20, 2018, from https://pypi.org/project/bonemapy/

Huguet, D., DeClercq, G., Rio, B., Teissier, J., & Zipoli, B. (2010). Results of a new stemless shoulder prosthesis: Radiologic proof of maintained fixation and stability after a minimum of three years' follow-up. *Journal of Shoulder and Elbow Surgery*, *19*(6), 847–852.

Jacobs, C. R., Levenston, M. E., Beaupré, G. S., Simo, J. C., & Carter, D. R. (1995). Numerical instabilities in bone remodeling simulations: The advantages of a node-based finite element approach. *Journal of Biomechanics*, *28*(4), 449–459.

Johansson, L., Hailer, N. P., & Rahme, H. (2017). High incidence of periprosthetic joint infection with propionibacterium acnes after the use of a stemless shoulder prosthesis with metaphyseal screw fixation - a retrospective cohort study of 241 patients propionibacter infections after eclipse TSA. *BMC Musculoskeletal Disorders*, *18*(1), 203.

Kadum, B., Mafi, N., Norberg, S., & Sayed-Noor, A. S. (2011). Results of the Total Evolutive Shoulder System (TESS®): A single-centre study of 56 consecutive patients. *Archives of Orthopaedic and Trauma Surgery*, *131*(12), 1623–1629.

Klawitter, J. J., More, R. B., Gourley, M. R., Ritz, J. P., & Podnos, E. G. (2014). Humeral head resurfacing implant. Google Patents. Retrieved October 15, 2018, from https://patents.google.com/patent/US8690958

Krukenberg, A., McBirnie, J., Bartsch, S., Böhler, N., Wiedemann, E., Jost, B., Scheibel, M. (2018). Sidus Stem-Free Shoulder System for primary osteoarthritis: short-term results of a multicenter study. *Journal of Shoulder and Elbow Surgery*, *27*(8), 1483–1490.

Lima Corporate. (2016a). SMR Stemless - Brochure, (c), 1–4.

Lima Corporate. (2016b). SMR Stemless - Description. Retrieved October 15, 2018, from https://www.limacorporate.com/medical/77/smr-stemless.html

Lima Corporate. (2016c). SMR Stemless - Product Combination, 51500.

Lima Corporate. (2016d). SMR Stemless - Surgical Technique, (c), 1–4.

Lübbeke, A., Rees, J. L., Barea, C., Combescure, C., Carr, A. J., & Silman, A. J. (2017). International variation in shoulder arthroplasty. *Acta Orthopaedica*, *88*(6), 592–599.

Magosch, P., Habermeyer, P., Bachmaier, S., & Metcalfe, N. (2012). Biomechanische Grundlagen des metaphysär verankerten Humeruskopfersatzes. *Obere Extremitat*, *7*(1), 11–16.

Maier, M. W., Lauer, S., Klotz, M. C., Bülhoff, M., Spranz, D., & Zeifang, F. (2015). Are there differences between stemless and conventional stemmed shoulder prostheses in the treatment of

glenohumeral osteoarthritis? Orthopedics and biomechanics. *BMC Musculoskeletal Disorders*, *16*(1), 1–7.

Marieb, E. N. (2001). *Human Anatomy & Physiology* (5th ed.). Benjamin Cummings - An imprint of Addison Wesley longman, Inc.

Mata-Fink, A., & Bell, J.-E. (2016). Indications and Preoperative Evaluation for Anatomic Shoulder Arthroplasty. In *Anatomic Shoulder Arthroplasty* (pp. 1–13). Cham: Springer International Publishing.

Moroder, P., Ernstbrunner, L., Zweiger, C., Schatz, M., Seitlinger, G., Skursky, R., Krifter, R. M. (2016). Short to mid-term results of stemless reverse shoulder arthroplasty in a selected patient population compared to a matched control group with stem. *International Orthopaedics*, *40*(10), 2115–2120.

Movements of shoulder joint. (2016). Retrieved October 4, 2018, from http://sequencewiz.org/2016/03/16/loosen-up-your-shoulders/

Nagels, J., Stokdijk, M., & Rozing, P. M. (2003). Stress shielding and bone resorption in shoulder arthroplasty. *Journal of Shoulder and Elbow Surgery*, *12*(1), 35–39.

Neer, C. S. (1974). Replacement Arthroplasty for Glenohumeral Osteoarthritis. *The Journal of Bone & Joint Surgery*, *56*(1), 1–13.

Palastanga, N., & Soames, R. (2012). *Anatomy and Human Movement* (6th ed.). Elsevier Ltd.

Pearl, M. l., & Kurutz, S. (1999). Geometric Analysis of Commonly Used Prosthetic Systems for Proximal Humeral Replacement*. *The Journal of Bone & Joint Surgery*, *81*(5), 660–71.

Peters, O., & Maret, D. (2013). Effect of voxel size and partial volume effect on accuracy of tooth volumetric measurements with cone beam CT: Author response. *Dentomaxillofacial Radiology*, *42*(5), 20130070.

Pham, D. L., Xu, C., & Prince, J. L. (2000). Current methods in medical image segmentation. *Annual Review of Biomedical Engineering*, *2*, 315–37.

Prendergast, P. (1997). Finite element models in tissue mechanics and orthopaedic implant design. *Clinical Biomechanics*, *12*(6), 343–366.

Pressel, T., Lengsfeld, M., Leppek, R., & Schmitt, J. (2000). Bone remodelling in humeral arthroplasty: follow-up using CT imaging and finite element modeling - an in vivo case study. *Archives of Orthopaedic and Trauma Surgery*, *120*(5–6), 333–335.

Quental, C., Fernandes, P. R., Monteiro, J., & Folgado, J. (2014a). Bone remodelling of the scapula after a total shoulder arthroplasty. *Biomechanics and Modeling in Mechanobiology*, *13*(4), 827–838.

Quental, C., Folgado, J., Ambrósio, J., & Monteiro, J. (2012a). A multibody biomechanical model of the upper limb including the shoulder girdle. *Multibody System Dynamics*, *28*(1–2), 83–108.

Quental, C., Folgado, J., Fernandes, P. R., & Monteiro, J. (2012b). Bone remodelling analysis of the humerus after a shoulder arthroplasty. *Medical Engineering & Physics*, *34*(8), 1132–1138.

Quental, C., Folgado, J., Fernandes, P. R., & Monteiro, J. (2014b). Subject-specific bone remodelling of the scapula. *Computer Methods in Biomechanics and Biomedical Engineering*, *17*(10), 1129–1143.

Quilez, M. P., Seral, B., & Pérez, M. A. (2017). Biomechanical evaluation of tibial bone adaptation after revision total knee arthroplasty: A comparison of different implant systems. *PLOS ONE*, *12*(9), e0184361.

Rancourt, D., & Drouin, G. (1990). Friction properties of the interface between porous-surfaced metals and tibia1 cancellous bone, *24*, 1503–1519.

Razfar, N., Reeves, J. M., Langohr, D. G., Willing, R., Athwal, G. S., & Johnson, J. A. (2015). Comparison of proximal humeral bone stresses between stemless, short stem, and standard stem length: a

finite element analysis. *Journal of Shoulder and Elbow Surgery*, *25*(7), 1076–1083.

Reeves, J. M., Athwal, G. S., & Johnson, J. A. (2017). An assessment of proximal humerus density with reference to stemless implants. *Journal of Shoulder and Elbow Surgery*, *27*(4), 641–649.

Reeves, J. M., Langohr, G. D. G., Athwal, G. S., & Johnson, J. A. (2018). The effect of stemless humeral component fixation feature design on bone stress and strain response: a finite element analysis. *Journal of Shoulder and Elbow Surgery*.

Ribeiro, N. S., Fernandes, P. C., Lopes, D. S., Folgado, J. O., & Fernandes, P. R. (2009). 3-D solid and finite element modeling of biomechanical structures - a software pipeline. *7th EUROMECH Solid Mechanics Conference*, (OCTOBER). Retrieved October 15, 2018, from https://dspace.ist.utl.pt/bitstream/2295/391667/2/paper.pdf

Santos, B. (2017). *Bone remodelling analysis of the humerus after resurfacing and stemless shoulder arthroplasties*. Instituto Superior Técnico.

Santos, B., Quental, C., Folgado, J., Sarmento, M., & Monteiro, J. (2018). Bone remodelling of the humerus after a resurfacing and a stemless shoulder arthroplasty. *Clinical Biomechanics*, *59*(8), 78–84.

Sharma, G. B., & Robertson, D. D. (2013). Adaptive scapula bone remodeling computational simulation: Relevance to regenerative medicine. *Journal of Computational Physics*, *244*, 312–320.

Sheridan, B. D., Ahearn, N., Tasker, A., Wakeley, C., & Sarangi, P. (2012). Shoulder arthroplasty. Part 1: Prosthesis terminology and classification. *Clinical Radiology*, *67*(7), 709–715.

Sobocinski, M. (2015). Analysis of biobearings friction and wear processes. *Journal of Applied Mathematics and Computational Mechanics*, *14*(2), 103–109.

Spitzer, V., Ackerman, M. J., Scherzinger, a L., & Whitlock, D. (1996). The Visible Human Male: A Technical Report. *Journal of the American Medical Informatics Association*, *3*(2), 118–130.

Spranz, D. M., Bruttel, H., Wolf, S. I., Zeifang, F., & Maier, M. W. (2017). Functional midterm follow-up comparison of stemless total shoulder prostheses versus conventional stemmed anatomic shoulder prostheses using a 3D-motion-analysis. *BMC Musculoskeletal Disorders*, *18*(1), 7–11.

Swaminathan, V., & Gilbert, J. L. (2012). Fretting corrosion of CoCrMo and Ti6Al4V interfaces. *Biomaterials*, *33*(22), 5487–5503.

Taddei, F., Pancanti, A., & Viceconti, M. (2004). An improved method for the automatic mapping of computed tomography numbers onto finite element models. *Medical Engineering and Physics*, *26*(1), 61–69.

Taylor, M., & Prendergast, P. J. (2015). Four decades of finite element analysis of orthopaedic devices: Where are we now and what are the opportunities? *Journal of Biomechanics*, *48*(5), 767–778.

Tornier. (2014). Tornier SIMPLICITI™ Shoulder System - Instructions for Use, *49*(0), 7–8.

Tortora, G. J., & Derrickson, B. (2012). *Introduction to the Human Body* (9th ed.). John Wiley & Sons.

Total Shoulder Arthoplasty. (n.d.). Retrieved October 4, 2018, from https://www.moveforwardpt.com/symptomsconditionsdetail.aspx?cid=4e1deb00-f6fd-40d4-b28c-28319f0d6d4a

Vanhees, M., Jaspars, K. C. J., van Riet, R., Verborgt, O., & Declercq, G. (2013). Stemless revision of a failed hemiarthroplasty: Case report and surgical technique. *Journal of Shoulder and Elbow Surgery*, *22*(9), e14–e18.

Walsh, J. S. (2018). Normal bone physiology, remodelling and its hormonal regulation. *Surgery (United Kingdom)*, *36*(1), 1–6.

Wilk, K. E., Reinold, M. M., & Andrews, J. R. (2009). *The Athlete's Shoulder* (2nd ed.). Churchill Livingstone Elsevier.

Williams, Gerald R., Ken Yamaguchi, and M. L. R. (2015). *Shoulder and Elbow Arthroplasty*. Philadelphia: Wolters Kluwer.

Wright. (2016). Tornier SIMPLICITI™ Shoulder System - Surgical Technique.

Wright. (2017). Tornier SIMPLICITI™ Shoulder System - Brochure.

Yushkevich, P. A., Piven, J., Hazlett, H. C., Smith, R. G., Ho, S., Gee, J. C., & Gerig, G. (2006). User-guided 3D active contour segmentation of anatomical structures: Significantly improved efficiency and reliability. *NeuroImage*, *31*(3), 1116–1128.

Zimmer. (2012). Sidus™ Stem-Free Shoulder - Surgical Technique.

Zimmer. (2014). Sidus™ Stem-Free Shoulder. Retrieved October 15, 2018, from http://www.zimmer.co.uk/medical-professionals/products/shoulder/zimmer-sidus-shoulder.html

9. Appendix

9.1. Change in bone mass for k and m parameters of 0.75×10^{-4} and 2, respectively.

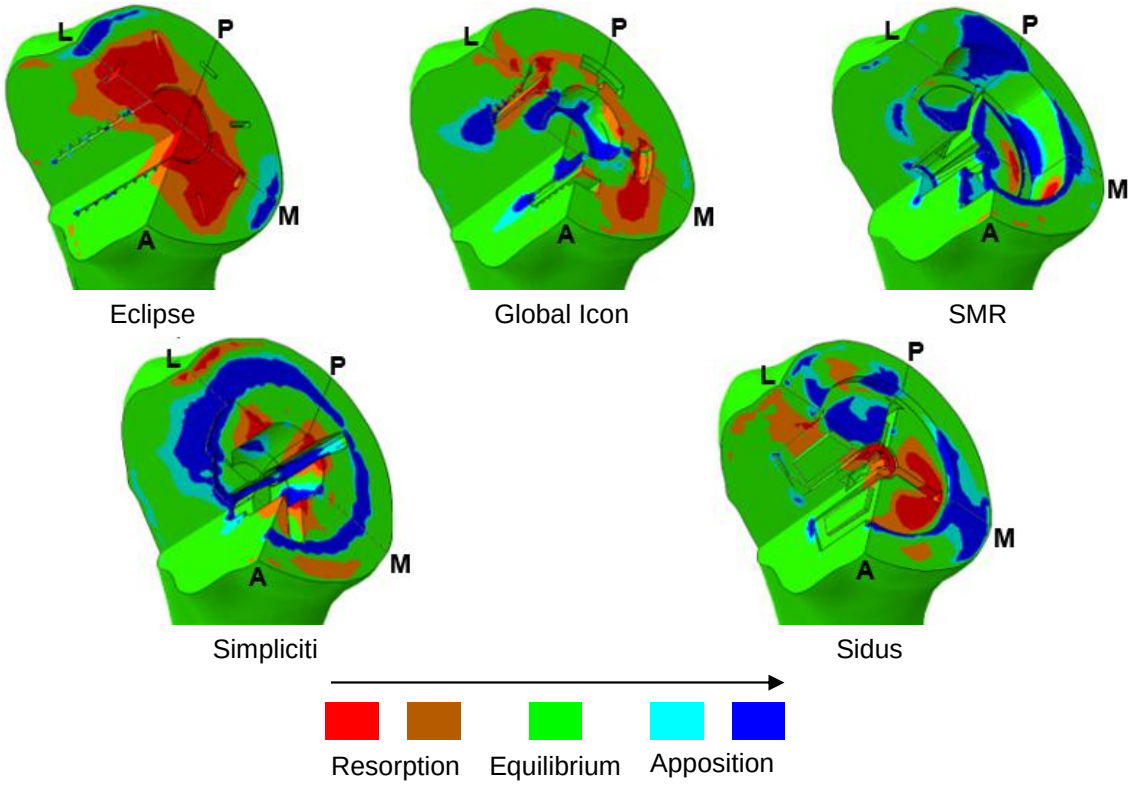

Figure 9-1 – Absolute changes in bone density with respect to the intact bone, considering parameters k and m of 0.75×10^{-4} and 2, respectively. The legend L, P, M and A refers to the anatomical terms lateral, posterior, medial and anterior, respectively. The green color represents an equilibrium condition (-0.1 g cm^{-3} $< \Delta\rho <$ 0.1 g cm^{-3}). Bone resorption condition is depicted in red ($\Delta\rho <$ -0.2 g cm^{-3}) and orange (-0.2 g cm^{-3} $\leq \Delta\rho \leq$ -0.1 g cm^{-3}). Bone apposition is depicted in dark ($\Delta\rho >$ 0.2 g cm^{-3}) and light blue (0.1 g cm^{-3} $\leq \Delta\rho \leq$ 0.2 g cm^{-3}).

Table 9-1 – Changes in bone mass, in percentage, for each ROI with respect to the intact bone, considering parameters k and m of 0.75×10^{-4} and 2, respectively. The colour code refers to Figure 9-1. However, the equilibrium condition was arbitrarily defined for a change in bone mass below 5 %, and the boundary of the remaining level was arbitrarily defined for a change in bone mass of 10 %.

ROI		Eclipse		Global Icon		SMR		Simpliciti		Sidus	
S	L	-14.37	-11.51	3.99	-0.12	-1.14	1.73	12.96	5.35	-10.23	-6.14
	P	-4.68		-1.69		11.60		5.07		1.04	
	M	-5.98		-3.62		1.24		0.67		-3.67	
	A	-18.05		0.09		-0.96		2.16		-12.64	
D	L	-6.69	-5.59	14.64	5.49	2.44	1.68	21.59	9.77	-6.35	-1.74
	P	0.74		-1.70		5.07		6.34		4.94	
	M	-3.56		2.78		0.49		8.92		0.02	
	A	-11.42		5.59		0.73		3.03		-7.19	
Total		-9.09		2.30		1.78		7.25		-4.23	

9.2. Change in bone mass for k and m parameters of 2.25×10^{-4} and 2, respectively.

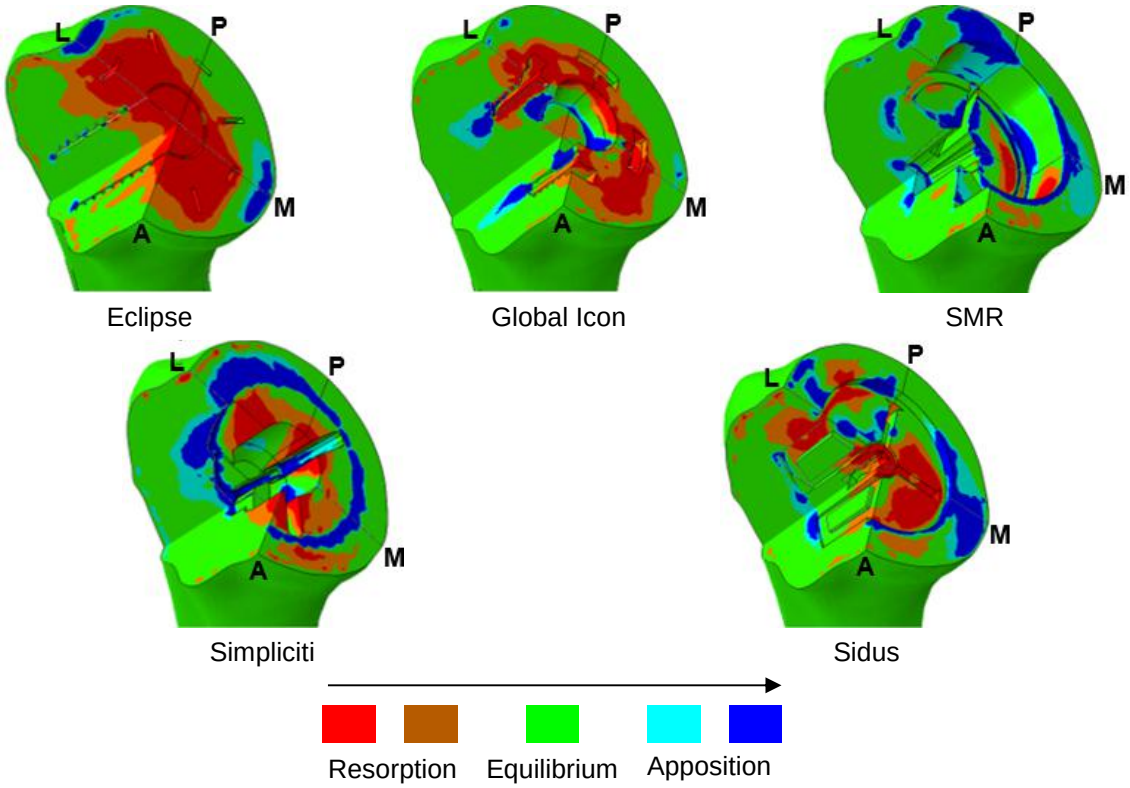

Figure 9-2 – Absolute changes in bone density with respect to the intact bone, considering parameters k and m of 2.25×10^{-4} and 2, respectively. The legend L, P, M and A refers to the anatomical terms lateral, posterior, medial and anterior, respectively. The green color represents an equilibrium condition (-0.1 g cm$^{-3} < \Delta\rho < 0.1$ g cm^{-3}). Bone resorption condition is depicted in red ($\Delta\rho < -0.2$ g cm^{-3}) and orange (-0.2 g cm$^{-3} \leq \Delta\rho \leq -0.1$ g cm^{-3}). Bone apposition is depicted in dark ($\Delta\rho > 0.2$ g cm^{-3}) and light blue (0.1 g cm$^{-3} \leq \Delta\rho \leq 0.2$ g cm^{-3}).

Table 9-2 – Changes in bone mass, in percentage, for each ROI with respect to the intact bone, considering parameters k and m of 2.25×10^{-4} and 2, respectively. The colour code refers to Figure 9-2. However, the equilibrium condition was arbitrarily defined for a change in bone mass below 5 %, and the boundary of the remaining level was arbitrarily defined for a change in bone mass of 10 %.

ROI		Eclipse		Global Icon		SMR		Simpliciti		Sidus	
S	L	-23.48	-22.19	-8.25	-12.21	-6.84	-5.04	3.25	-3.38	-21.20	-16.73
	P	-10.31		-11.47		8.89		-0.56		-3.93	
	M	-13.86		-13.54		-3.25		-6.50		-13.39	
	A	-36.30		-17.54		-14.23		-10.77		-30.47	
D	L	-9.56	-10.99	15.29	4.35	0.61	-0.60	23.16	9.52	-8.25	-3.24
	P	1.23		-4.73		6.33		7.20		9.37	
	M	-7.70		-0.28		-1.46		8.02		-1.85	
	A	-24.91		8.17		-4.76		0.20		-13.50	
Total		-17.67		-5.14		-2.84		2.11		-10.95	